



Searching for pulsars with MeerKAT

*A dissertation submitted to the University of Manchester
for the degree of Master of Philosophy*

in the

Faculty of Science and Engineering

2020

By

Tinn Thongmeearkom

Department of Physics and Astronomy
in the School of Natural Sciences

Contents

Contents	2
List of Figures	5
List of Tables	6
Abbreviations	7
Physical Constants	8
Abstract	9
Declaration of Authorship	10
Copyright Statement	11
Acknowledgements	12
1 Introduction	14
1.1 Discovery of pulsars	15
1.2 Neutron stars	15
1.3 Pulsars and their properties	18
1.3.1 Dispersion Measure	20
1.3.2 Spectral Index	22
1.3.3 $P - \dot{P}$ diagram	23
1.4 Types of pulsars	23
1.4.1 Normal pulsars	25
1.4.2 Millisecond pulsars	25
1.4.3 Rotating radio transients	25
1.4.4 Magnetars	25
1.4.5 Spider pulsars	26
1.5 Pulsar as tools	26
1.6 Background of the project	27

2	Instruments and programs	28
2.1	Fermi catalogue	29
2.2	MeerKAT and TRAPUM	31
2.3	Interferometric observation and beam tiling	34
2.4	De-dispersion	36
2.5	PRESTO and other pulsar analysis tools	36
2.6	Fast Fourier Transform	38
3	Project Overview and preparation	40
3.1	Source selection	41
3.2	Survey design	41
3.2.1	Sensitivity of previous surveys	43
3.2.2	System equivalent flux density	44
3.2.3	Required integration time	45
3.3	Scheduling	46
3.4	Acceleration search	52
3.5	Pulsar recording setup and processing overview	54
4	Survey classification, results, and re-processing	60
4.1	Inspection of pulsar candidates	61
4.2	Localisation	68
4.3	J1717.5–5804, aka PSR J1717–5800	69
4.4	J1526.6–2743	75
4.5	J1803.1–6708	76
4.6	J1823.8–3544	78
4.7	J1858.3–5424	80
4.8	J1906.4–1757	82
5	Discussion and conclusion	83
5.1	Discussion	84
5.2	Second pass observation	87
5.3	Deeper survey and follow-up observations	89
5.4	Targeted survey	91
5.5	Conclusion	92
A	The list of 79 sources	95
B	The details of four observing blocks	99
C	Beam tiling and position	104

List of Figures

1.1	The first pulsar	15
1.2	Stellar evolution	16
1.3	Pulsar mass distribution	17
1.4	Pulsar Model	19
1.5	Pulsar dispersion	21
1.6	Delayed time – DM plot	22
1.7	Power law model	23
1.8	$P - \dot{P}$ diagram	24
2.1	Fermi sources in Galactic coordinates	30
2.2	Galactic latitude distribution of Fermi sources	31
2.3	$\log(\text{curve significance}) - \log(\text{variability index})$ plot	32
2.4	MeerKAT telescope	33
2.5	MeerKAT interferometer	34
2.6	An example of beam tiling	35
2.7	An example of de-dispersion plan	38
2.8	The FFT decomposition	39
3.1	Targeted sources for the shallow survey in Galactic coordinates	42
3.2	SEFD throughout MeerKAT's L-band	45
3.3	Histogram of required integration times MeerKAT vs. Parkes	47
3.4	Histogram of required integration times MeerKAT vs. GBT	48
3.5	Histogram of required integration times MeerKAT vs. Arecibo	49
3.6	Histogram of required integration times MeerKAT vs. Effelsberg	50
3.7	MeerKAT's beam size	52
3.8	The elevation of sources from an observing block	53
3.9	Schematic of a binary system	54
3.10	The plot between the orbital period and acceleration/ z	55
3.11	De-dispersion plan for MeerKAT's L-band	56
3.12	Processing diagram for MeerKAT	57
3.13	Exponential fit with detected signal	58
3.14	An example of a PNG file from pdmp	59
4.1	Candidates labeller	62

4.2	An example of PSR candidate	63
4.3	An example of Noise candidate	64
4.4	An example of RFI candidate	65
4.5	An example of Tier 2 candidate	66
4.6	Generated point spread function	68
4.7	Original fold detection of J1717.5–5804	69
4.8	Localisation map for J1717.5–5804	71
4.9	L-band split	72
4.10	Localisation map for J1717.5–5804 (low frequency)	73
4.11	Localisation map for J1717.5–5804 (high frequency)	74
4.12	Original fold detection of J1526.6–2743	75
4.13	Original fold detection of J1803.1–6708	76
4.14	Localisation map for J1803.1–6708	77
4.15	Original fold detection of J1823.8–3544	78
4.16	Localisation map for J1823.8–3544	79
4.17	Original fold detection of J1858.3–5424	80
4.18	Localisation map for J1858.3–5424	81
4.19	Original fold detection of J1906.4–1757	82
5.1	Histogram of expected new pulsars from a simulation	85
5.2	MeerKAT’s beam size with new data	88
5.3	DM list	89
5.4	De-dispersion plan for second pass	90
5.5	TRAPUM’s pulsar candidate in archive data	92
5.6	Observing visibility for 5 targeted redback candidates	94
B.1	The elevation of sources from the first observing block (0620)	100
B.2	The elevation of sources from the second observing block (0704)	101
B.3	The elevation of sources from the third observing block (0804)	102
B.4	The elevation of sources from the fourth observing block (1001)	103
C.1	J1526.6–2743 beam position	105
C.2	J1717.5–5804 beam position	105
C.3	J1803.1–6708 beam position	106
C.4	J1823.8–3544 beam position	106
C.5	J1858.3–5424 beam position	107
C.6	J1906.4–1757 beam position	107

List of Tables

2.1	Technical specifications of MeerKAT's L and UHF band receivers	33
3.1	List of 79 unidentified 4FGL sources for the MeerKAT shallow survey	43
3.2	Instrumental specifications for the four main previous surveys	44
4.1	The example of result file generated by <i>labeller.py</i>	67
4.2	List of pulsar candidates	67
4.3	The information of J1717.5–5804 for localisation	70
4.4	The information of J1526.6–2743 for localisation	75
4.5	The information of J1803.1–6708 for localisation	76
4.6	The information of J1823.8–3544 for localisation	78
4.7	Information on J1858.3–5424 for localisation	80
4.8	Information on J1906.4–1757 for localisation	82
5.1	Properties of five candidate redbacks for a targeted survey	93
A.1	List of 79 sources	96
B.1	The first observing block	100
B.2	The second observing block	101
B.3	The third observing block	102
B.4	The fourth observing block	103

List of Abbreviations

DM	D ispersion M easure
ISM	I nter S tellar M edium
FFT	F ast F ourier T ransform
RFI	R adio F requency I nterference
MSP	M illi S econd P ulsar
SEFD	S ystem E quivalent F lux D ensity
PSF	P oint S pread F unction

Physical Constants

Speed of Light	$c = 2.99792458 \times 10^8 \text{ m s}^{-1}$ (exact)
Gravitational Constant	$G = 6.67408(31) \times 10^{-11} \text{ m}^3 \text{ kg}^{-1} \text{ s}^{-2}$
Solar Mass	$M_{\odot} = 1.98847 \pm 0.00007 \times 10^{30} \text{ kg}$
Solar Radius	$R_{\odot} = 6.955 \times 10^8 \text{ m}$
Parsec	$\text{pc} = 3.0857 \times 10^{16} \text{ m}$
Boltzmann constant	$k = 1.380649 \times 10^{-23} \text{ J K}^{-1}$

THE UNIVERSITY OF MANCHESTER

Abstract

Faculty of Science and Engineering
Department of Physics and Astronomy
in the School of Natural Sciences

Master of Philosophy

Searching for pulsars with MeerKAT

by Tinn Thongmeearkom

Pulsars are fabulous laboratories to study fundamental physics and can be used, among other things, to try and detect gravitational waves. Experience has shown that pulsars that prove most useful at helping us explore the laws of physics are often the rare ones, either because they are the fastest spinning ones, are found in extreme binary systems, or simply display unusual properties. This fact motivates the continuous need to search for new pulsars to expand the pool of available objects that we can use for physics studies. The work presented in this study aims to contribute to this endeavour. We follow an already well-established approach, which is to search for pulsars in regions of the sky where a gamma-ray point source has been detected by the Fermi Gamma-Ray Space Telescope, but no counterpart has been identified. Multiple of these targets are associated with energetic, young pulsars as well as millisecond pulsars. Our survey used the newly commissioned MeerKAT, the latest addition to the new generation of radio telescopes. Because of its large collective area, small dishes, and interferometric capabilities, MeerKAT represents a step-change in sensitivity, survey speed, and localisation for pulsar searching. The survey was performed at L-band and pointed for 10 minutes at each target of 79 unidentified gamma-ray sources detected with Fermi's Large Area Telescope (LAT) and selected from the 4FGL catalogue. This thesis mostly focuses on the preparation work of this survey, including source selection, processing, and candidate viewing. From the observing first pass of the survey, our work led to the identification of five excellent pulsar candidates, one of which has already been confirmed as a pulsar. We also detected one known pulsar whose location overlapped with one of the targeted fields.

Declaration of Authorship

No portion of the work referred to in the dissertation has been submitted in support of an application for another degree or qualification of this or any other university or other institute of learning.

Copyright Statement

- (i) The author of this dissertation (including any appendices and/or schedules to this dissertation) owns certain copyright or related rights in it (the “Copyright”) and s/he has given The University of Manchester certain rights to use such Copyright, including for administrative purposes.

- (ii) Copies of this dissertation, either in full or in extracts and whether in hard or electronic copy, may be made **only** in accordance with the Copyright, Designs and Patents Act 1988 (as amended) and regulations issued under it or, where appropriate, in accordance with licensing agreements which the University has from time to time. This page must form part of any such copies made.

- (iii) The ownership of certain Copyright, patents, designs, trademarks and other intellectual property (the “Intellectual Property”) and any reproductions of copyright works in the dissertation, for example graphs and tables (“Reproductions”), which may be described in this dissertation, may not be owned by the author and may be owned by third parties. Such Intellectual Property and Reproductions cannot and must not be made available for use without the prior written permission of the owner(s) of the relevant Intellectual Property and/or Reproductions.

- (iv) Further information on the conditions under which disclosure, publication and commercialisation of this dissertation, the Copyright and any Intellectual Property and/or Reproductions described in it may take place is available in the University [IP Policy](#), in any relevant Dissertation restriction declarations deposited in the University Library, The University [Library’s regulations](#) and in The University’s policy on Presentation of Dissertations.

Acknowledgements

I would like to thank my supervisors Rene Breton and Colin Clark. I consider myself very lucky to be your student. You gave me support, guidance, knowledge, and opportunity. Those help me improve my enthusiasm for learning and help me overcome the obstacles. I admire your passion for Astrophysics. Moreover, you also have good patience to explain difficult things to me several times. Without you two, I could not have made it.

Thank you to Mark Kennedy, Daniel Mata Sánchez, and other people in the Spider group for giving me a warm welcome. I have learned many things from the weekly group meetings. All of the questions and comments throughout the year have made me a little closer to being a real astronomer.

To people in the TRAPUM group. I have learned how to search for pulsars, from the beginning to the end, during the first pass of this survey. Special thanks to Maciej Serylak, who provided the SEFD information, to Lars Küinkel and Prajwal Padmanabh, who explained the MeerKAT's data processing to me, to Tiaan Bezuidenhout and Weiwei Chen, who provided the localisation script and explained the beam tiling of MeerKAT, to Laila Vleeschower Calas, who helped me find the detection parameters for localisation, to Marta Burgay and the Follow-up Working group, who will conduct the follow-up survey with Parkes to confirm our pulsar candidates, to Ewan Barr, who provided me an account to access the cluster, and to Ben Stappers and Michael Kramer for their leadership of the TRAPUM consortium and help. I hope to work with all of you in the future.

Many thanks to Oliver Dodge, Matthew Ridsdill-Smith, and Ittipat Promnorakid for reading the first draft of my dissertation. I know that it was so difficult and painful to read. All of your comments on grammar and Latex were very helpful and time-saving. Moreover, I would like to express my gratitude to Michael Keith and Ramesh Bhat, the examiners who gave many comments and suggestions for my dissertation. Those comments are very useful for the final version and improvement of my writing style in the future.

To Thai friends in Manchester: Fern, Yun, Guy, and Job, who accidentally met this lost soul in this huge city. Cheers to all of you who helped me explore university life and never get bored with me repetitively singing the same song all night.

To my friends: Note, Vudh, Tong, Pim, Jane, Jeep, Moodang, and Nina (more like brothers and sisters). The English weather makes me miss the Sun and feel alone. In spite of the 7 hours time difference, you always support and talk to me in lonely and difficult times. I hope that our paths will cross again one day.

Lastly, thank you with love to my family, for caring and believing in me. Although my MPhil journey comes to an end, the journey among the stars is just beginning.

Chapter 1

Introduction

The cosmos is full of mysteries and possibilities. It is not an easy task for us, humankind, to understand it. However, some people try their best to get a little closer to the truth. In this thesis, we will discuss the topic of “pulsars”, which are some of the most extreme celestial objects that are known to us. Over time, they have generated numerous challenges about our understanding of fundamental physics and astrophysics, yet they also offer a key to answer many questions and progress our knowledge further. True puzzling questions are rare and tend to be arising from peculiar pulsars. For this reason, we want to find as many as possible and try to understand them on an individual basis but also as a population. In this chapter, we will start by introducing some fundamental knowledge about pulsars, such as what they are and why we want to study them. Then, the motivation and background of this research project on “Searching for pulsars with MeerKAT” will be presented.

1.1 Discovery of pulsars

In 1967, Jocelyn Bell and her supervisor Antony Hewish were working on data from a hand-built radio array at the Mullard Radio Astronomy Observatory in Cambridge (Hewish et al., 1968). Bell, who was a Ph.D. student at that time, discovered a mysterious signal from the sky, which she noticed because the source appeared 4 minutes earlier every solar day which suggested that it came from outside the Solar System. Several explanations were provided, the most interesting one was "little green men" which stated that the signal was produced by an extraterrestrial civilisation. However, this is untrue. In the end, they found similar sources in other parts of the sky. They believed that these objects could be a type of pulsating compact object. It was later found that these sources match the theory of neutron stars. The discovery of the Crab pulsar in the Crab nebula supported this notion (Pacini, 1968). The first known pulsar CP 1919 (Hewish et al., 1968) is shown in Figure 1.1.

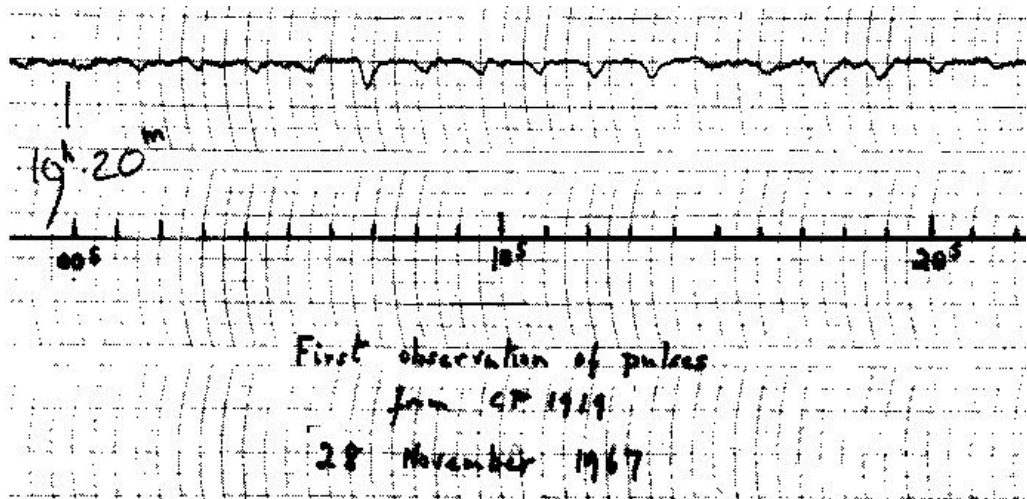


FIGURE 1.1: Image of the first high-speed recording of the first pulsar. The observation was carried out as part of a low-frequency (81 MHz) survey of extra-galactic radio sources. This mysterious unexpected signal was later known as CP 1919 (Figure from Condon & Ransom, 2016).

1.2 Neutron stars

To understand pulsars, we first need to understand stars and neutron stars. A star is a sphere of plasma held in hydrostatic equilibrium due to the pressure generated from nuclear fusion balancing gravity, which pulls matter inward. When a star with an initial mass $\gtrsim 8M_{\odot}$ (e.g. Carroll & Ostlie, 2007) stops the nuclear fusion process at the end of its life, its core collapses as nuclear pressure stops pushing out. This sudden core-collapse triggers a catastrophic event that causes the external layers of the star to violently explode as a supernova. After the supernova, the collapsed core can form one of two possible compact objects: a black hole or a neutron star (e.g. Carroll & Ostlie, 2007). A smaller star like our Sun, on the other hand, will not experience a core-collapse. It will

instead turn into a red giant and then expel its envelope less violently. This will end up forming a planetary nebula and the leftover core will turn into a white dwarf. The reason that the stellar remnant can turn into one of several object types is the state of matter under the temperature and pressure conditions. These possible outcomes of the star are mostly dictated by the mass of the remaining core. If the gravity is weaker than the quantum force of the Pauli exclusion principle, the leftover stellar core will be supported by electron degeneracy pressure. Hence, the result is a white dwarf (Chandrasekhar, 1935). If the pressure is higher than the electron degeneracy pressure limit, protons and electrons are forced to turn into neutrons via the inverse beta decay process, and the core, therefore, turns into a neutron star. Neutron degeneracy pressure also has an upper limit, beyond which an object will collapse into a black hole. For the remainder of this introduction, we will focus solely on neutron stars as the other types of stellar remnants are beyond the scope of this work.

A neutron star has its name because of the forming process. At the moment of the supernova, the gravitational collapse is extremely powerful. It is stronger than electron degeneracy pressure. Thus, it crushes protons and electrons into neutrons. A neutron star is typically assumed to have a mass around $1.4 M_{\odot}$, though actual mass measurements made using binary systems reveals that it spans a range from roughly 1.2 to $2.0 M_{\odot}$ (see Figure 1.3). The radius of a neutron star is somewhere around 10 km, thus their density is comparable to that of an atomic nucleus (which is approximately $10^{14} \text{ g cm}^{-3}$; (e.g. Lyne & Graham-Smith, 2006)).

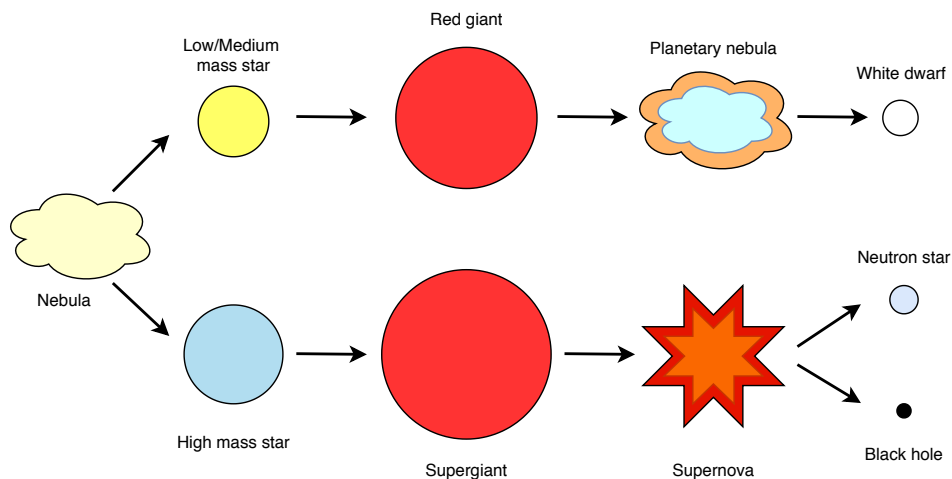


FIGURE 1.2: The diagram shows the evolution of stars, which comprises two main branches. The first branch (top) applies to low and medium mass stars. They expand as red giants and turn into a planetary nebula at the end of their lives. In the end, the leftover is a white dwarf. For the other branch (bottom), the nebula evolves into high mass stars. They expand into supergiants. Once nuclear fusion stops, their core collapses and triggers a supernova explosion. Finally, the leftover of this branch can be a neutron star or a black hole, depending on details, such as the exact remnant mass and composition.

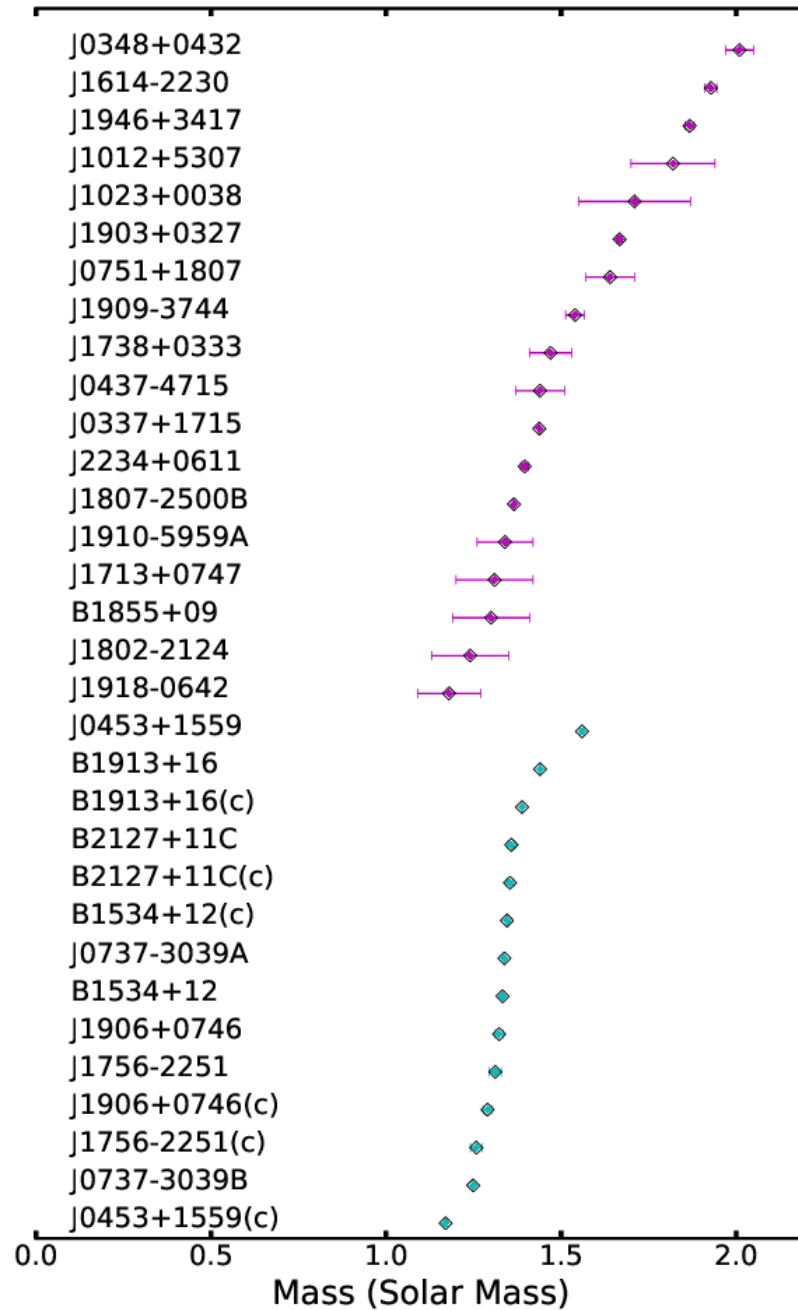


FIGURE 1.3: Mass measurements and 68% uncertainty for Neutron stars in Double neutron star and Millisecond pulsar with blue and purple, respectively (Figure from [Antoniadis et al., 2016](#)).

1.3 Pulsars and their properties

A pulsar is a neutron star that has a very strong magnetic field and a fast spin period. Its co-rotating magnetic field is so powerful that it induces a strong electric field which accelerates particles across the charge gaps. These charges follow the open magnetic field lines and produce the collimated electromagnetic emission (via synchrotron radiation and other non-thermal mechanisms) primarily along the pulsar's magnetic axis. Astronomers sometimes call this a radio beam because this signal can be observed mostly in the radio wavelength. Given that a pulsar's magnetic and rotational axes are not necessarily aligned, the star's rotation moves the beam across the sky. This produces a periodic flash of light every time the beam sweeps across the Earth. This phenomenon is similar to the light from a lighthouse that can be seen in Figure 1.4. Pulsars therefore appear to pulse on and off, which is the reason which led to being named pulsars, i.e. pulsating stars. In spite of the apparent simplicity their main observable characteristic, a lot of physics can be derived from observing them. The rest of this section will discuss some of them.

As mentioned before, pulsars have a fast spin period and are assumed to have a high magnetic field. This latter characteristic as well as others, such as the rotational kinetic energy loss, their approximate (i.e. characteristic) age, and their braking index are crucial to understanding them and can be inferred from their spin period and spin-down rate (i.e. the rate of change of the spin period), under a few assumptions. If we assume that dipole braking dominates the spin-down rate and that a pulsar can be modelled as a magnetic dipole rotating in a vacuum, with a magnetic axis offset at an angle θ with respect to the spin axis, it is possible to find an expression for the magnetic field strength, B_s , at the pulsar surface (e.g. Lorimer & Kramer, 2005):

$$B_s = \sqrt{\frac{3c^3}{8\pi^2} \frac{I}{R^2 \sin^2 \theta P \dot{P}}}, \quad (1.1)$$

where P is the spin period, \dot{P} is the spin-down rate, I is the moment of inertia, α is the angle between the magnetic moment and the spin axis. By assuming the pulsar's moment of inertia $I = 10^{45} \text{g cm}^2$, radius $R = 10 \text{ km}$, and $\alpha = 90$ (e.g. Lorimer & Kramer, 2005), one can find a simplified numerical expression:

$$B_s = 3.2 \times 10^{19} \text{G} \sqrt{P \dot{P}}. \quad (1.2)$$

We can study the rotational behaviour of pulsars by measuring their spin at different points in time; a process which we commonly refer to as pulsar timing. A pulsar's spin period should increase over time due to the loss of rotational kinetic energy. The relation between the spin period (P), spin-down rate (\dot{P}), and the loss of rotational kinetic energy (\dot{E}) (e.g. Lorimer & Kramer, 2005) can be written as

$$\dot{E} = \frac{-4\pi I \dot{P}}{P^3}. \quad (1.3)$$

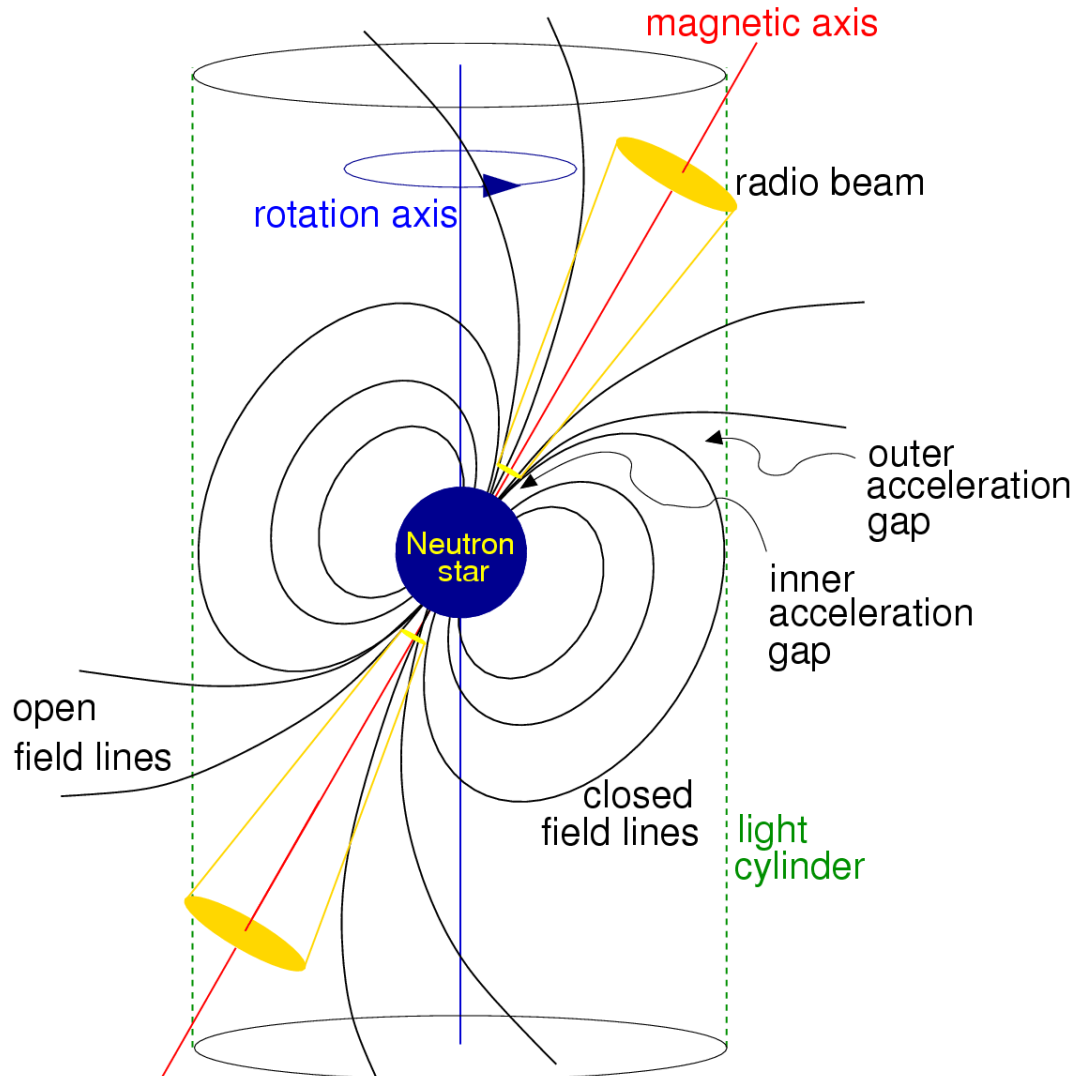


FIGURE 1.4: Pulsar model depicts the magnetosphere, radio emission region, magnetic field lines, magnetic axis, rotation axis, and a neutron star. The light cylinder is the boundary between close and open field lines. The particles rotate with the neutron star for the close field lines and move away from the neutron star for the open field lines. These distinct regions occur because the particles that are far from the surface of the neutron star need to move faster to co-rotate with the neutron star than the particles that are close to the surface. The light cylinder shows the place where the particles need to reach the speed of light to keep up with the neutron star (Figure from [Condon & Ransom, 2016](#)).

The characteristic age, τ_c , is a timescale inferred from the spin period and spin-down rate which enables one to approximate the age of the pulsar by assuming that the rotational energy loss is such that the pulsar initially spun much faster than the current observed period (e.g. [Lorimer & Kramer, 2005](#)). It is defined as

$$\tau_c = \frac{P}{2\dot{P}}. \quad (1.4)$$

1.3.1 Dispersion Measure

The dispersion delay is an effect that occurs as an electromagnetic wave propagates through an ionised interstellar medium. The electromagnetic wave experiences a frequency-dependent refraction index, which results in lower frequencies experiencing a larger propagation delay than higher frequencies. As a result, this delay causes a shift in the arrival time of the signal (see [Figure 1.5](#)). Therefore, we need to find a solution to shift it back to the phase that it should be. Fortunately, the dispersion measure (DM) can be calculated ([Figure 1.6](#)).

Electromagnetic radiation from pulsars will experience a frequency-dependent index of refraction by the interstellar medium (ISM) which can be describe as

$$\mu = \sqrt{1 - \left(\frac{f_p}{f}\right)^2}, \quad (1.5)$$

where f is the observing frequency and f_p is the plasma frequency (e.g. [Lorimer & Kramer, 2005](#)). Integration of free electrons along a line of sight can be written as

$$DM = \int_0^d n_e dl, \quad (1.6)$$

where n_e is the electron number density. The dispersion constant k_{DM} is written as

$$k_{DM} = \frac{e^2}{2\pi m_e c}, \quad (1.7)$$

where e and m_e are the charge and mass of an electron, respectively (e.g. [Lorimer & Kramer, 2005](#)). By using an approximate numerical factor of $4.15 \text{ MHz}^2 \text{ pc}^{-1} \text{ cm}^3 \text{ ms}$, the time delay in milliseconds between two frequencies can be written as

$$\Delta t = 4.15 \text{ ms} \left(\frac{DM}{\text{cm}^{-3} \text{ pc}} \right) \left[\left(\frac{\nu_1}{\text{MHz}} \right)^{-2} - \left(\frac{\nu_2}{\text{MHz}} \right)^{-2} \right] \quad (1.8)$$

with Δt being the time delay between two observing frequencies, ν_{low} and ν_{high} in MHz (e.g. [Lorimer & Kramer, 2005](#)). After calculating the delay time, the data at different frequencies can be shifted, or “de-dispersed”, in order to compensate for the delay. Two options are possible, incoherent de-dispersion and coherent de-dispersion, which we will discussed later in [chapter 2.4](#).

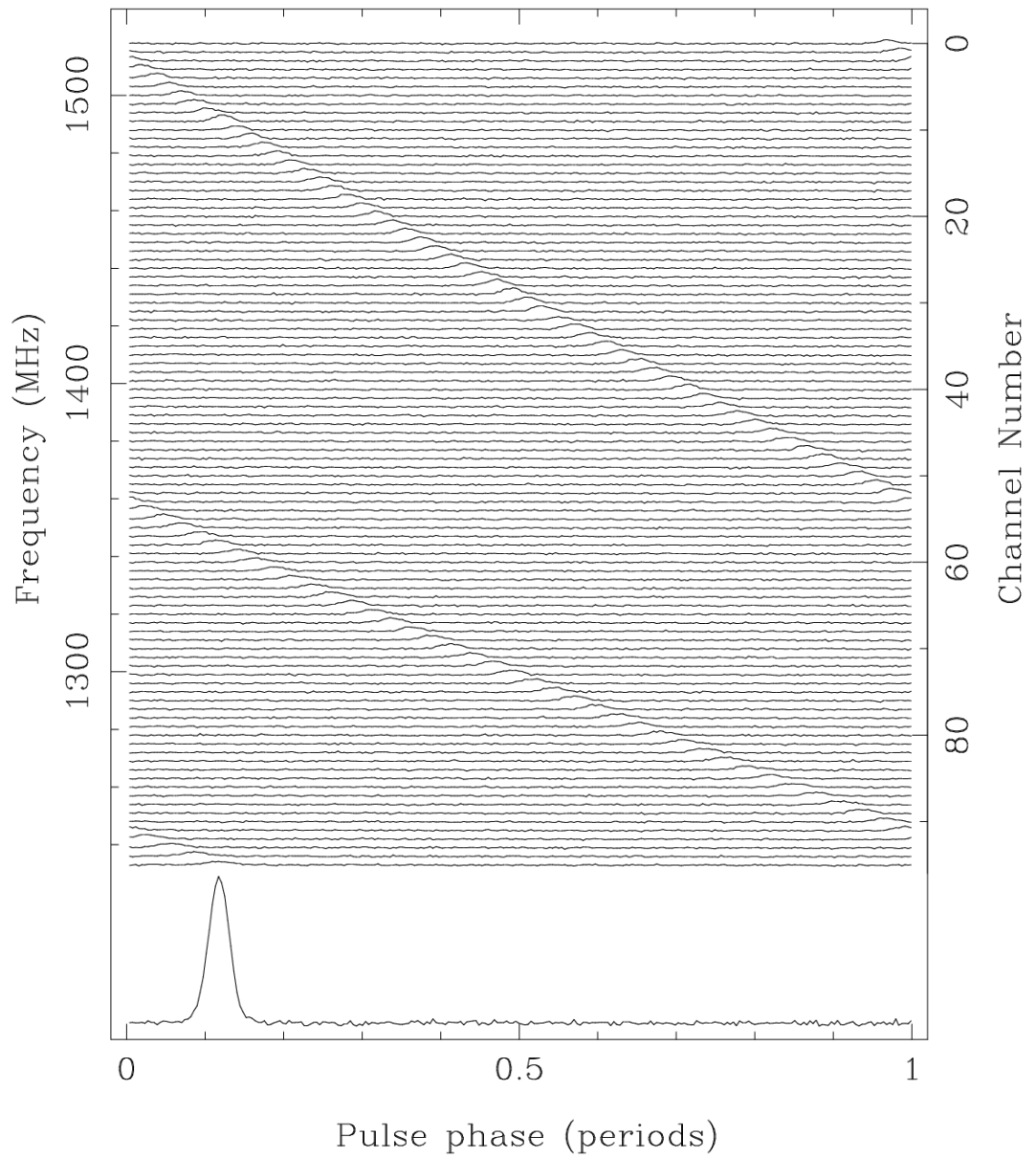


FIGURE 1.5: B1356-60 is a 128 ms pulsar. We can clearly see the dispersion delay throughout the frequency band. Without this delay, the signal would look like a straight line which would align with the Gaussian like pulse at the bottom of the plot. This data is from the Parkes telescope and the pulsar has a dispersion measure of $295 \text{ pc}/\text{cm}^3$ (Figure from [Lorimer & Kramer, 2005](#)).

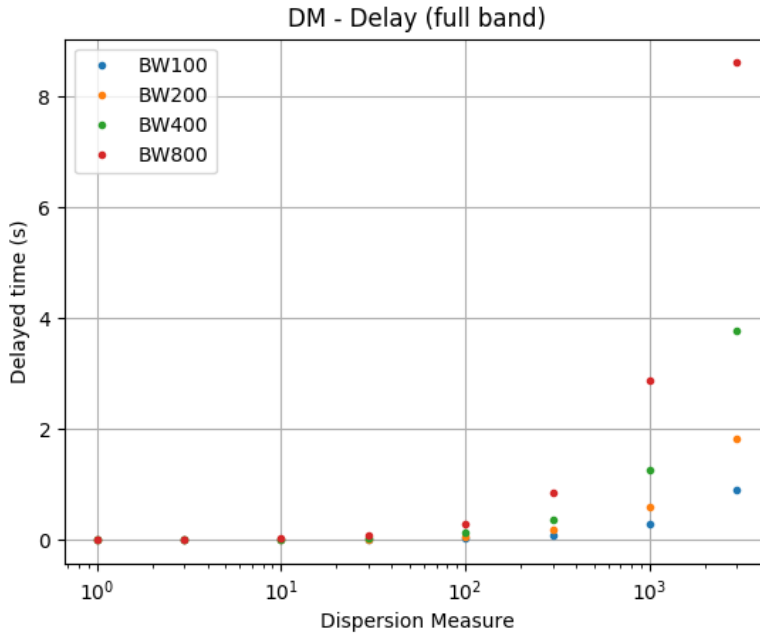


FIGURE 1.6: Delay across the full observing band centred at 1400 MHz for DMs ranging from 1 to 3000 pc cm^{-3} . Colours blue, orange, green and red represent a bandwidth of 100, 200, 400 and 800 MHz, respectively.

1.3.2 Spectral Index

The unit of flux density in radio astronomy is Jansky (Jy) where $1 \text{ Jy} \equiv 10^{-26} \text{ W m}^{-2} \text{ Hz}^{-1}$. There are two measurements that astronomers typically use to describe the flux of a pulsar: the peak flux density, which is the value at the maximum of a pulse profile, and the mean pulsed flux density, which is the average flux density over the pulse (e.g. Lorimer & Kramer, 2005). Pulsars are typically observed to have a spectrum that is well described by a power law function with the frequency turnover around 100-600 MHz (Sieber, 1973; Malofeev et al., 1994). The power law function can be described as

$$S_\nu = S_0(\nu/\nu_0)^\alpha, \quad (1.9)$$

where S_0 is the flux density at the reference frequency ν_0 , and α is the spectral index (Bilous et al., 2016). Most pulsars tend to be brighter at lower frequencies (i.e. they have a negative spectral index) and various studies have attempted to characterise their pulsar spectral index by using the results from several surveys. In such a study, Bates et al. (2013) found that the power law index for the pulsar population can be modelled using a Gaussian distribution with a mean of -1.4 and a unit standard deviation. The power law fitting with a pulsar model can be seen in Figure 1.7.

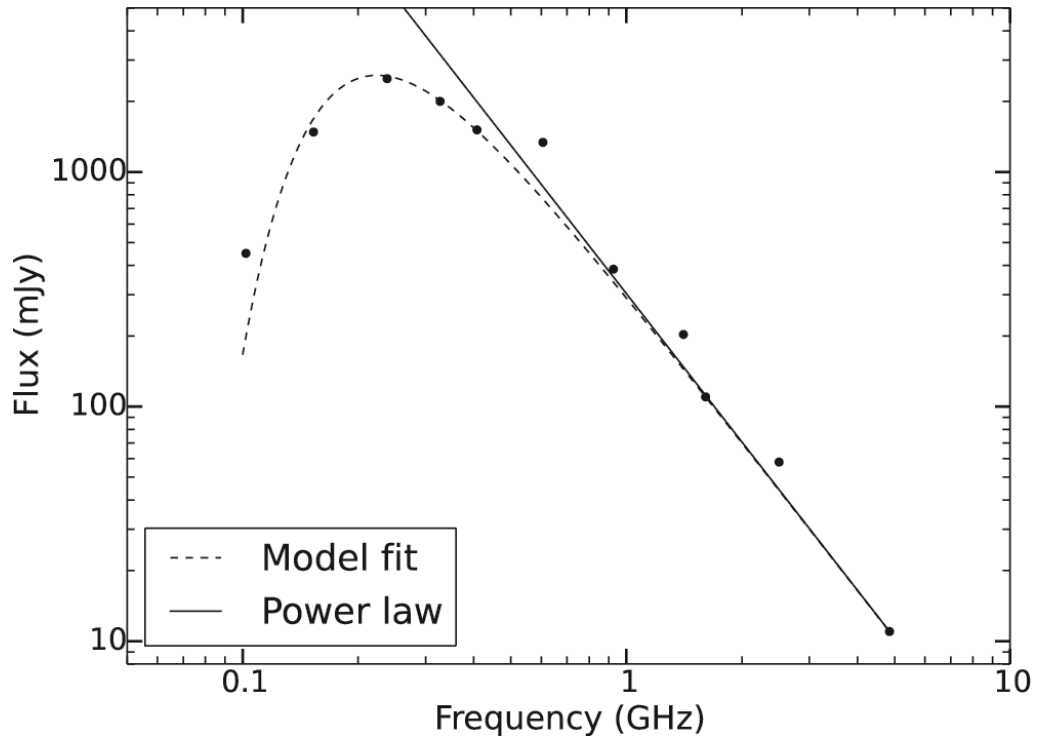


FIGURE 1.7: The solid line shows Power law spectrum while the dashed line displays the best fitting curve from the model for PSR B0329+54. The black circles are measured flux densities. The power law has a spectral index $\alpha = -2.1$ (Figure from [Rajwade et al., 2015](#)).

1.3.3 $P - \dot{P}$ diagram

We can use the knowledge about the timing and its connection to the physical properties of pulsars to depict the known population on a $P - \dot{P}$ diagram (see Figure 1.8). The vast majority of pulsars are referred to as normal pulsars. This population is located at the centre of the diagram. At the bottom left of the diagram, we can see another population that has a low spin period and low spin-down rate, these objects are millisecond pulsars (MSPs). MSPs are very useful objects, they can be used as a probe and a clock which we will discuss in the next section. According to the diagram, most of the millisecond pulsars are in a binary system. Moreover, the diagram also shows other types of pulsars, for instance, pulsars in supernova remnants and radio-quiet pulsars. The $P - \dot{P}$ diagram plays a crucial role in many studies about the evolution of pulsars, such as [Ridley & Lorimer \(2010\)](#) and [Johnston & Karastergiou \(2017\)](#)

1.4 Types of pulsars

There are several types of pulsars. According to the $P - \dot{P}$ diagram Figure 1.8, the two most noticeable types are normal pulsars which are located at the centre of the diagram, and millisecond pulsars which are depicted at the bottom left of the diagram. However, there are other types that are unique and fascinating that we will discuss in this section.

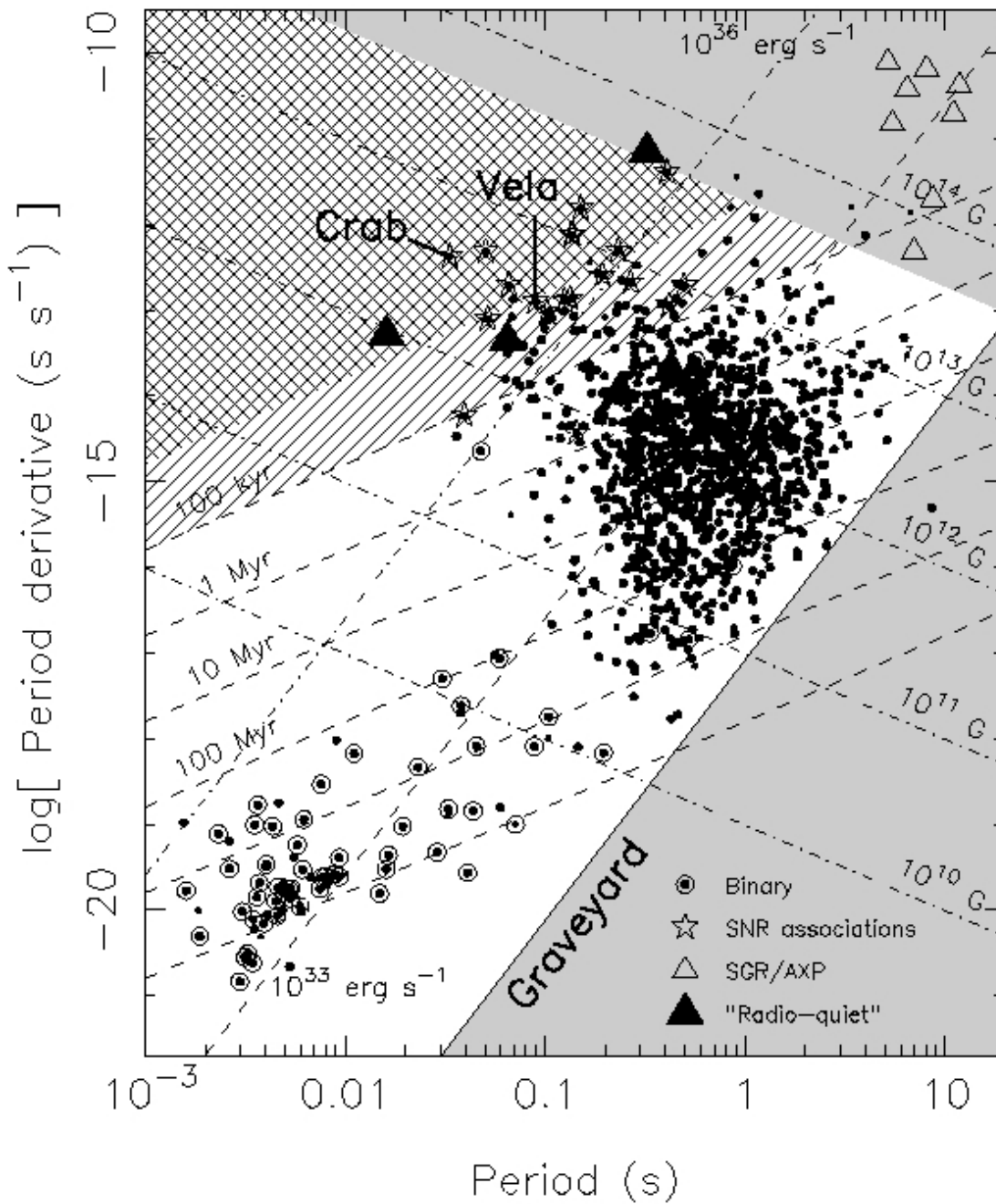


FIGURE 1.8: The $P - \dot{P}$ diagram illustrates the population of pulsars by using two main observable timing parameters: the period and the period derivative. By doing this, it also provides a way to connect physical properties to the rotational behaviour using the simple pulsar toy model of a magnetic dipole spinning in vacuum. One can therefore estimate the characteristic age, magnetic field and spin-down power. (Figure from [Lorimer & Kramer, 2005](#))

1.4.1 Normal pulsars

Normal pulsars are displayed around the centre of the $P - \dot{P}$ diagram. The vast majority of pulsars are of this type. The characteristics of this type are described in section 1.3. For younger pulsars, such as the Crab and the Vela pulsars, we can find a supernova remnant association (O'Leary et al., 2015). Furthermore, these young pulsars can be detected in gamma-ray (Thompson et al., 1993).

1.4.2 Millisecond pulsars

A millisecond pulsar is a pulsar whose rotational period is in the range of a few milliseconds. While there is no formal definition, they often include pulsars with $P \lesssim 30$ ms. They also have a very low period derivative. Hence, we can find millisecond pulsars located at the bottom left corner in $P - \dot{P}$ diagram. Because of their stable rotation and the precision of timing the pulse's arrival time (as a fraction of the pulse width), we can use this type of pulsar as a clock. Millisecond pulsars also tend to be in binary star systems. There is a theory on the evolution of millisecond pulsars. In a binary system, when the companion main-sequence star evolves into a red giant it can fill the Roche lobe. As a result, the mass from the giant transfers to the old spun-down neutron star. The neutron star can spin-up and turn into a millisecond pulsar by accreting matter and angular momentum known as "recycled pulsar" (Lorimer, 2008). Millisecond pulsars are an ideal experiment tool, they can be used to test many astrophysical phenomena. For instance, planet detection, testing relativity, and low-frequency gravitational-wave detection (Manchester, 2017).

1.4.3 Rotating radio transients

Rotating Radio Transients (RRATs) are neutron stars that are more easily detectable in a single pulse search than in a periodicity search. The first RRAT was discovered in 2006 by McLaughlin et al. (2006). The study reported that eleven objects were characterised by dispersed bursts with durations between 2 and 30 ms. The sources had time intervals between bursts ranging from 4 minutes to 3 hours.

1.4.4 Magnetars

Magnetars are highly magnetised neutron stars. The magnetic field of a magnetar is exceedingly powerful approximately 10^{15} G (Duncan & Thompson, 1992). Magnetars also exhibit X-ray signals and many fascinating phenomena, for instance, spin-down, glitches, and anti-glitches. Moreover, magnetars are likely to represent the young neutron star population Kaspi & Beloborodov (2017).

1.4.5 Spider pulsars

Spider pulsars are a type of binary pulsar system that contain an energetic millisecond pulsar which strongly interacts with a low-mass companion orbiting in a compact orbit via their relativistic wind and/or high energy radiation (Roberts et al., 2018). The first spider pulsar was discovered by Backer et al. (1982). The interaction produces a strong irradiation of the companion, which heats up the side facing the pulsar, and also leads to material being blown away from the companion's surface. The 'evaporation' of the companion leads these systems to be compared to the deadly spiders of the 'black widow' family, in which the female spider sometimes consumes the male after mating. There are two main types of spider pulsars, black widows and redbacks. In 2013, observed data depicts that the black widows companion's mass ($M_2 \ll 0.1M_\odot$) is lower than redbacks companion's mass ($M_2 = 0.1 - 0.4M_\odot$) (Chen et al., 2013). They proposed that the redbacks and the black widows have a distinct evolution path due to a fraction of the emitted spin-down energy of the radio pulsar, the redbacks absorb a larger fraction than the black widows. They believe that redbacks do not evolve to black widows.

Spider pulsars are a link between two different systems. Those are low-mass X-ray binaries and radio millisecond pulsars. An X-ray signal has been observed during an X-ray phase while a radio signal can be detected when a millisecond pulsar phase. This fascinating changeable system known as a transitional pulsar. There are many studies on these systems, such as monitoring an optical counterpart (Breton et al., 2013), monitoring in X-ray (Bogdanov et al., 2011) and in gamma-ray (Aliu et al., 2016).

1.5 Pulsar as tools

The importance of pulsars shines when it comes to using them as tools. Pulsars can be used as many different probes. These extreme objects are used to test the general relativity theory. The evidence suggested the existence of gravitational radiation (Taylor & Weisberg, 1982). For another type of study, a large number of millisecond pulsars, which have a very consistent spin period, low spin-down rate, and variations in the spin frequency. Hence, they are utilised as a clock. Because of these properties, a pulsar timing array (PTA) has been developed. PTA is an array of millisecond pulsars for detecting gravitational wave at low frequencies from nHz to μ Hz (Detweiler, 1979). This technique is a new window to observe a very weak gravitational wave.

1.6 Background of the project

As stated before, young pulsars and spider pulsars can be detected in a wide range of wavelengths. They also prove to be remarkable cosmic laboratories, which motivates the never-ending quest to find more of them, in particular the rare systems that display the more extreme properties. To find new radio pulsars, searching specific locations of the sky where prior information is available (e.g. from observations made in other parts of the electromagnetic spectrum) about the strong possibility of finding one of them can be a very fruitful approach. Not only it is more likely that new pulsars can be found, but also we can search for deeper flux sensitivity limits than that which would be possible with the broad, unguided survey. Many studies have used unidentified Fermi gamma-ray sources as targets (Ransom et al., 2010; Keith et al., 2011; Barr et al., 2012; Camilo et al., 2015; Cromartie et al., 2016). Their results show that observing pulsar-like gamma-ray sources is a successful strategy. Therefore, in this study, we follow a similar approach and use the MeerKAT radio telescope to observe unidentified Fermi sources. MeerKAT is part of the new generation of radio telescopes; using it for our survey will provide better sensitivity than the previous work. Hence, we expect to find several pulsars, either because their location could not have been searched before due to time limitations or simply because they escaped detection. The 4FGL Fermi catalogue is utilised as the basis of this project, the information about it can be found in Abdollahi et al. (2020). We expect to find young pulsars and energetic, rapidly spinning pulsars.

The structure of the thesis is as follows. In chapter 2, we introduce more details about the MeerKAT and Fermi telescopes, the TRAPUM collaboration, and tools used for pulsar searching. In chapter 3, we provide details about our contribution to the survey preparation (i.e. source selection, scheduling, observing parameter, and processing). In chapter 4, we present the candidate viewing program we built for the project, the first results from the survey and our work on preliminary source localisation. Finally, we discuss some of the implications of our work, elaborate on upcoming future work and offer conclusions in chapter 5.

Chapter 2

Instruments and programs

This study aims to find new pulsars using the newly-built MeerKAT radio telescope. The focus of the survey that we conducted was to point the telescope at specific locations where Fermi unidentified sources are located. In this chapter, we introduce the instruments, both the MeerKAT radio telescope and the Fermi Gamma-ray Space Telescope, and then move on to the importance of survey planning and scheduling. We introduce and discuss several vital equations related to these topics, such as the radiometer equation, the dispersion measure, and the system equivalent flux density. Lastly, we will elaborate on standard pulsar programs such as PRESTO and PSRCHIVE that are used for data analysis.

2.1 Fermi catalogue

The Fermi Gamma-ray Space Telescope is a space telescope that started operations in 2008. The primary instrument is the Large Area Telescope (LAT) used for observing the gamma-ray phenomena at high energies mainly involving non-thermal processes, such as accelerated particles emitting radiation. Results from the first 11 months of the science phase were presented in the First Fermi-LAT catalogue (1FGL) (Abdo et al., 2010). This catalogue contains 1451 sources, most of which are connected to energetic phenomena, for instance, supermassive black holes, merging neutron stars, and extremely fast-moving hot gas. Numerous Fermi sources are classified, for example, pulsars (PSRs), normal galaxy (GALs), active galactic nuclei (AGNs), globular cluster (GLCs), and unidentified sources (UNKs). Throughout several years, the characterisation, localisation, and the model of Galactic diffuse gamma-ray emission have been developed in 2FGL catalogue Nolan et al. (2012) and in 3FGL catalogue Acero et al. (2015). In this study, we use the point source catalogue published in early 2019, the Fermi-LAT Fourth Source Catalogue (4FGL). This catalogue consists of 8 years of data in the 50 MeV to 1 TeV energy range. It contains 5064 sources overall with 1336 of them which remain “unidentified sources”, that is no association with another source observed in another part of the electromagnetic spectrum has been made. The Fermi-LAT team developed a new model to describe the underlying diffuse Galactic emission and used a new weighted log-likelihood method to systematically test spectral fitting Abdollahi et al. (2020).

As mentioned earlier, the majority of Fermi sources have been classified as belonging to a certain type of astrophysical object already. There are 239 sources that have been identified as pulsars (Abdollahi et al., 2020). Figure 2.1 shows the distribution of PSRs, AGNs and, unidentified Fermi sources from the latest 4FGL catalogue in Galactic coordinates. As expected, the spatial distribution of AGNs appears to be isotropic due to their extra-galactic origin. On the other hand, pulsars and unidentified sources follow an anisotropic distribution. Figure 2.2 provides more details about the Galactic latitude distribution of unidentified sources as well as pulsars, which have been split between young pulsars and MSPs. Young pulsars tend to be closer to the Galactic plane than MSPs because the latter are old and have travelled more significantly away from the site of the supernova explosion in which they formed. On the other hand, young pulsars tend to be closer to the plane, where we find clusters of young and massive stars that form pulsars. In the case of unidentified Fermi sources, they also show a preference for clustering closer to the plane with an extended tail at a larger Galactic scale height. A fraction of them is probably associated with pulsars whose pulsations have yet to be discovered. Many background AGNs are likely too absorbed to be detected at optical wavelengths along the plane. Given that the gamma-ray photons travel mostly without being blocked across our Galaxy. This creates a bias against identifying them at lower latitudes.

In 2016, there was a study of classification and ranking of Fermi sources using machine learning (Saz Parkinson et al., 2016). They found a likelihood of a source is from

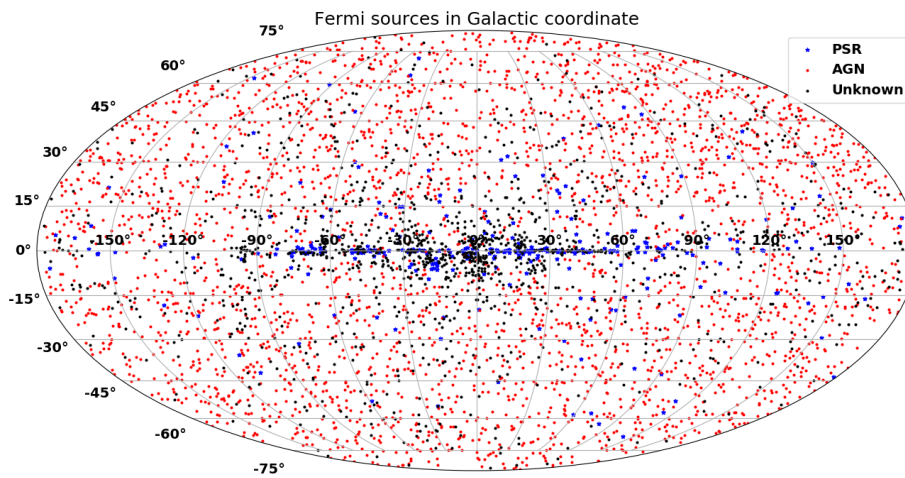


FIGURE 2.1: 4FGL Fermi sources Galactic coordinates. The red, blue and black represent AGNs, pulsars and unidentified sources, respectively. Pulsars tend to line along the Galactic plane while AGN spread across the sky. The reason is that pulsars used to be massive stars, which cluster along the plane, while AGNs are galaxies and thus uniformly distributed in the sky.

one of two main categories. Those are PSR and AGN. In addition, further classification of young pulsars and millisecond pulsars have been made. By filtering missing value sources, a training sample and a testing sample have been created. They applied many techniques, for instance, random forest, logistic regression, and modified logistic regression to find the most accurate technique. Their results suggested that 75% of 125 unidentified sources are pulsars and the two-thirds are predicted to be young pulsars, the remaining third are millisecond pulsars (Saz Parkinson et al., 2016).

To understand different types of classification, the 4FGL sources are plotted between the variability index against the curve significance. This can be done because gamma-ray pulsars show a distinct gamma-ray signature from other types of sources, for example, AGNs. As a result, it can be inferred that pulsars have relatively lower variability and higher spectral curvature than that of AGN as seen in Figure 2.3.

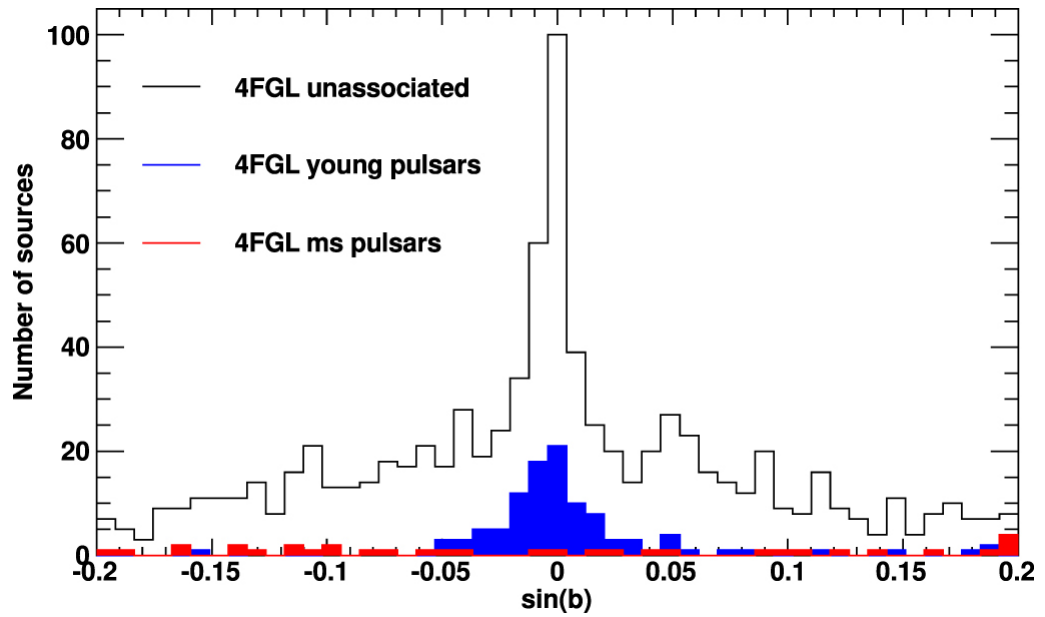


FIGURE 2.2: Galactic latitude distribution of 4FGL sources. The black, blue and red colour histograms represent unidentified sources, young pulsars and millisecond pulsars (MSP), respectively (Figure from [Abdollahi et al., 2020](#)).

2.2 MeerKAT and TRAPUM

The Karoo Array Telescope (MeerKAT) is an interferometer array of 64 radio telescopes. At the moment, MeerKAT is the most sensitive telescope which operates at centimetre wavelengths in the Southern hemisphere. It is located in the Karoo, a desert region in the Northern Cape, province of South Africa. MeerKAT (and the future SKA telescope) was built in this region specifically due to its low population density. As a result, there is very low radio frequency interference (RFI) in this region which is therefore considered to be superior quality for radio astronomy [Booth et al. \(2009\)](#). The core of MeerKAT is located at a longitude $21^{\circ}230E$ and latitude $30^{\circ}420S$. Each one of the MeerKAT dishes has a diameter of 13.5 metres. The relative ground position of each antenna is illustrated in [Figure 2.5](#). The longest baseline is 8 kilometres, while the shortest one is 20 metres ([Booth et al., 2009](#)).

TRAPUM stands for TRAnsients and PULsars with MeerKAT. TRAPUM's objectives are to discover the number of new pulsars in targets, unidentified Fermi sources, supernova remnants, and globular clusters to understand the science of those extreme sources ([Jonas & MeerKAT Team, 2016](#)). Moreover, by using new generation telescope, MeerKAT, finding pulsars and fast transients outside Milky way are expected. TRAPUM is a flagship survey for upcoming Square Kilometre Array (SKA). The data processing from TRAPUM will be vital for further SKA development. There are several projects on TRAPUM, for instance, targeted pulsar searches, globular cluster searches, and extra-galactic pulsar and transient searches. This dissertation is a part of targeted pulsar searches. Hence, we will only discuss the targeted survey. The targeted survey of Fermi unidentified gamma-ray sources can detect pulsars that have a gamma-ray counterpart. This provides many

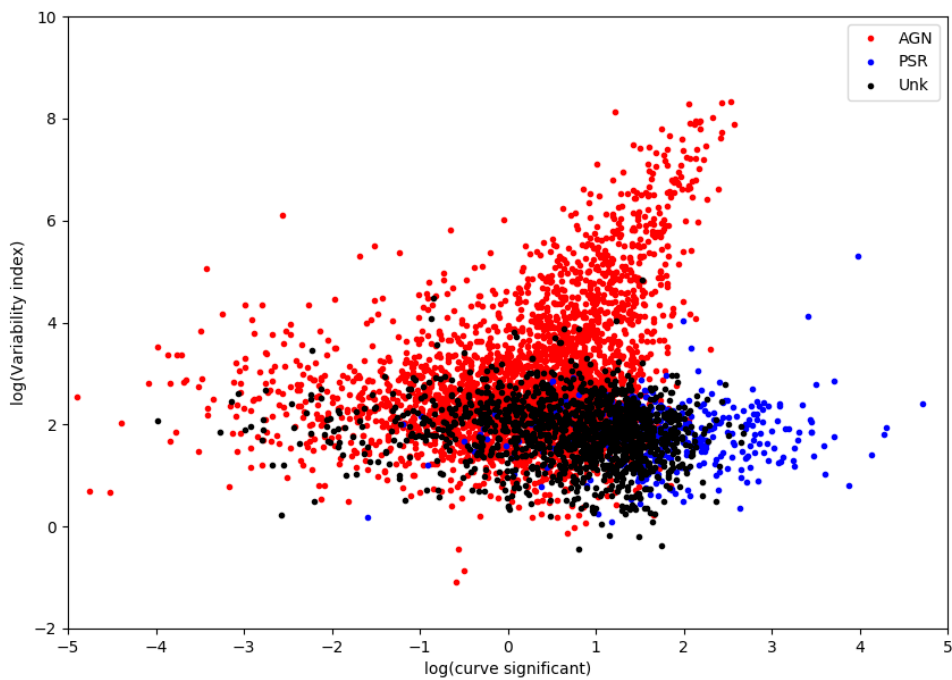


FIGURE 2.3: Variability index of Fermi sources as a function of the significance of the gamma-ray spectrum curvature. This plot shows that there are two main groups. The first group is located on the left-hand side and going upward diagonally are AGNs. The second group are pulsars. They tend to show lower variability, yet comparatively higher spectral curvature. There is a region where these two groups overlap, and most of unidentified sources usually belong to this region (Data from [Abdollahi et al., 2020](#)).

Parameter	L-band	UHF
Bandwidth (MHz)	856	544
Centre frequency (MHz)	1284	816
Bandwidth* (MHz)	800	400
Centre frequency* (MHz)	1400	800
Gain ^ζ (K/Jy)	2.75	2.75
Receiver temperature ^ζ , T_{rec} (K)	18.15	18.15
Coherent beam radius (arcsec)	~ 20	~ 35

TABLE 2.1: Specifications of MeerKAT's L and UHF bands. Information provided by Maciej Serylak (priv. comm.). The * refers to the value that we use for the calculation in section 3.2.1. Due to some data is affected by RFI, 1400 MHz is used for a centre frequency of L-band. The ^ζ refers to the result from the calculation in section 3.2.2. At the calculation time, the UHF information was not provided. Therefore, we assume the same L-band's Receiver temperature for UHF. Coherent beam radius is a semi-major axis at $\sim 30^\circ$ elevation.

benefits. Finding young pulsars may help us to understand the the Galactic neutron star formation rate, the nature of supernovae, and the interaction between a young pulsar and its remnants (Brinkmann et al., 1985). On the other hand, the discovery of millisecond pulsars can improve our knowledge on the link between millisecond pulsars and low-mass X-ray binary transition known as "transitional pulsar" (Stappers et al., 2014). Furthermore, short period millisecond pulsars can be used as precision clocks for the International Pulsar Timing Array (Verbiest et al., 2016). For the observation, 338 hours has been proposed to conduct the Fermi targeted searches.



FIGURE 2.4: Night time photograph of the MeerKAT telescope near the core of the array (Image from the SARAo website).

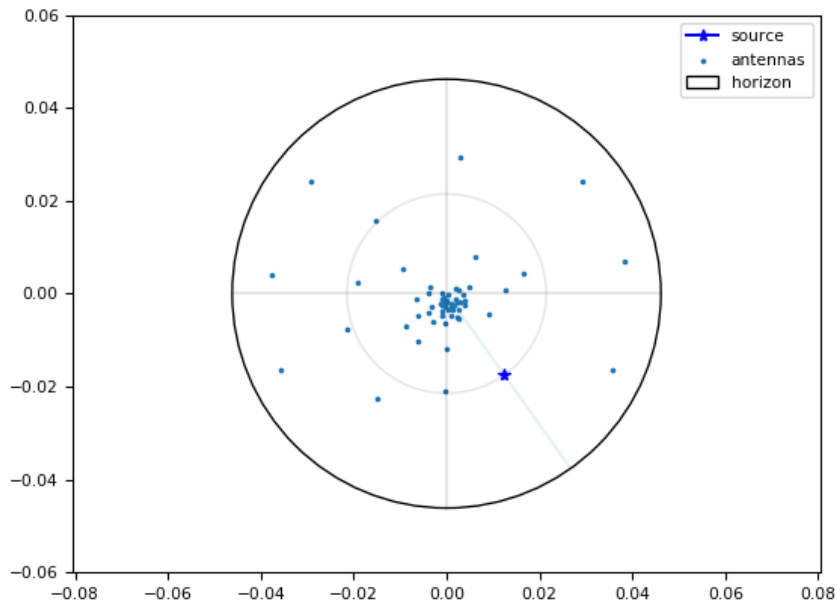


FIGURE 2.5: MeerkAT interferometer of 64 antennas (blue dots), the blue star is a projection of the target. This plot is generated by `tilesim.py` (more information in chapter 4.2).

2.3 Interferometric observation and beam tiling

Interferometric observation is a technique using many telescopes to create a small beam. For a single dish telescope, beam size depends on λ/D , where λ is a wavelength, and D is a diameter of a telescope (order of metres). For interferometer, on the other hand, beam size is λ/B , where B is a baseline or distance between two telescopes (can be as far as kilometres). Therefore, an interferometric beam can be much smaller compared to a single dish. This implementation can be used as high-resolution detection. However, we want to use the optimised resolution and sky coverage for searching. Hence, beam tiling is used to create a large field of view with high resolution. MeerkAT has several observing modes. In this survey, we use coherent beam mode where many antennas point to the targets and create many small coherent beams. Each coherent beam overlaps together to form the main beam. The MOSAIC python package has been developed by Chen et al. (in prep). This package uses UV coverage and the Fourier transform to create a point spread function (PSF) of the array which can be implied as a coherent beam. The next step is beam tiling. The area of the main beam depends on a few factors: the size of the coherent beam, the number of beams, and the overlap parameter shown in Figure 2.6. An overlap of 50% (0.5) shows that the coherent beams intersect at their half-power.

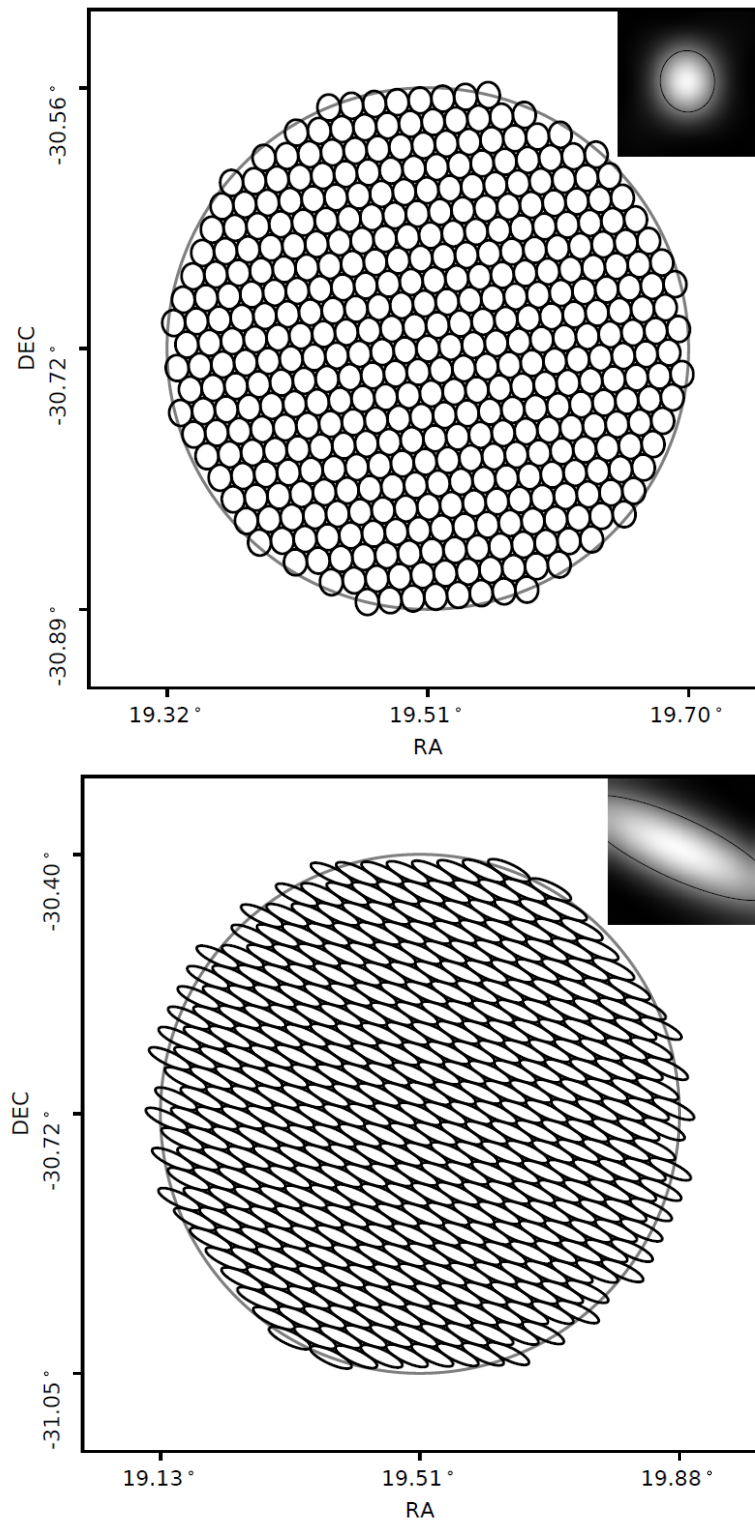


FIGURE 2.6: An example of beam shape and beam tiling. The configuration is from inner 44 dishes. The top image is the MeerKAT array points to the zenith with 405 beams while the bottom image is the MeerKAT array points near the horizon with 409 beams. As a result, the sky coverage from bottom setting is larger than the top (Figure from Chen et al. (in prep)).

2.4 De-dispersion

Before de-dispersion, we will discuss a filterbank file which is a standard format in pulsar astronomy, first. Filterbanking is a step where the program uses Fourier transform to turn raw baseband data into a filterbank file, which has the intensity, time, and frequency component. In section 1.3.1, dispersion measure and two types of de-dispersion procedures were mentioned. Incoherent de-dispersion is a post-filterbank process. The program separates the signal into frequency blocks. As a result, the algorithm can calculate a delay for each block. It then moves them to the appropriate position in order to compensate for the delay. Incoherent de-dispersion can be done off-site because this technique can have lower data rate compared to coherent de-dispersion. Incoherent de-dispersion can be applied on downsampled data in time and frequency compared to the original raw data. However, it comes with a disadvantage of smearing effects. These effects occur because of the imperfect reconstruction of incoherent de-dispersion. Smearing can take place for a number of reasons. Firstly, channel smearing is a delay that occurs in each channel. Secondly, DM stepsize smearing is a delay dictated by the DM step. Thirdly, subband stepsize smearing is a delay that occurs due to a splitting of frequency band into subbands. Total smearing is a combination of these smearing types with a sample time.

Coherent de-dispersion, on the other hand, requires the original Nyquist sampled voltage signal (Hankins & Rickett, 1975; Straten, 2003; De & Gupta, 2016). This technique is generally applied at the same time as the data are channelised in a filterbank. Given the data rate generated from a modern radio receiver, coherent de-dispersion is generally performed on-site (and in real time). Coherent de-dispersion utilises a specific function to adjust the phase of a signal in the Fourier domain (frequency domain) because it is applied before the signal is divided up into frequency channels, the de-dispersed data will not suffer from intra-channel smearing effects as well as those related to the time averaging of the data. Although coherent de-dispersion is computationally expensive and not widely used at low-frequency, it does not suffer from this at higher-frequency as much as lower-one.

2.5 PRESTO and other pulsar analysis tools

PRESTO stands for Pulsar Exploration and Search TOolkit, is a software suite for analysis and pulsar searching developed by Scott Ransom (Ransom, 2011). It comprises a number of standalone programs that can be executed on recorded pulsar data in order to process them. When searching for new pulsars, the DM of new sources is unknown. A range of values must be searched in order to identify pulsations with the least dispersion smearing possible as otherwise the significance of the detection will be reduced, or the pulse completely smeared away as channels are combined. So far, a brute force search of the DM phase space has proven to be the most optimal approach. Before a survey is undertaken, a de-dispersion plan must be designed in order to determine the most optimal

choice of de-dispersion steps, given the range of DM considered and the instrumental parameters in order to ensure that the drop in sensitivity between two DM trials is sensible. *DDplan* is a python script part of PRESTO which is used to find such an optimal way to execute the de-dispersion process. An example of a de-dispersion plan produced by *DDplan* is showed in Figure 2.7 and displays the various smearing effects explained earlier.

PRESTO also incorporates other programs designed to deal with several areas of pulsar analysis. Those are data preparation, searching, and folding. The preparation part involves the detection of RFIs (*rfifind*) and removal of common human-generated periodicities (*zapbirds*), de-dispersion of the data (*prepdata*, *prepsubband*, or *mpiprepsubband*, depending on the input types), barycentering (done using the aid of the *TEMPO* pulsar timing software (Nice et al., 2015)). Once the initial processing of the data is done, the de-dispersed time series are ready to be searched for pulsations. The searching is generally carried out in the Fourier-domain and can account for a linear acceleration of the data caused by binary motion (*accelsearch*), or, occasionally, in the time domain to detect individual single pulses (*singlepulsesearch.py*). Such a single pulse search has proved very useful and led to the identification of RRATs (McLaughlin et al., 2006) as well as the discovery of Fast Radio Bursts (FRBs) later on (Lorimer et al., 2007; Thornton et al., 2013). For binary systems, additional techniques can be employed such as phase-modulation or sideband searches (*searchbin*). Lastly, the promising candidates can be ‘folded’ and their periodicity and DM parameters are optimised (*prepfold*) to display the pulsed signal. For known pulsars, PRESTO also enables one to extract the ‘Time-of-Arrival’ (TOA) of pulsations (*getTOAs.py*) from the folded data.

A number of other pulsar software suites also exist such as *dspsr*, *sigproc* and *PSRCHIVE*. They implement a subset or additional features than those available within PRESTO. *PSRCHIVE*, for instance, is also a program to analyse pulsar data developed in C++. A wide range of algorithms has been implemented for pulsar timing, scintillation studies, polarimetric calibration, single-pulse work, and RFI mitigation. The software is described in details by W. Hotan et al. (2004). Most of these pulsar analysis programmes are made available open source and are maintained by the community. Graphics Processing Units (GPUs) now also offer very powerful hardware to perform several of the tasks involved with pulsar searches, thus many of the aforementioned tools, and new ones, are being developed. For the next generation of radio facilities, such as MeerKAT, the volume of data to be processed is simply too large to be handled by a small-scale computer. Hence, MeerKAT implements its own data analysis pipeline, which borrows components from PRESTO and other softwares and has been dubbed ‘PulsarX’. A full description of this software has not been officially published yet.

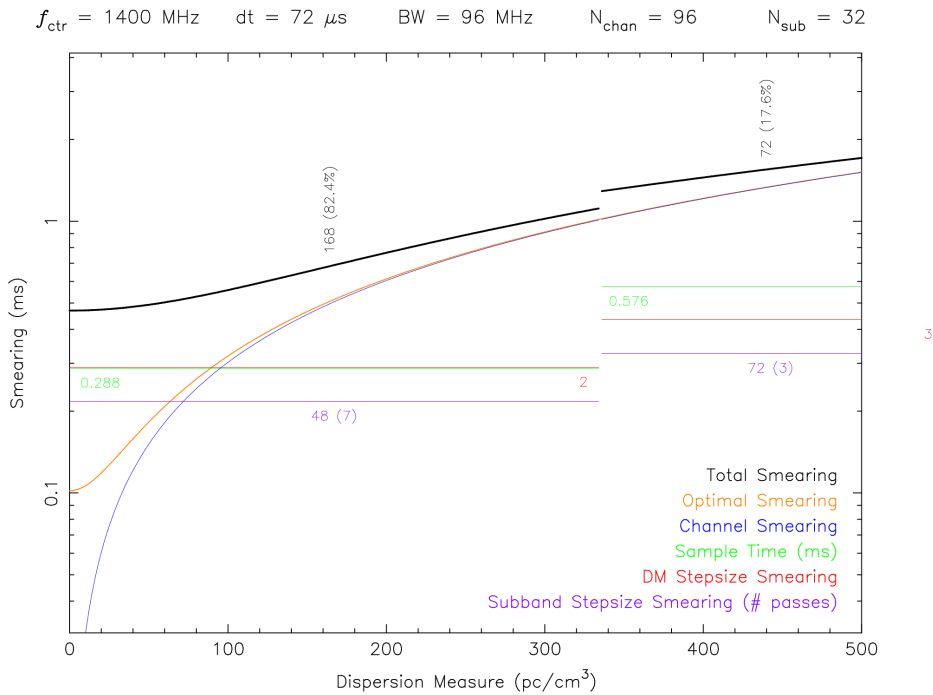


FIGURE 2.7: An example of de-dispersion plan from the PRESTO tutorial. On the top, the used information to run de-dispersion plan is shown. The parameters are : f_{ctr} is the centre frequency, dt is a sample time, BW is a bandwidth, N_{chan} is number of channels, and N_{sub} is number of subbands. The colour lines represent different smearing effects while the black line is a total smearing (Figure from PRESTO - Pulsar Exploration and Search Toolkit).

2.6 Fast Fourier Transform

As most pulsation searching is performed in the Fourier domain, we need to introduce the concept of Fast Fourier Transform (FFT), which is a specific algorithm used to perform discrete Fourier transforms (Cooley & Tukey, 1965) of digital data between the time and frequency domains very efficiently. We shall recall that time and frequency domain are related to each other (i.e. $t = \frac{1}{f}$). In the first step, the FFT algorithm rearranges the position of data as showed in Figure 2.8. For example, for one data signal of 16 points, the program separates data into two data signals of 8 points each. The first output signal contains data points 0, 2, 4, ..., 14 and the second output signal contains data points 1, 3, 5, ..., 15. After that, the algorithm separates these two signals into four signals with four data points for every output signal. the program will keep doing this until there are 16 signals with 1 data point each known as time domain decomposition. The input data length dictates the number of this step. As we can see after the program separates data and the results are rearranged. In the next step, the algorithm uses the Fourier transform to obtain frequency information. Then, it combines the frequency data known as frequency domain synthesis. The step requires three loops. The outer most loop is $\log_2 N$

stage (e.g. 16 data points $N=4$). The middle loops runs through each frequency spectra and the inner most loops is for calculating the points in each individual spectra. The in-depth details of FFT can be found in [Smith. \(1998\)](#).

At this stage, the general background on telescopes and programs has been explained. We will discuss the project preparation in the next chapter.

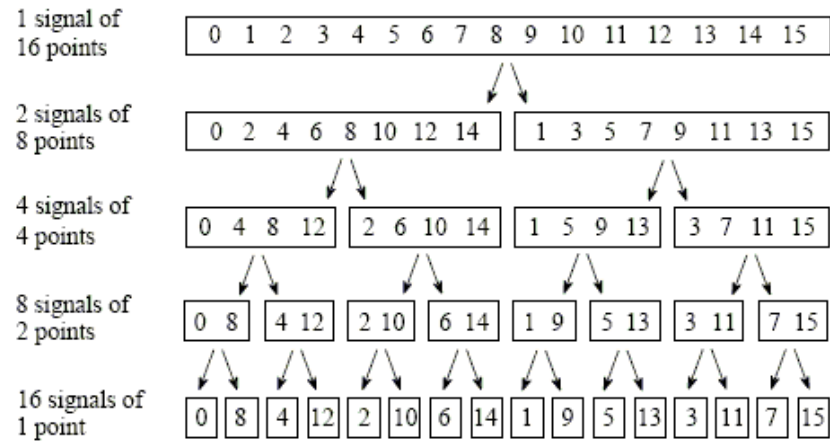


FIGURE 2.8: The FFT decomposition, from 1 signal of 16 points into 16 signals of 1 point by separating the even and odd numbered samples (Figure from [Smith., 1998](#)).

Chapter 3

Project Overview and preparation

The previous chapters have detailed the background knowledge, telescopes, and widely-used standard softwares in pulsar astronomy necessary for this project. In this chapter, the MeerKAT survey preparation will be explained covering several topics: the planning and scheduling of observations, as well as source selection and candidate filtering. Further discussion of these areas and processing is also included, along with a description of in-house built scripts and equations as they become relevant.

3.1 Source selection

The first consideration should be the source selection because the required time to observe every single part of the sky is unfeasible, efficient source selection is a key. We use the unidentified Fermi sources from the LAT 8-year catalogue (4FGL) (Abdollahi et al., 2020). We remove sources that closer than 10° to the Galactic plane because those sources have higher sky temperature and a larger range of expected dispersion measure. Furthermore, because MeerKAT is a southern hemisphere telescope we also exclude sources that have declination over 20° because the maximum elevation of these sources would be undetectable from the site. Next, we remove sources that have r_{95} , the 95 %-confidence error region on the source position calculated by Fermi, larger than 5 arcmins. This helps ensure the telescope beam size covers the source (more details in section 3.3). With these constraints applied, an initial sample of 1336 sources was reduced to only 288. Finally, we exclude sources that have a lower than 5% probability of being a pulsar. Applying the last filter yields a total of 79 sources left on our list (Table. 3.1).

For the probability of being a pulsar (P_{psr}), this work has been done by Colin Clark using “Random forest” technique. Random forest (Breiman, 2001) is a learning method which uses decision trees for classification. The decision trees are created using variables: overall detection significance, curvature significance, variability index (the chi-squared of flux vs time), spectral parameters (spectral index, exponential cutoff energy), and Galactic latitude. The result is from the voting system of the trees to get the most popular class.

The matching between our list has been done with the observed sources from Pulsar Search Consortium (PSC) (Ray, priv. comm.) to find how many sources that have been observed before. The details on PSC can be found in Ray et al. (2012). The reason for the matching is to compare the predicted sensitivity of our sources to previous surveys. An in-house python script is created to check the 4FGL name from our list with the PSC list. Nonetheless, some sources may have been observed before with the findings being attributed to a different name. Therefore, the sky distance cross-matching is required. The program calculates a distance between two sources and examines with a threshold of three times r_{95} . Figure 3.1 shows the result of the program, revealing that 65 sources have been observed before, mostly by the Parkes telescope.

3.2 Survey design

There are several areas which require careful consideration when designing the survey observations. First of all, we needed to think about what kind of sources we are targeting. In this study, we are going to search for pulsars with, young pulsars and millisecond pulsars the most likely types to be detected. Therefore, this survey requires sufficient time resolution to detect very fast pulsars and suitable observing time for acceleration search (see chapter 3.4) note that most MSPs are known to be in binary systems. Secondly, instrument specifications must inform how the observation can be carried out. We already know that we are going to use the MeerKAT radio telescope. However, there are several

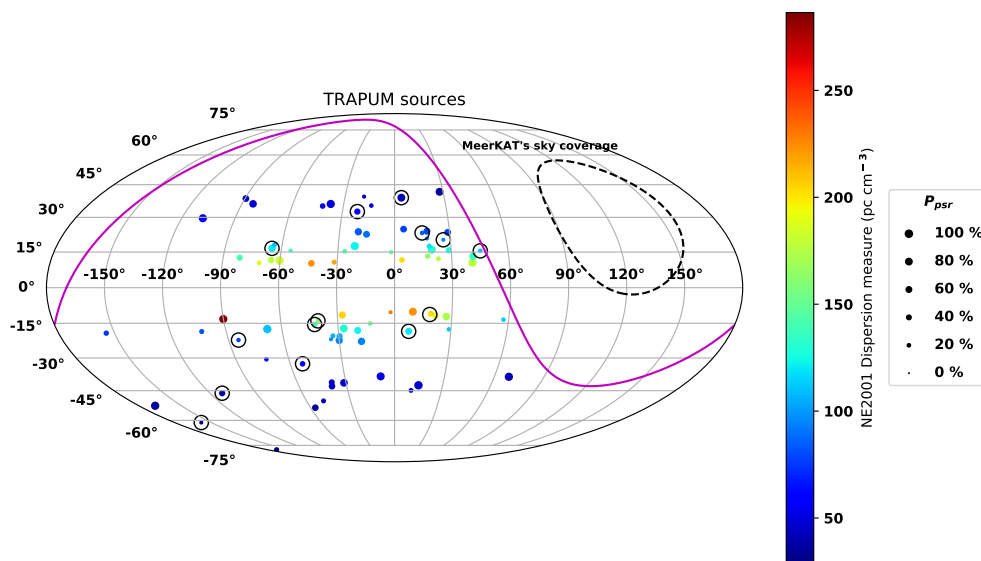


FIGURE 3.1: Targeted sources for our shallow survey of unidentified 4FGL sources projected in Galactic coordinates. The data points use a colour indicative of the maximum DM information along the line of sight from Cordes & Lazio (2002). Sources circled with a black circle represent the ones that have not been observed by the PSC. The purple line is 20° declination which is the threshold for targeted sources. The black line is MeerKAT's sky coverage and the dot size indicates the probability of the source to be a pulsar.

Name	RA	DEC	b	r_{95}	P_{psr}	DM	PSC
J2112.5–3043	318.14001	-30.72930	-42.44355	1.068	0.96	46.8159	True
J1827.5+1141	276.87860	11.68630	10.55460	2.616	0.96	176.9606	True
J1231.6–5116	187.91020	-51.26720	11.48313	2.760	0.96	183.7301	True
J0940.3–7610	145.09891	-76.17940	-17.44946	2.664	0.94	110.2022	True
J0312.1–0921	48.02800	-9.35410	-52.37003	2.928	0.94	35.3578	True
J2212.4+0708	333.10831	7.14280	-38.47989	2.982	0.92	41.1455	True
.
.
.

TABLE 3.1: The example of the first six sources from the full list of 79 4FGL sources selected for the MeerKAT shallow survey run by the Fermi Working Group under the TRAPUM collaboration. Name of the target refers to the 4FGL name (Abdollahi et al., 2020). RA and DEC are in the epoch of J2000. The Galactic latitude is represented as b . r_{95} is the 95 %-confidence error region on the source localisation in arcminutes. P_{psr} is the probability of the source being a pulsar according to the machine learning classification (Random forest). DM is the maximum dispersion measure from the NE2001 model (Cordes & Lazio, 2002). The PSC column refers to whether a source has been searched for in the radio according to the Pulsar Search Consortium (Ray, priv. comm). The full version of our source list can be found in Appendix A.

bands that can be used. The two available options are the L-band and UHF (see table 2.1), each with their advantages and disadvantages. The L-band is less affected by the interstellar dispersion delay than the UHF as it has a higher frequency. However, normally pulsars are brighter at lower frequencies therefore the UHF would appear as superior to the L-band in terms of sensitivity. Lastly, the observing time and schedule, which is the sequence of the object in the observing blocks, needs to ensure that source observations provide an optimal combination of beam size projected on the sky and sensitivity (due to elevation-dependent gain).

3.2.1 Sensitivity of previous surveys

Starting with the observing time, we want to design our survey to be competitive and improve upon previous observations that have been performed. Our first step is therefore to work out the time required for MeerKAT in its current configuration to reproduce the estimated flux density limit achieved in other surveys. The radiometer equation is crucial for this task as it enables us to determine the flux density that can be detected given the parameters of the instrument. The minimum flux density of pulsar can be written as (Lorimer & Kramer, 2005)

$$S_{\min} = \frac{S/N T_{\text{sys}}}{\beta G \sqrt{n_{\text{pol}} t_{\text{obs}} \text{BW}}} \sqrt{\frac{W}{P - W}} \quad (3.1)$$

where S/N is the signal to noise ratio, β is the correction factor due to digitisation, T_{sys} is the system temperature, G is the gain, n_{pol} is the number of polarisations, BW is the bandwidth, t_{obs} is the observing time, P is the pulsar period, and W is the pulse width.

In this project, we compare both MeerKAT L-band and UHF with previous surveys conducted with other telescopes, namely the Parkes telescope, the Green Bank telescope, the Arecibo telescope, and the Effelsberg telescope. We constrain some parameters to ensure a fair comparison. To this end, we fix the signal to noise ratio to 10, and the correction factor to 1. In this discussion, the number of polarisation is 2 and we assume that pulsars ($P = 1$ ms) have a pulse profile with an effective width corresponding to 10% of the pulse period.

Parameter	Parkes	GBT	Arecibo	Effelsberg
T_{rec} (K)	25	18	64	25
Gain (K/Jy)	0.735	2	10	1.5
t_{obs} (minutes)	60	45	76	76
Bandwidth (Hz)	256	200	68.75	240
Centre frequency (Hz)	1390	820	327	1360

TABLE 3.2: Instrumental specifications for the four main surveys and telescopes using to search for pulsars associated with Fermi unidentified sources. The parameters for Parkes, GBT, Arecibo, and Effelsberg are from [Camilo et al. \(2015\)](#), [Ransom et al. \(2010\)](#), [Cromartie et al. \(2016\)](#) and [Barr et al. \(2012\)](#), respectively.

3.2.2 System equivalent flux density

In order to compare the other work with our planned MeerKAT survey, we need to determine some of the missing technical specifications for our instrument. At the time of performing this thesis work, MeerKAT was in its commissioning phase and so we needed to derive the effective T_{rec} and gain from system equivalent flux density (SEFD) information (Table 2.1) that has been provided to us (Serylak, priv. comm.). Figure 3.2 shows the measured SEFD. There are some frequency gaps from 1100 to 1300 MHz and 1500 to 1600 MHz. These regions have been taken out because of RFI. When calculating T_{rec} , we fitted a smooth polynomial function through the measured SEFD in order to interpolate across these gaps and attenuate some noticeable high and low values which are likely caused by the digital filterbanking system. Our approximation will be sufficient to deduce T_{rec} for the purpose of our comparison, and it was calculated using

$$SEFD = \frac{2kT_{\text{sys}}}{A_{\text{eff}}}, \quad (3.2)$$

where $SEFD$ is the system equivalent flux density, k is the Boltzmann constant, T_{sys} is the system temperature and A_{eff} is the effective area of antenna ([Lorimer & Kramer, 2005](#)).

The effective area of an antenna is the product of telescope efficiency (η_A) and telescope geometric area (A_{geo}). According to (Serylak, priv. comm.), the telescope efficiency

is 83 % and the geometric area, describing the telescope’s dish, 13.5m. By doing this, we can find the gain and system temperature of MeerKAT. The parameters are shown in Table 2.1 as a rough approximation of the real L and UHF band. We assumed the same value for both L-band and UHF, $T_{\text{rec}} = 18.15$ K, and $G = 2.75$ K/Jy (64 dishes).

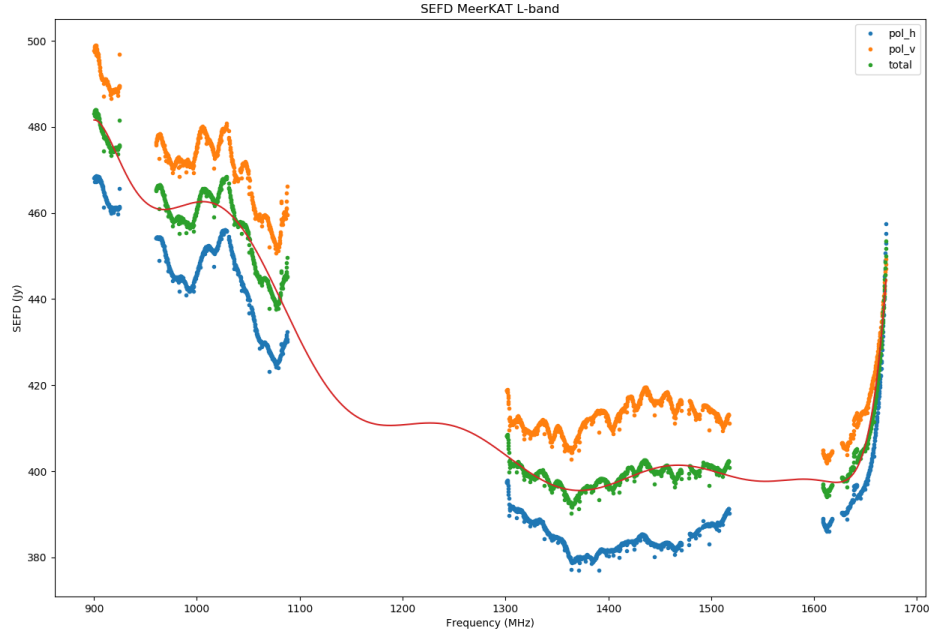


FIGURE 3.2: SEFD throughout MeerKAT’s L-band, the colours orange, blue, and green are polarisation in vertical, horizontal, and total polarisation respectively. The gap between frequencies is due to RFI and error of the data. The results are $\text{SEFD} = 422.44$ Jy, $T_{\text{rec}} = 18.15$ K, $G = 0.043$ K/Jy, and gain for 64 dishes $G = 2.75$ K/Jy

3.2.3 Required integration time

We can rearrange the radiometer equation in order to find the time required to reach the sensitivity of previous surveys with MeerKAT for both the L-band and UHF. We use the approximate SEFD from above, the sky temperature in the direction of each source, and weighting using the spectral index. The sky temperature information is from a python script developed by Rene Breton. The script uses the sky temperature map from [Re-mazeilles et al. \(2015\)](#). For our calculation, we made the same assumption on the minimum signal to noise, pulse duty cycle, and efficiency parameter. The other parameters, such as the bandwidth are taken from Table 2.1. For the minimum flux density, we use the values from each one of the main surveys calculated using the radiometer equation and parameters from section 3.2.2. These survey observations, however, were not necessarily performed at the same frequency as our L-band and UHF receivers. Thus, we need to rescale the flux density values which are calculated from these surveys to what they would be at our MeerKAT frequencies. To do so, we assume that pulsars have

a power law spectrum and consider three scenarios where the spectral index is either 0, -1 , or -2 . as these values cover the typical observed range of the population. Histograms (details in section 3.2.1) displaying the required time for both MeerKAT L-band and UHF compared with Parkes is seen in Figure 3.3, while GBT in Figure 3.4, Arecibo in Figure 3.5 and Effelsberg in Figure 3.6. In each one of them, different colours display one of the scenarios about the value of the spectral index. The result shows that it takes approximately a minute for MeerKAT to reach the same SEFD as 60 Minutes of Parkes observation (1390MHz). For GBT, on the other hand, it takes about 10 minutes or more to reach the same SEFD as 45 minutes of observation. For 76 minutes of Arecibo observation (327 MHz), the required times are very high because Arecibo operates at a lower frequency where pulsars appear to be brighter. Lastly, MeerKAT takes generally takes under 10 minutes to reach the same SEFD as 76 minutes of Effelsberg observation (1360 MHz).

3.3 Scheduling

Scheduling is a step where we design the observing sequence of the sources and their split between observing blocks. Generally, scheduling is a complicated task because a number of observing constraints (i.e. minimum required elevation and size of the source) need to be fulfilled and be optimised simultaneously. The number of permutations in the observing sequence and observing times make the problem more difficult. There are a number of techniques that can be used to plan this process. For example, sorting objects by right ascension (RA) and using Monte Carlo statistical methods to find minimum distance from one source to another or minimum telescope slew time. In this section we describe our approach for scheduling in this survey.

The first criterion is the length of the observing block. Commissioning of the telescope by the technical team demonstrated a phase stability of the array for pulsar observations over a period of a few hours. An observing block of four hours is considered as this is a good compromise of efficiency for MeerKAT as it requires only one phase calibration sequence at the start while maintaining coherence without loss of sensitivity until the end. In light of the work presented in the previous section, we determined that L-band would be used for the first phase of our survey. This is motivated by the fact that its commissioning is at a more advanced stage than UHF, but also given the fact that sensitivity compared to previous surveys is generally as good if not better, in particular with respect to Parkes which provides the most overall with our sky. We established that 10 minutes of observation for each source would provide a net gain in depth, but would also enable us to use the default data reduction pipeline on the MeerKAT computer cluster dedicated to non-imaging observations. Such short observations also imply that the expected change in velocity due to orbital motion will be kept to a minimum, thus reducing the range of acceleration that need to be searched. Given this integration time, approximately 20 sources are required in each block. Our 79 targets there need to be separated into four blocks.

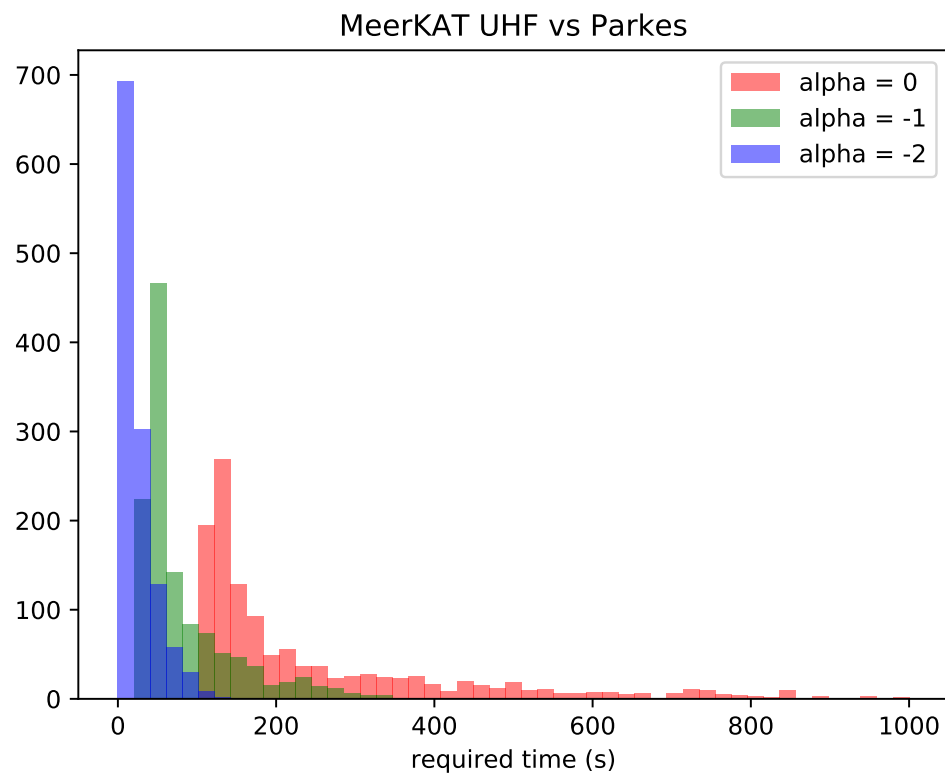
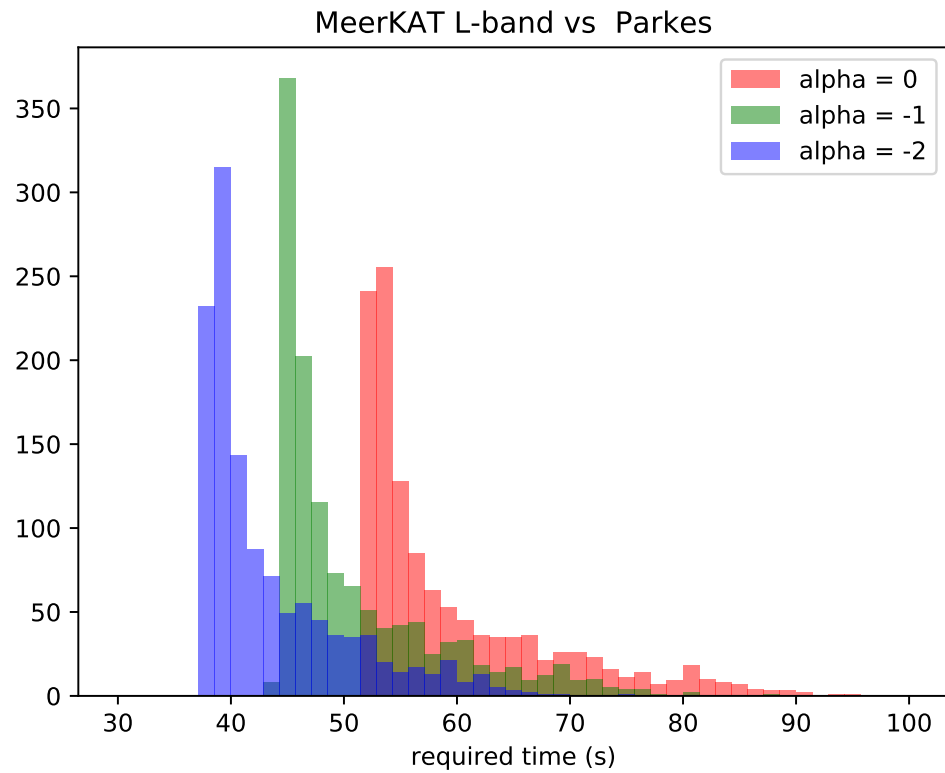


FIGURE 3.3: Histogram of required times for MeerKAT's L and UHF bands to reach the same sensitivity as Parkes (1390MHz). As we can see, it takes about a minute for L-band to reach the same SEFD as 60 Minutes of Parkes observation, assuming the spectral index of 0, -1 , and -2 .

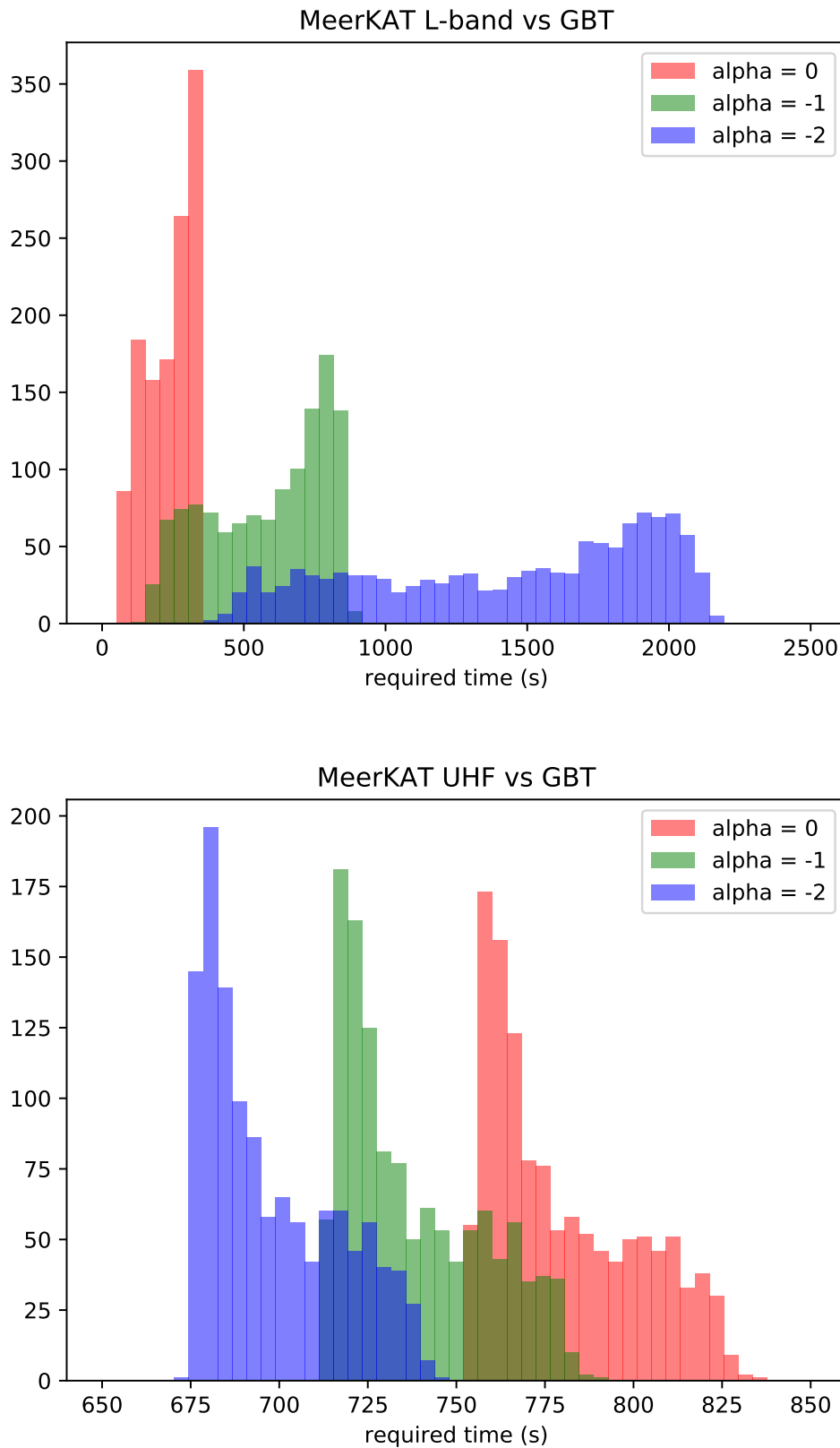


FIGURE 3.4: Histogram of required times for MeerKAT's L and UHF bands to reach the same sensitivity as GBT (820 MHz). As we can see, it takes about 10 minutes or more for L-band to reach the same SEFD as 45 minutes of GBT observation, assuming the spectral index of 0, -1 , and -2 .

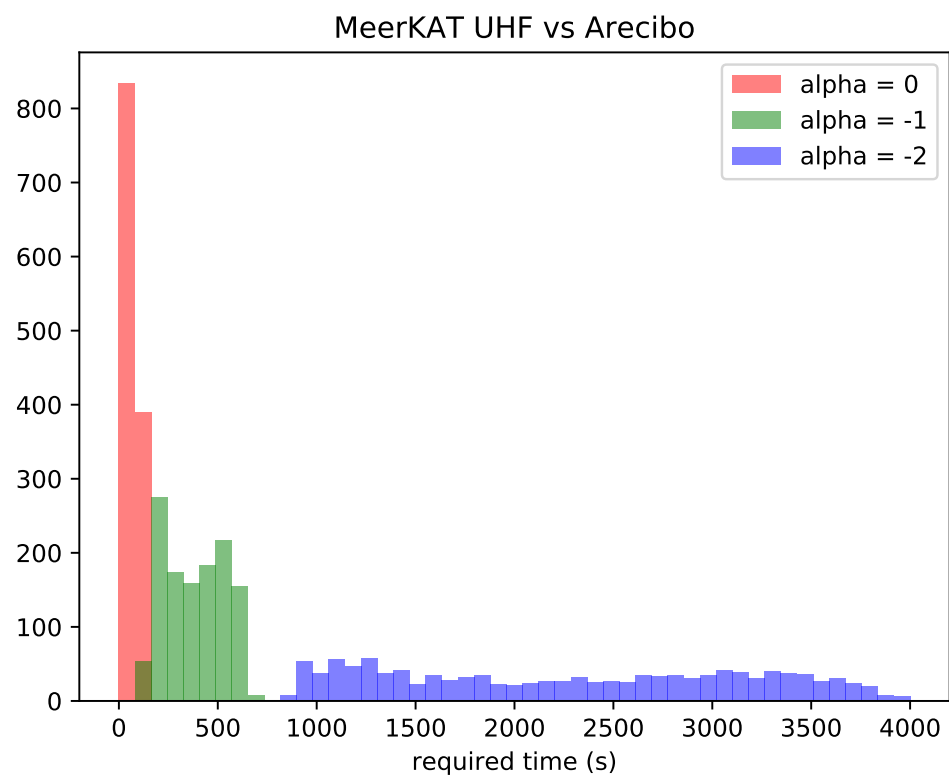
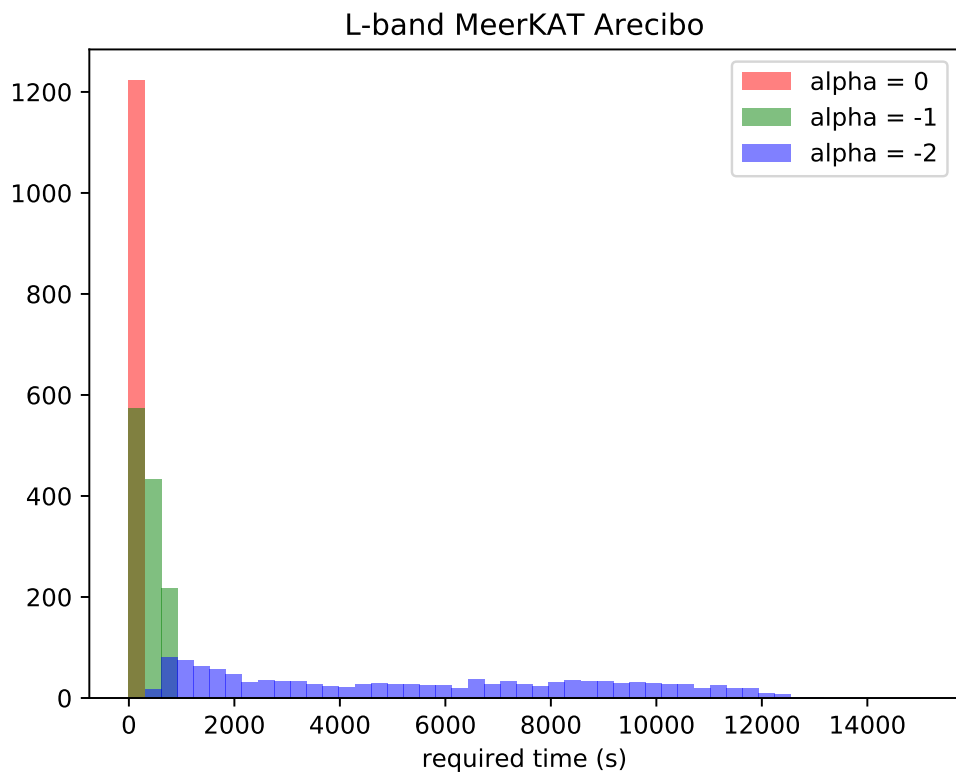


FIGURE 3.5: Histogram of required times for MeerKAT's L and UHF bands to reach the same sensitivity as Arcicbo (327 MHz). As we can see, by assuming the spectral index equal to -2, the required times are very high in both L and UHF bands. One of the main reasons is Arcicbo operates at a lower frequency where pulsars appear to be brighter.

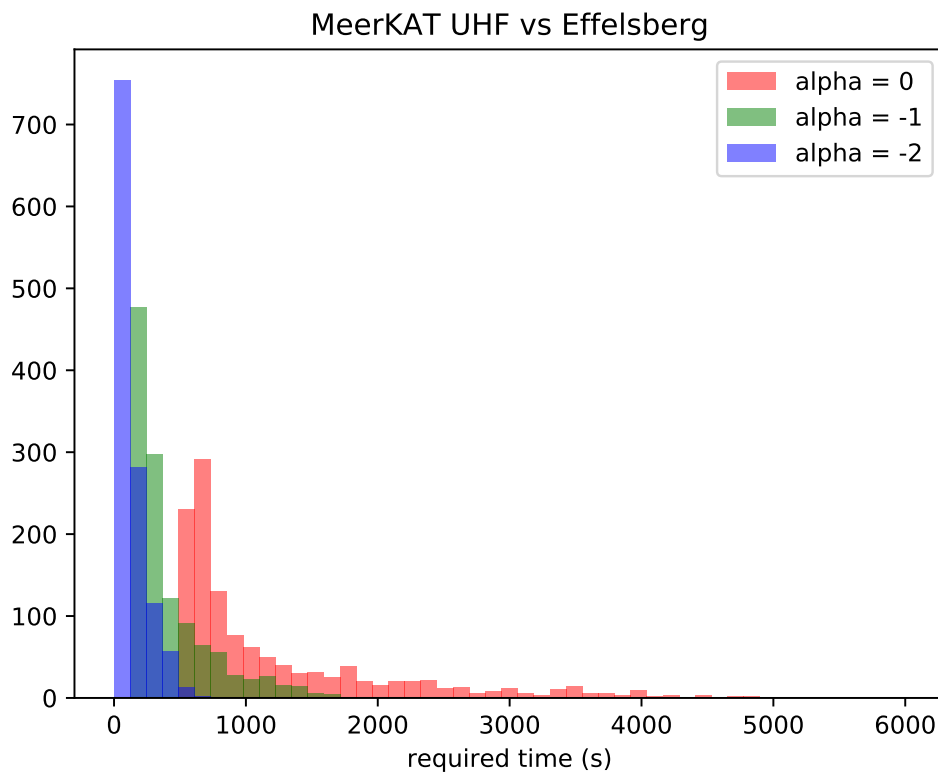
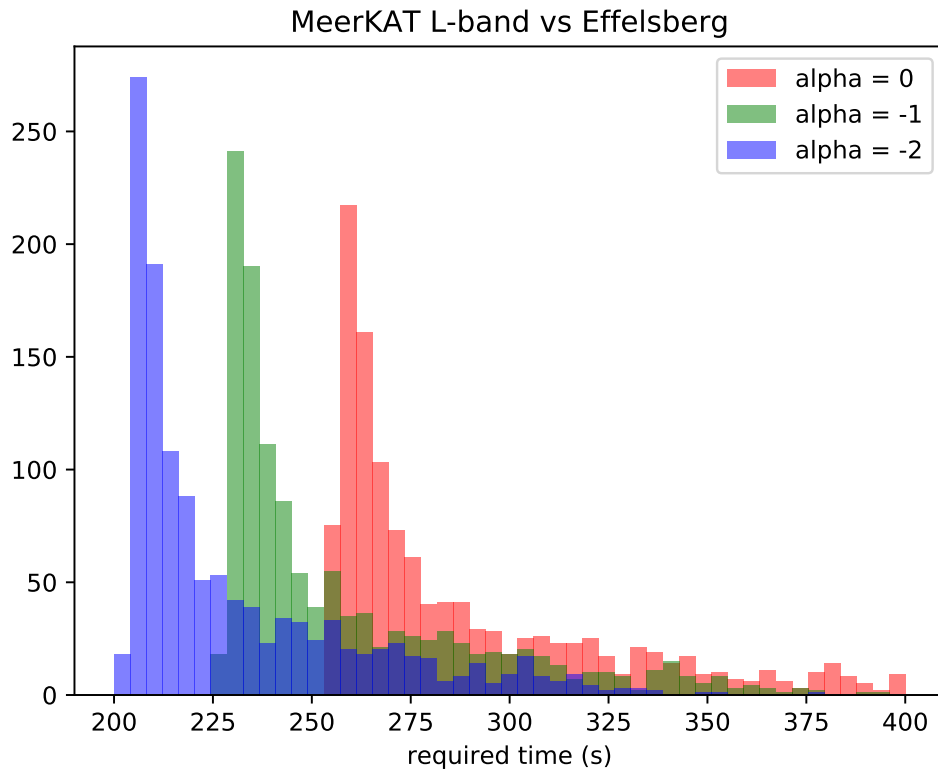


FIGURE 3.6: Histogram of required times for MeerKAT's L and UHF bands to reach the same sensitivity as Effelsberg (1360 MHz). As we can see, it generally takes under 10 minutes for L-band to reach the same SEFD as 76 minutes of Effelsberg observation, assuming the spectral index of 0, -1 , and -2 .

Another aspect to consider is the size of the telescope main beam and r_{95} . The main beam size depends on the number of beams which is fixed for an instrument configuration (number of frequency channels and time resolution) as it depends on the processing power available. For the first pass observation, 288 coherent beams are formed to create the main beam. The main beam size also depends on the elevation, with beam size decreasing with increasing elevation. This effect, which can be seen in Figure 3.7 and is due to the projection of the sky onto the plane of the interferometer layout. Imagine a circular beam at 90° elevation. When pointing the telescope to lower elevation the projection of the beam onto the sky will shift from being circular to becoming increasingly ellipsoidal. For r_{95} , the target can be located in any regions inside r_{95} (the error). Therefore, the total region covered with the tiling of the 288 beams must be larger or equal to that of r_{95} . We can use the elevation to our advantage in order to maximise the total covered sky area as a function of the requirement from each source.

We must also consider the telescope elevation as its effective gain and the amount of RFI will depend on the elevation. We set the minimum elevation at $\sim 30^\circ$ because there are more RFI at lower elevations, especially toward the northern horizon. Moreover, it is recommended that MeerKAT should be used at elevations higher than 15° because its structure can experience high tension at lower elevation.

At this stage, all criteria required for scheduling are determined. The next step is implementing a program which will find an optimal solution. The first technique we use is sorting objects by RA. The result shows that some sources do not match the criteria, therefore, they do not belong in any observing block. Hence, we change the algorithm to sort sources by r_{95} instead. This almost solves the issue, giving a lower number of sources that do not fit in the observing block. However, including every single object in an observing block is required to make our observing program valid. The final technique that solves this problem was developed by Colin Clark. The solution is to check the observable window for all sources, then sorting those by the length of observable time. By prioritising the objects that have a short observable time, it is easier for our Monte Carlo trials to find a solution which fulfils our requirements.

By using the above optimiser, we separate the 79 sources into 4 blocks. Three of them contain 20 sources while the last block consists of 19 sources. The on-source time is 10 minutes, as discussed earlier. When considering an additional 30 seconds to slew the telescope from one target to another, the total time spent on each source will be 10 minutes 30 seconds. Therefore, one block will take around 3.5 hours (see Figure 3.8). The four observing blocks can be found in Appendix B.

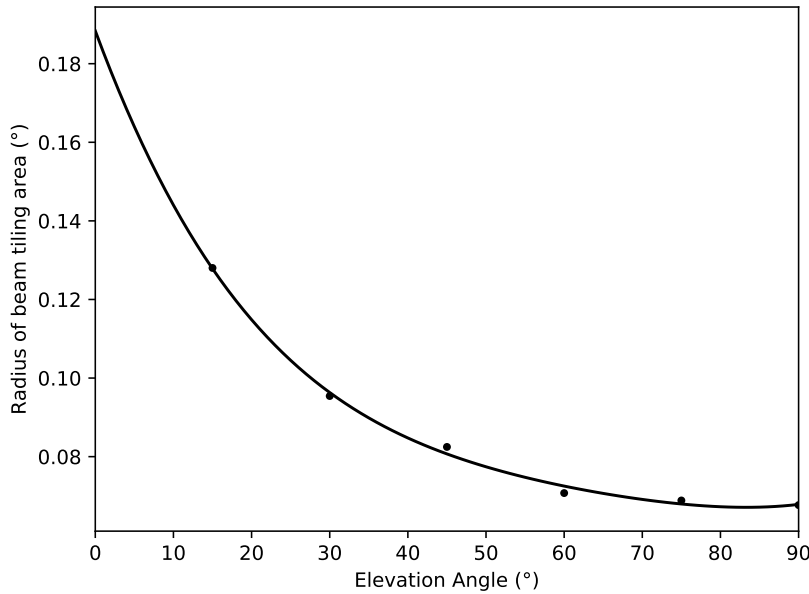


FIGURE 3.7: The plot shows the radius of the approximate circular area covered by 288 coherent beams as a function of elevation, the dots are the beam size information (Chen, priv. comm.) using `tilesim.py` (for more information see chapter 4.2). The polynomial fitting used to find MeerKAT’s beam size at different elevations is represented with the black curve.

3.4 Acceleration search

Acceleration search is a technique used to find pulsations specifically for pulsars in binary systems as the orbital motion will cause a regular pulsation to be Doppler shifted. When the star moves away, the signal is shifted to a lower frequency. On the contrary, when the star moves toward the line of sight, the signal is shifted to a higher frequency. If the orbital motion acceleration is not corrected for, the pulsed signal will be smeared across neighbouring frequency bins in the Fourier domain and result in a lower detection significance, if not a complete loss of the signal. The typical acceleration search involves that that change in pulse frequency of the course of the observation can be described as a linear function. A newer method, dubbed the “jerk search” extends this principle to a second order function and can more efficiently demodulate larger orbital accelerations (at the cost of increased computational resources). A recent review of the acceleration search can be found in [Andersen & Ransom \(2018\)](#).

To design the observation, we assume several binary system parameters. There are four types of binary systems that we could reasonably expect to detect and they cover a range of companion masses. These types are the black widow, redback, neutron star + white dwarf companion, and neutron star + neutron star companion, with companion masses which we assume to be as 0.05 , 0.2 , 1 , and $1.4 M_{\odot}$, respectively. In all cases, we assume that the pulsar has a circular orbit. The set up of two masses is shown in Figure 3.9. Therefore, we can calculate the separation from the pulsar to its companion

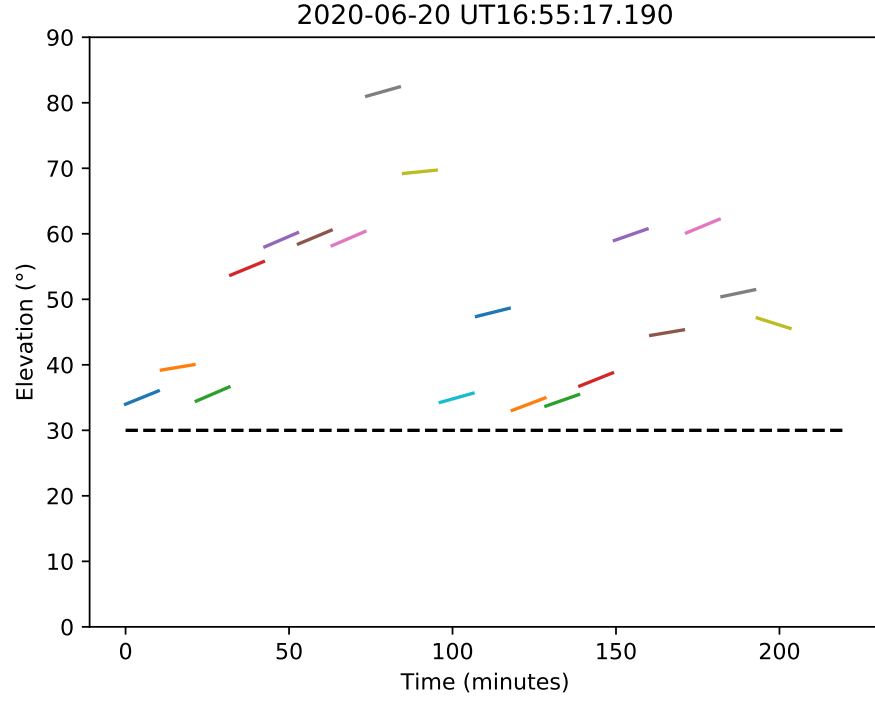


FIGURE 3.8: The elevation of sources from an observing block. The dashed line is the minimum elevation at 30 degrees. The information for every observing blocks can be found in Appendix B.

by equating the centrifugal force to the gravitational force as

$$\left(\frac{mM}{m+M}\right)r\omega^2 = G\frac{mM}{r^2}, \quad (3.3)$$

where m is the mass of the companion, M is the mass of pulsar, r is the separation between two objects, ω is the angular velocity which equals $2\pi/P$, and G is the gravitational constant (i.e. Kepler's third law or orbital motion).

By rearranging the above equation we obtain an expression for the orbital separation as a function of the masses and the orbital period

$$r = \sqrt[3]{\frac{G(m+M)P_{\text{orb}}^2}{4\pi^2}}. \quad (3.4)$$

Then, we can find the distance between the pulsar and the centre of mass of the system, r_M , using the following equation

$$r_M = \frac{mr}{m+M}. \quad (3.5)$$

Following this, we can find the acceleration of the pulsar. Note that the acceleration

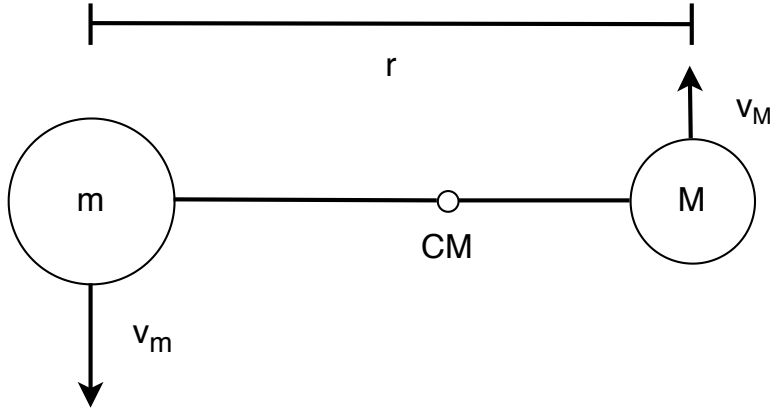


FIGURE 3.9: Schematic of a binary system. In this case, M is a pulsar and m is its companion, r is the distance between the centre of mass of the two objects, CM is the centre of mass of the system, while the arrows represent the instantaneous velocity of each body at a given point in the orbit.

(a) varies throughout the orbit. However, we can calculate the acceleration at its maximum value as

$$a = r_M \left(\frac{2\pi}{P_{\text{orb}}} \right)^2. \quad (3.6)$$

The general requirement of applicability of the linear acceleration search is that the observing time (t_{obs}) must be smaller than $\sim 10\%$ of the orbital period (P_{orb}) (Johnston & Kulkarni, 1991). The equation is described as

$$a = \frac{zc}{hf t_{\text{obs}}^2}, \quad (3.7)$$

where a is the acceleration, z is the number of Fourier bin shifted, c is the speed of light, h is the harmonic number of the considered signal, f is the pulsar frequency, and t_{obs} is the observing time (Andersen & Ransom, 2018).

Results from the expected acceleration are shown in Figure 3.10. The calculation of z has been done using Equation 3.6. The result shows that millisecond pulsars in a spider system (black widow and redback) with an orbital period lower than 2.5 hours can be detected with the observing time of 10 minutes and the acceleration of 50 m/s^2 .

3.5 Pulsar recording setup and processing overview

In this section, we discuss the processing and the candidate filtering that is used for our survey. The set up are DM from 0 to 300 pc/cm^3 with a step of 0.05 pc/cm^3 , sampling time of $76 \mu\text{s}$, 4096 channels, and 288 coherent beams with overlapping at 50 % power. The de-dispersion plan for MeerKAT's L-band is shown in Figure 3.11.

A diagram describing the workflow of the processing is shown in Figure 3.12. First of all, the raw data from the telescope are digitised with the D-engine (the official name for the digitiser). Then they are passed through the F-engine (the official name for the a spectrometer) for channelisation. Consequently, the data go to FBFUSE (The official

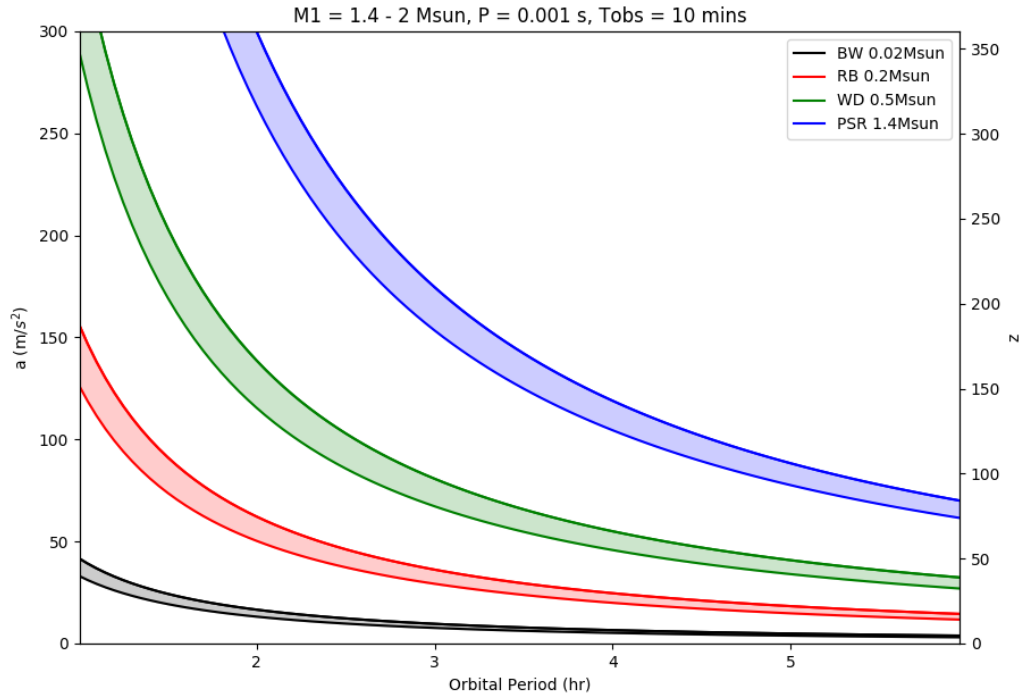


FIGURE 3.10: The plot between the orbital period and acceleration/ z for pulsar binary system with distinct companions. Those are black widow, redback, neutron star - white dwarf, and neutron star - neutron star shown in black, red, green, and blue respectively. The colour region represents the pulsar mass from 1.4 to $2 M_{\odot}$. We use 1 for the harmonic number. Finally, the assumption is the pulsar is a millisecond pulsar with an observing time of 10 minutes. As can be seen, with the acceleration of 50 m/s^2 , we can detect every black widow and redbacks that have an orbital period lower than 2.5 hours.

TRAPUM beamformer) for the beamforming. In the next step, the data are sent to Kubernetes, which is a docker orchestration system that contains DEDISP (de-dispersion from [Barsdell et al. \(2012\)](#)) and the acceleration search pipeline via *Peasoup* (the GPU based acceleration search pipeline) on GPU as well as various steps of candidate filtering, candidate folding and cleaning, and a machine learning classifier. This stage requires the observation file and a user-defined file with the project name, acceleration trials, DM trials, RFI mask, and birdie file. After that, these details are sent in a JSON format to the clusters to run jobs. The searching can be run in different 45 nodes on 45 different files. The output file is an XML file with the potential period, DM, and acceleration of the candidate. After that, the spatial filtration of candidates is performed. The algorithm is developed by Künkel et al. (in prep). The program groups the cluster candidates from different beams and checks against an exponential fit. The detected candidates are grouped to adjacent beams, which can be fitted with an exponential, while RFI typically spreads to all beams (Figure 3.13). After applying the classifier, the data is folded by PulsarX (prepfold). Afterward, *psrconv* is used for changing prepfold's pfd file format to

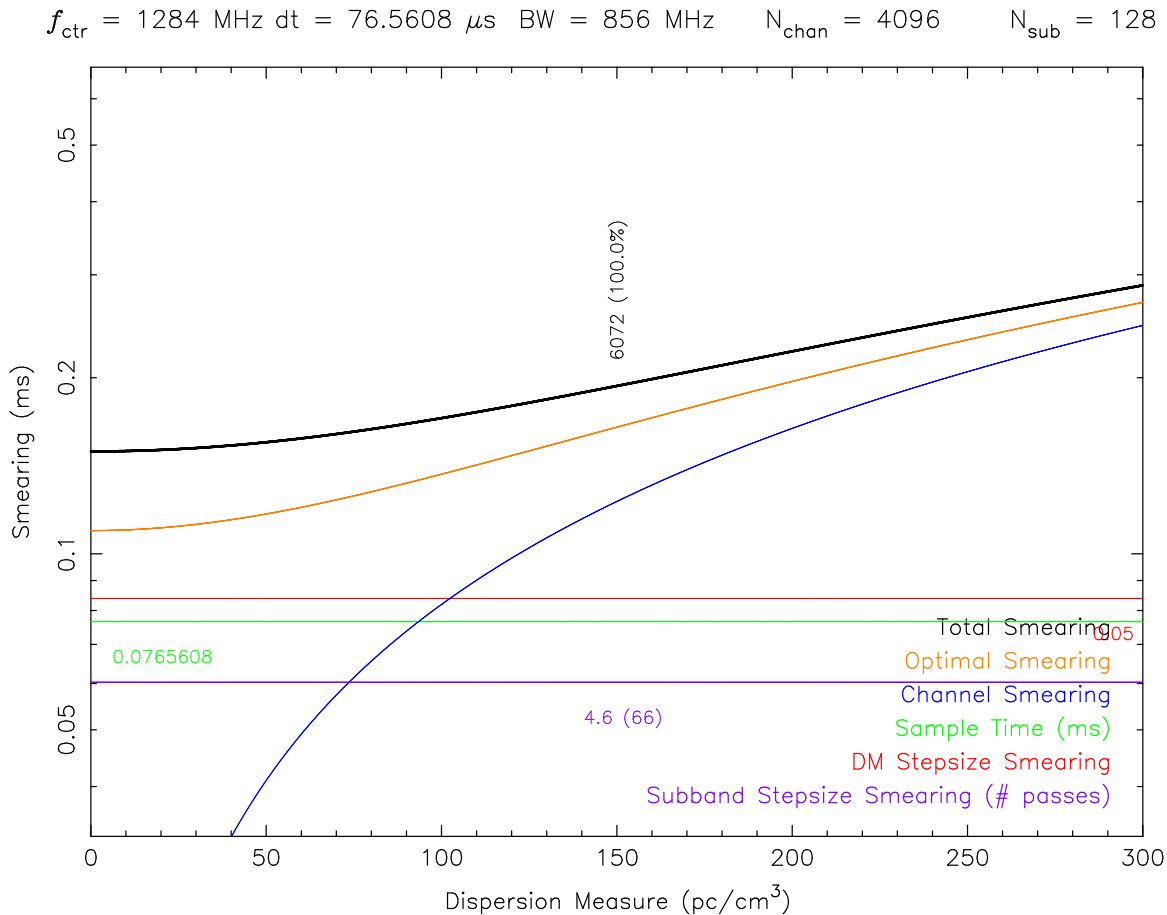


FIGURE 3.11: The de-dispersion plan for MeerKAT’s L-band. As can be seen for this set up, the total smearing is around 0.15 ms at $\text{DM} = 0 \text{ pc}/\text{cm}^3$. It gradually increases to 0.3 ms at $\text{DM} = 300 \text{ pc}/\text{cm}^3$.

PSRCHIVE file format. Subsequently, RFI cleaning is performed using CLFD. Eventually, the machine learning classifier is used for scoring the candidates. Throughout the years, many machine learning methods have been developed for classifying pulsar candidates (Lyon et al., 2016; Tan et al., 2018; Guo et al., 2019). For MeerKAT, the machine learning classifier is from Zhu et al. (2014). In the end, the candidates are plotted using pdmp and saved in PNG format (Figure 3.14). They are packed in a tarball for one observing block and stored in the clusters. This work on pulsar recording setup and processing has been done by Prajwal Padmanabh.

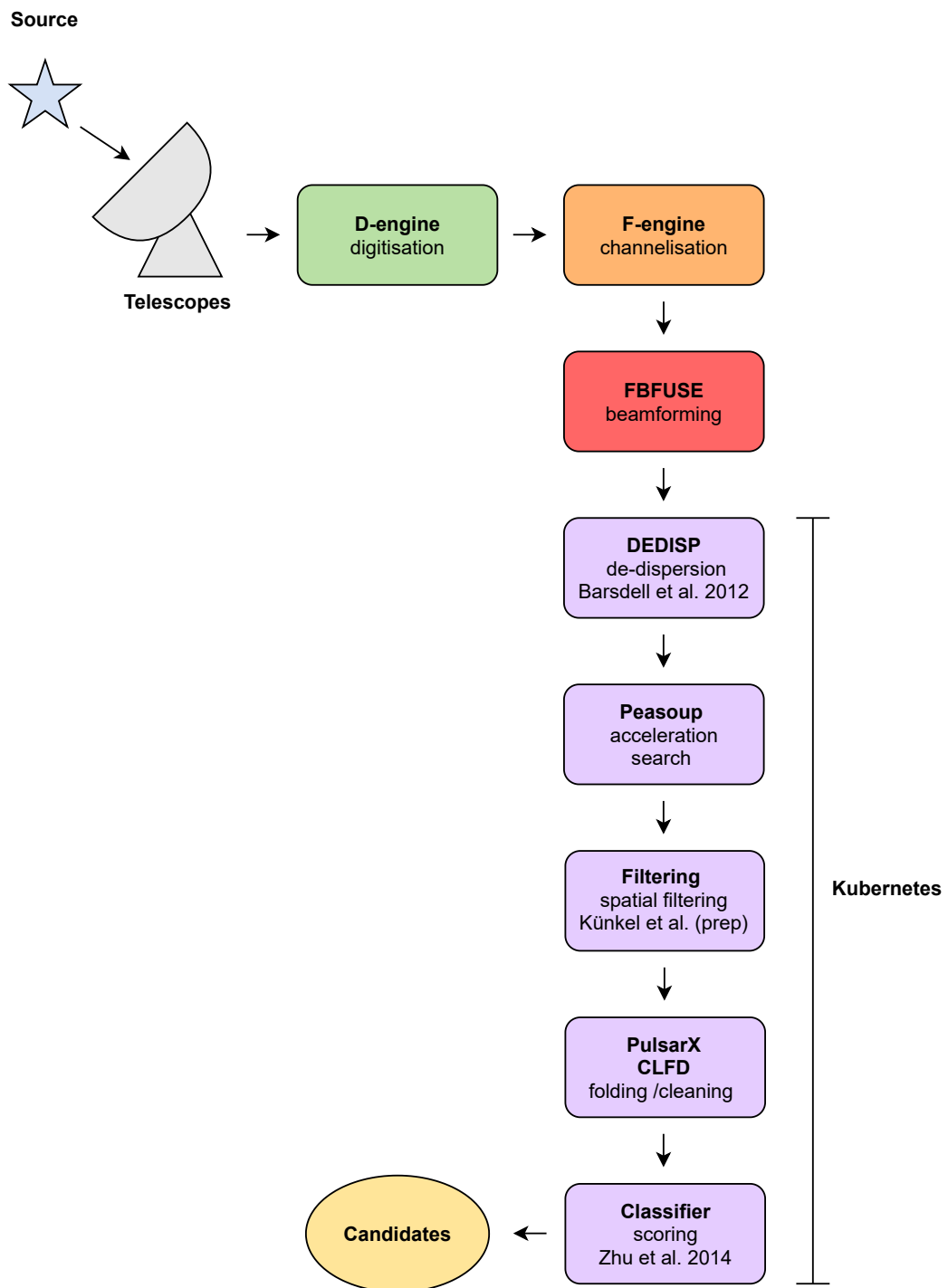


FIGURE 3.12: Processing diagram for MeerKAT. The telescopes detect radio signals, then, the data are digitised and channelised by D-engine and F-engine, respectively. After that, that data go to FBFUSE for the beamforming. The next step is the de-dispersion using DEDISP. Later, the acceleration search is performed by Peasoup. Afterwards, the algorithm applies spatial filtering to the data, subsequently, folding and cleaning by PulsarX and CLFD. The last step is scoring the candidates.

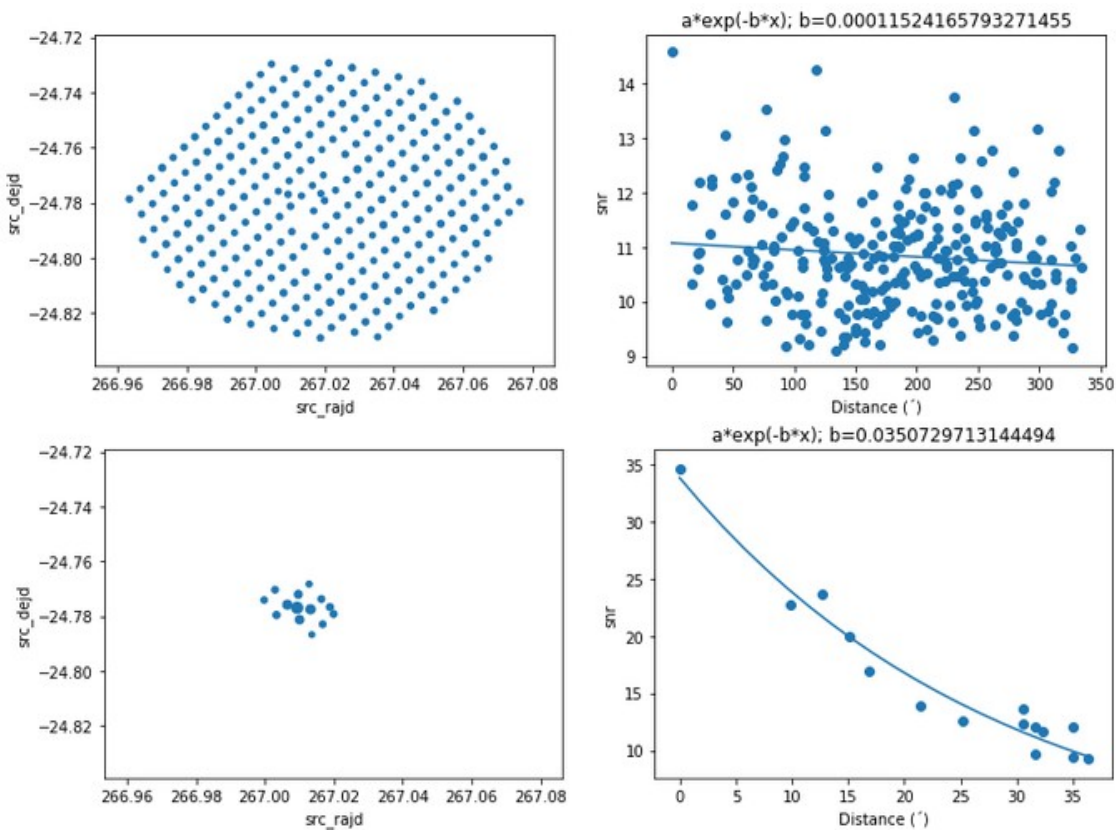


FIGURE 3.13: On the top panel, the RFI with similar strength spreads across the beams (left). On the bottom panel, the harmonics of a pulsar candidate with different strengths appear to be clustered (left). Hence, the result shows the exponential decay from centre detection (right) (Figure provided by Lars Künkel).

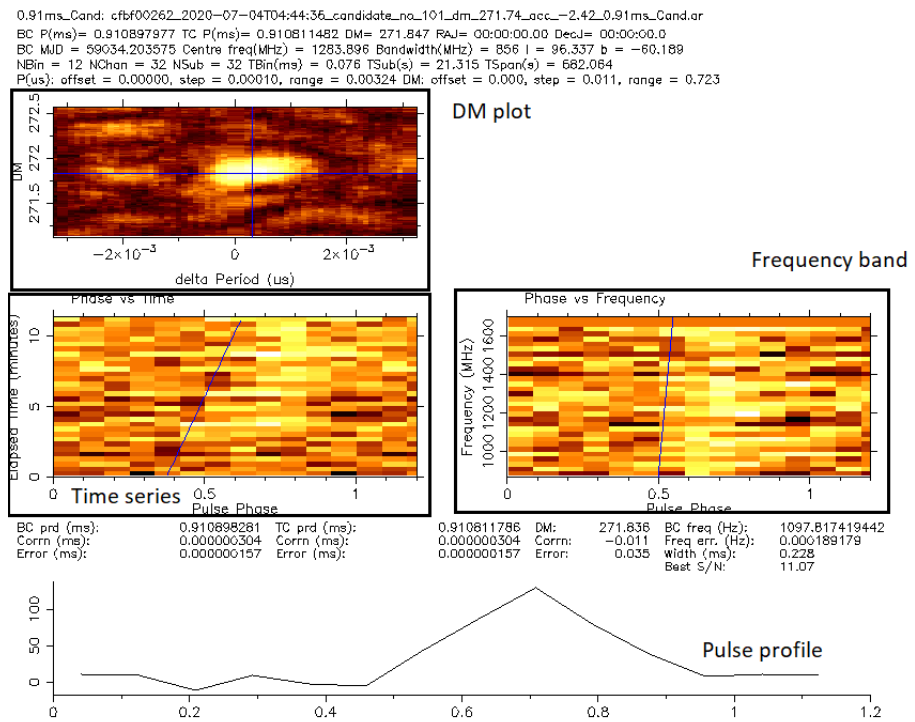


FIGURE 3.14: An example of a PNG file from pdmp. Each plot is shown in colour map where yellow refers to a high flux density while darker colour refers to lower value. On the top is the DM plot with the line that shows the best-fitted DM from DM trials. The better fitted DM provides higher flux density than the worse fitted DM. As a result, the DM plot shows ellipse image. At the centre-left is a time series with the line that shows the profile along the time domain. On the centre-right is the frequency band with the line that shows the profile along with the frequency domain. The pulsar profile is shown at the bottom.

Chapter 4

Survey classification, results, and re-processing

In this chapter, we cover the survey results and discuss the outputs from the search pipeline and classifier. An important step in this process is the candidate classification by humans. To facilitate the work within the collaboration, we built an in-house program to display and classify the candidates, which enables us to aggregate results and vote the suitable signals for follow-up work. From the 13,115 candidates generated by the algorithm, we detected five new, high-quality pulsar-like candidates and one known pulsar. Then, we discuss our work to refine the position of the sources using the capabilities offered by the interferometer in order to prepare optimised follow-up observations. We conclude this chapter with data re-processing to refine the parameters of the candidates.

4.1 Inspection of pulsar candidates

As stated in the previous chapter, the data goes through a filtering stage taking advantage of a machine learning classifier. This helps turn the data into almost-surely non-pulsar and potential pulsar candidates. Typical classifiers are tuned so that the class labelled as pulsar is permissible enough to avoid mislabelling real pulsars as non-pulsars. Nonetheless, it comes at the cost of incorporating a substantial fraction of false positives (i.e. real non-pulsars labelled as pulsars). These candidates need a human's eyes to make a final assessment and confirm them as sufficiently good for follow-up. For the first observing pass of our survey, our automated classification pipeline generated 13,115 candidates labelled as potential pulsars. This represents about 4,000 candidates to further inspect by observing block, or ~ 170 candidates per pointing. Considering that 288 coherent beams are formed on the sky per pointing, our pipeline is capable of reducing the amount of potential signal to inspect to less than one per beam. Manual inspection of the candidates is divided among volunteers from the Fermi Working Group within the TRAPUM collaboration. To assist with this task, we developed a candidate viewing program that enables one to quickly sift through a bundle of candidate diagnostic plots and manually label them.

The candidate viewing program is a simple python program (*labeller.py*) created with the TKinter module for users to label candidates using a graphical user interface. This program ingests a folder containing pulsar candidate files in PNG format. The program displays candidates as illustrated in Figure 4.1. It features functionalities that extract the candidate name and ID from the filename. The program provides several buttons and keyboard shortcuts to perform the inspection tasks swiftly. There are four options provided to label a candidate, those are pulsar (PSR), non-pulsar noise (Noise), non-pulsar associated with radio frequency interference (RFI), and Tier 2 candidates (Tier2), which are candidates worth keeping track of in future observations or display behaviours which stand out from others. Figures 4.2, 4.3, 4.4, and 4.5 display an example from each one of the four types, i.e. PSR, Noise, RFI, and Tier2, respectively. The understanding of classification is a crucial part of this study. Not only that any pulsars candidates are not to be missed, but also misleading candidates should be avoided.

The program has the option to go back and forth between candidates and it can adjust the size of the displayed diagnostic plot to suit various screen sizes and/or user preferences. It is possible to search for a specific candidate using its ID and filter the visible outputs based on one of the labels from above or whether it has been labelled already or not. The classification is updated immediately in the database live local database and upon quitting, the program will automatically save the result in a csv file. The output file contains the names and labels of candidates as shown in Table 4.1.

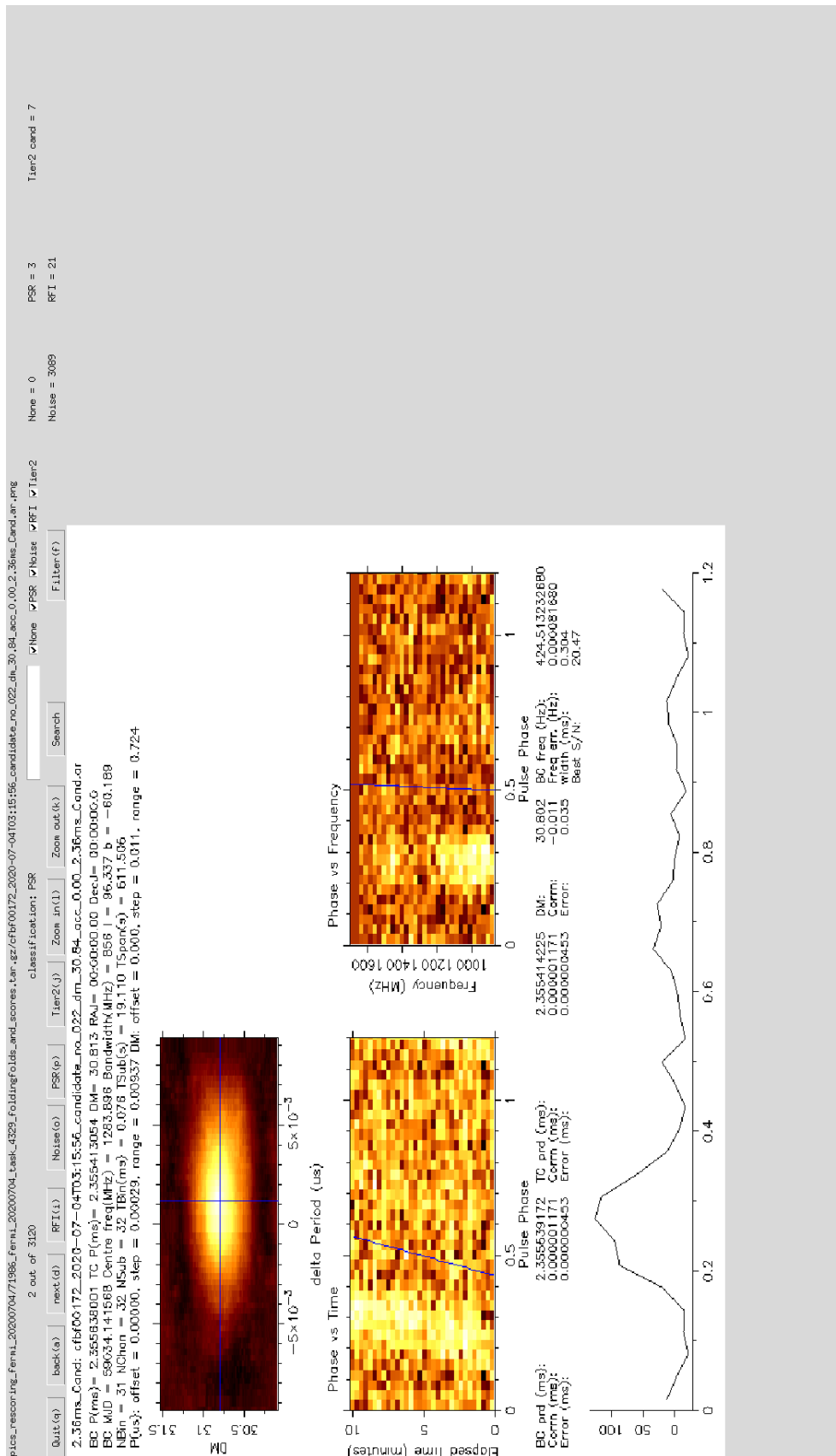


FIGURE 4.1: The candidate labeller program (*labeller.py*) shows one candidate at a time. The user can classify, search, filter candidate types, change the image size, and move between candidates by clicking one of the buttons or press a shortcut key.

2.37ms_Cand: cfbf00088_2020-07-04T02:22:42_candidate_no_013_dm_81.66_acc_0.00_2.37ms_Cand.ar
 BC P(ms)= 2.373518550 TC P(ms)= 2.373291146 DM= 81.660 RAJ= 00:00:00.00 DecJ= 00:00:00.0
 BC MJD = 59034.104627 Centre freq(MHz) = 1283.896 Bandwidth(MHz) = 856 l = 96.337 b = -60.189
 NBin = 31 NChan = 32 NSub = 32 TBin(ms) = 0.077 TSub(s) = 19.477 TSpan(s) = 623.266
 P(us): offset = 0.00000, step = 0.00029, range = 0.00933 DM: offset = 0.000, step = 0.011, range = 0.730

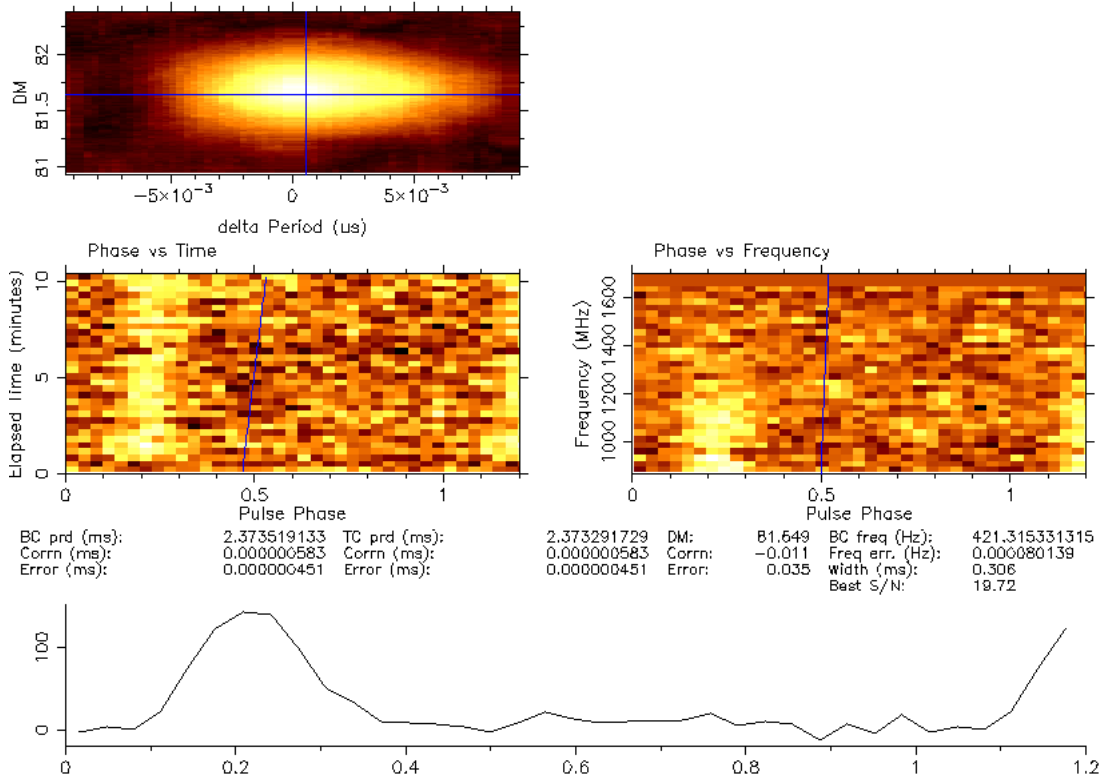


FIGURE 4.2: For an example of PSR candidate, we can clearly see the signal in both time vs phase and frequency vs phase plots, both match the integrated pulse profile of the source at the bottom. The DM vs pulse period plot shows a clear ellipse shape which indicates that the best-fit solution is well localised in this phase space. This particular source has DM with a peak at $81 \text{ pc}/\text{cm}^3$ which is reasonable considering that the maximum predicted DM in this direction is $229 \text{ pc}/\text{cm}^3$. The location of the source concerning the Galactic plane is an important factor in determining the DM range that is reasonable to expect. If the value is more than expected, it is unlikely that the candidate will be a pulsar.

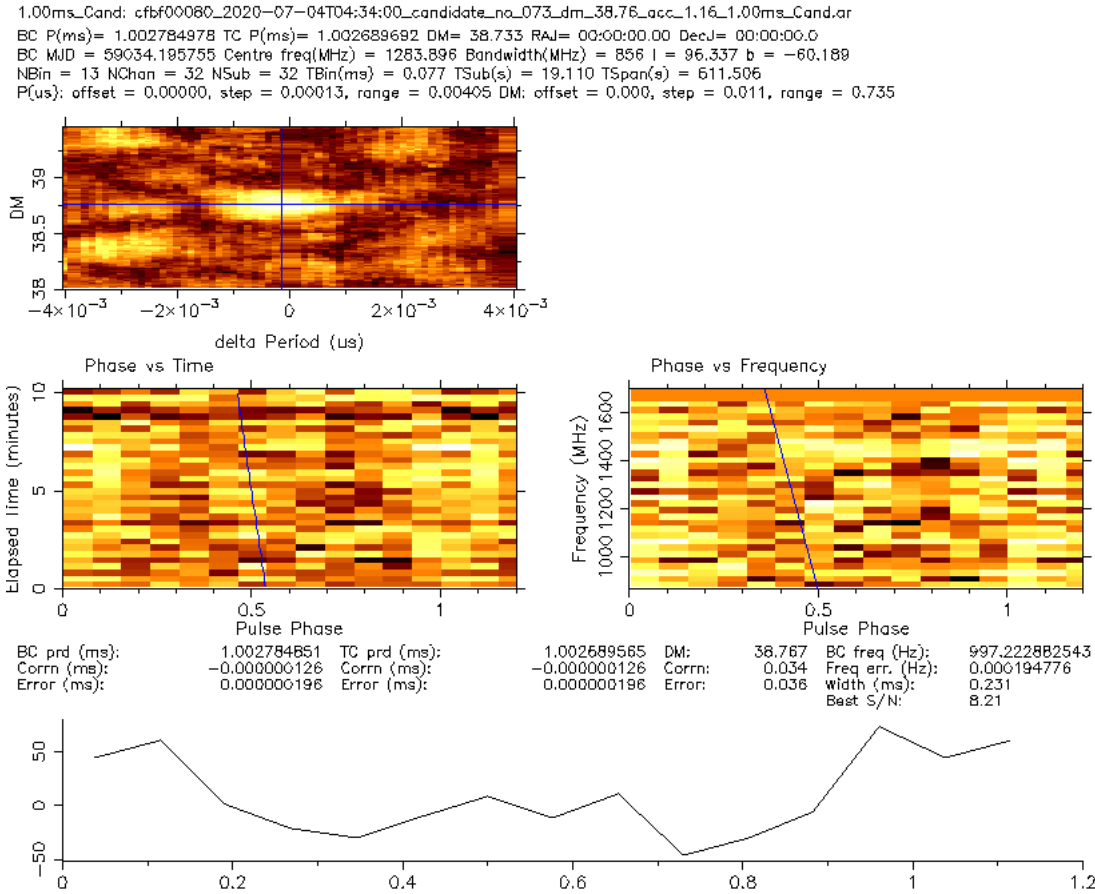


FIGURE 4.3: For an example of Noise candidate, we see none of the plots displays any characteristic feature as seen for the PSR candidate. The integrate pulse profile shows a peak but it is clear from looking at the time vs phase and frequency vs phase plots that this is the result of spurious noise and that no consistent trail pattern is visible. Furthermore, the DM vs pulse period plot shows a localised region of best fit but it is not significantly better than fluctuations seen in the surrounding area.

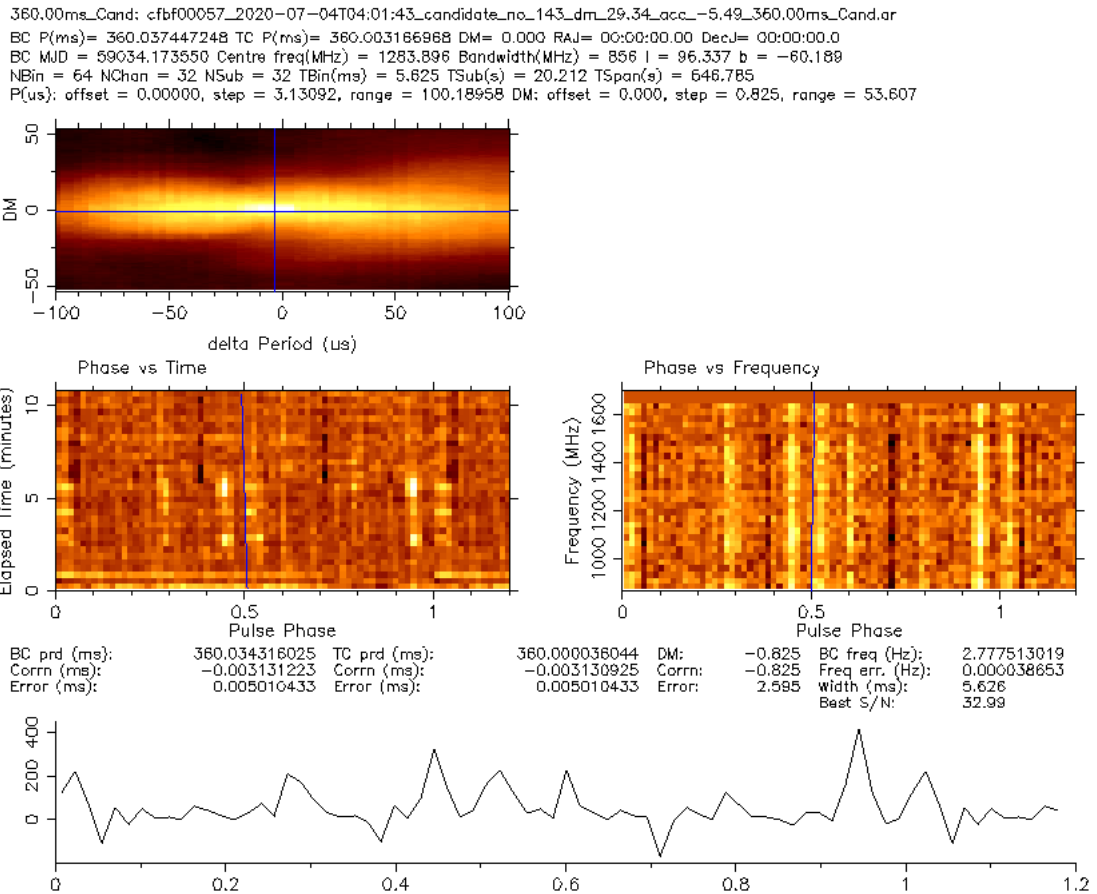


FIGURE 4.4: For an example of RFI candidate, the diagnostic plots clearly show many straight lines, either localised in time or frequency or phase. These features are unlikely caused by random noise fluctuations, but they are clearly not related to the signature expected from a true pulsar and more likely human-generated. Thus, the pulse profile shows multiple narrow peaks. Another typical signature of RFI signals is that the best DM peaks at, or is consistent with, 0. This is because RFIs are produced on Earth or from satellites, which implies negligible dispersion delay affects their propagation.

0.94ms_Cand: cfbf00101_2020-07-04T05:28:42_candidate_no_089_dm_236.20_acc_48.77_0.94ms_Cand.ar
 BC P(ms)= 0.941849897 TC P(ms)= 0.941760695 DM= 236.228 RAJ= 00:00:00.00 DecJ= 00:00:00.0
 BC MJD = 59034.233830 Centre freq(MHz) = 1283.896 Bandwidth(MHz) = 856 l = 96.337 b = -60.189
 NBin = 12 NChan = 32 NSub = 32 TBin(ms) = 0.078 TSub(s) = 19.477 TSpan(s) = 623.266
 P(us): offset = 0.00000, step = 0.00012, range = 0.00379 DM: offset = 0.000, step = 0.012, range = 0.748

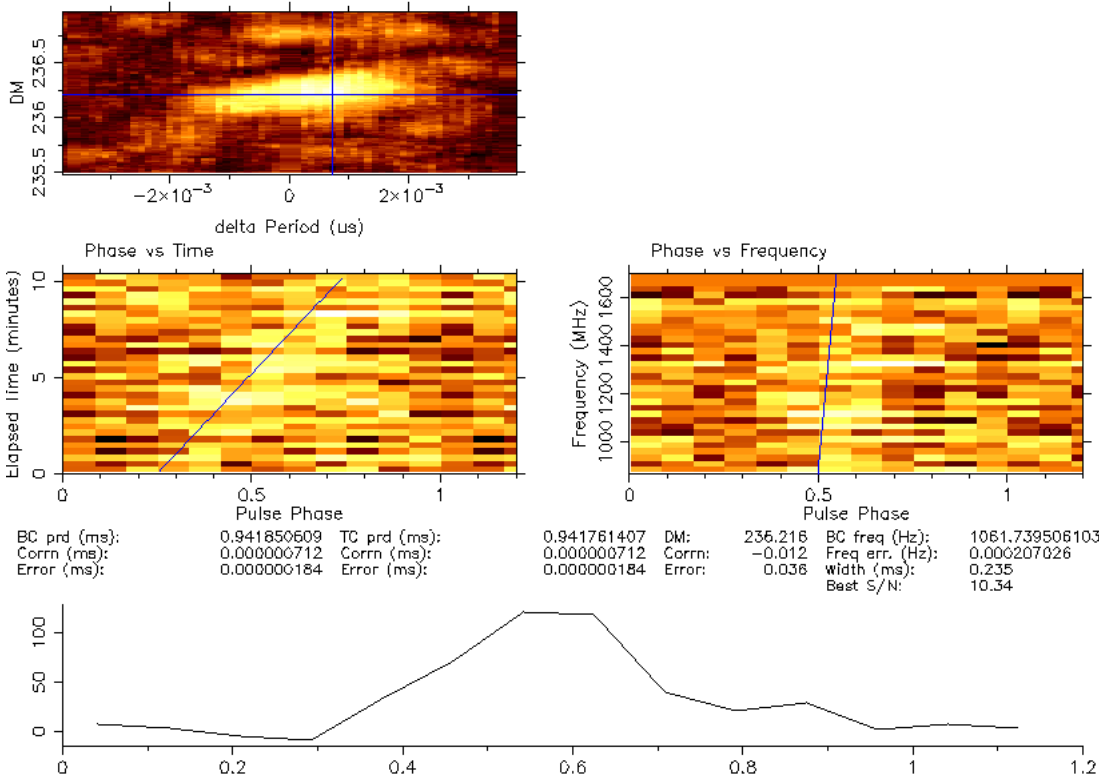


FIGURE 4.5: For an example of Tier 2 candidate, the classification is the trickiest and the most ‘controversial’. Some hint of a trail in the time vs phase and frequency vs phase can be seen but is not very strong. In the DM vs spin period plot, for this particular candidate, the DM peaks at around 236 pc/cm^3 which is more than the maximum DM value along the line of sight which is 58 pc/cm^3 . It is not impossible that a specific line of sight goes through a higher density of electrons (e.g. if it overlaps with an HII region, for instance), but this clearly stacks the odds against it being a true pulsar. Nonetheless, some of the more borderline candidates like this one are kept in case further occurrences happen in new observations.

Name	Type	PSR	Noise	RFI	Tier2
cand1.png	PSR	True	False	False	False
cand2.png	PSR	True	False	False	False
cand3.png	RFI	False	False	True	False
cand4.png	Noise	False	True	False	False
cand5.png	RFI	False	False	True	False
cand6.png	Noise	False	True	False	False
cand7.png	Tier2	False	False	False	True
.
.
.

TABLE 4.1: The example of result file generated by *labeller.py*. Labels are stored as a Boolean so that results from multiple can be quickly aggregated and filtered.

Name	RA	DEC	DM	P(ms)	Batch	N_{beams}	Type
J1526.6-2743	15:26:45.89	-27:44:05.7	30.996	2.489	0620	253	PSR
J1803.1-6708	18:03:04.00	-67:07:40.9	38.362	2.134	0620	253	PSR
J1823.8-3544	18:23:43.04	-35:43:26.5	81.649	2.373	0704	288	PSR
J1858.3-5424	18:58:09.67	-54:22:13.9	30.802	2.355	0704	288	PSR
J1906.4-1757	19:06:15.51	-17:54:31.6	98.060	2.877	1010	288	PSR
J1717.5-5804	17:17:35.83	-58:00:13.5	124.560	321.783	0620	252	KnPSR
J0251.1-1830	02:51:25.08	-18:30:59.7	280.56	2.741	0704	288	Tier2

TABLE 4.2: List of pulsar candidates from the first pass of our survey, that is, sources classified as PSR or Tier 2. Name is the 4FGL name and RA and DEC are the centre of the coherent beam in which the candidate is detected. N_{beams} is total number of coherent beams in the pointing. DM and P are the best-fit dispersion measure and spin period generated by Peasoup. Batch is the observing ID. KnPSR stands for a known pulsar, which was fortunately detected by our pipeline.

The usual process of human inspection of the candidates involves having more than one person look at each candidate. This multi-person strategy increases robustness against biases and avoid missing worthy candidates due to, e.g., human factors, such as fatigue. We aggregated and analysed the scores from all users. We aimed to have each candidate ranked by at least four different persons. Consequently, we set a threshold that if at least one person classifies a candidate as PSR, this candidate will be retained for a further group discussion at a collaboration meeting since we do not want to miss any possible pulsars. Overall, this process only generated a handful of candidates to discuss for a final decision on its ranking. Another criterion was so so that if two or more people classified a candidate as Tier 2, this candidate would enter the final Tier 2 candidate list. We present five discovered pulsar-like candidates and one known pulsar in Table 4.2. There are $\sim 12,000$ Noise candidates, ~ 750 RFI candidates, ~ 150 Tier2 Candidates note that noise, RFI, and Tier2 are arbitrary. Therefore, the numbers of these three categories should be taken as indicative only.

4.2 Localisation

After identifying possible candidates, the next step is to find/refine their position using a localisation. Indeed, a real astronomical source is likely to be detected in multiple adjacent beams, and the significance of the detection in each of them should be proportional to the sensitivity of the given beam at the true position of the source. Solving this problem requires one to have an accurate description of the two-dimensional beam profile.

For this project, we use a python script (*tilsim.py*) written by Weiwei Chen to calculate the beam profile. This program requires the antenna layout information (via a csv file), then (centre) frequency of the receiver at which to calculate the profile (i.e. 1284 MHz for the L band), the pointing direction, the date and time at which the observation is taking place, the total number of beams and their overlap. For our first pass of the survey, we used nominal 0.5 overlap, which means that adjacent beams would in theory overlap at the point where their sensitivity is half that of the boresight. The sub-array which is the ID of used antennas is required for the program to form a beam profile. Lastly, The output file is generated with defined. The program generates the point spread function (PSF) shown in Figure 4.6.

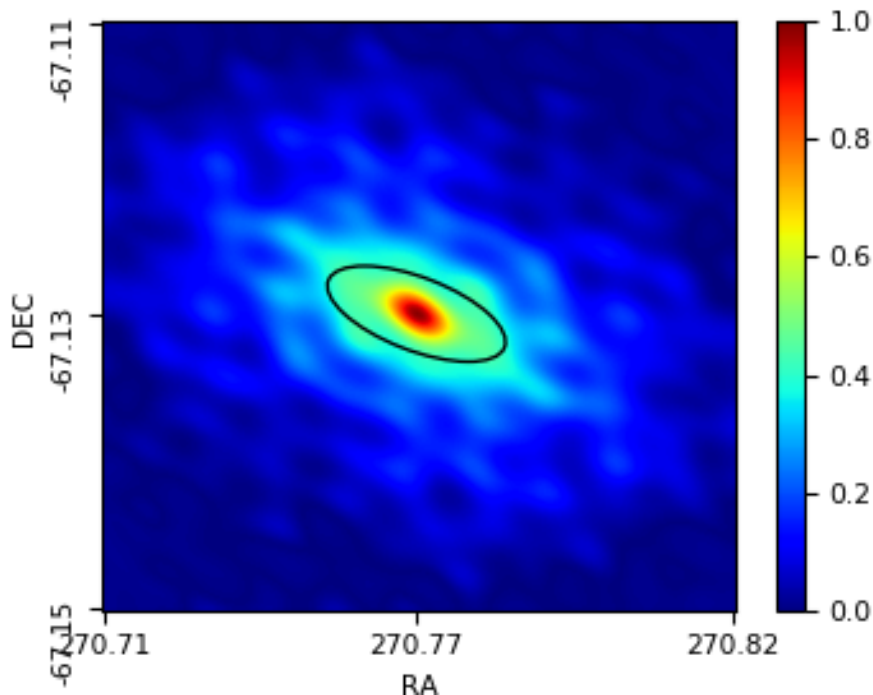


FIGURE 4.6: The point spread function (PSF) of the centre beam of our tiled array at 1284 MHz generated by *tilsim.py*. The ellipse is drawn at the half value of the maximum power level.

Once we have a good description of the beam shape, another program uses this information along with the detection signal-to-noise of various beams to work out the position of the pulsar. We use *SeeKATmain.py* for the localisation, a program written by Tiaan

Bezuidenhout. The algorithm uses the PSF result from *tilsim.py* and a text file that contains the beam position and signal-to-noise from each detection. The program uses this to weigh the likelihood of the position and produces a probability heat map representing the location of the source (see examples in the coming sections).

In the remainder of this chapter, we present the properties, discovery fold plot, and localisation map of each one of the 5 candidate pulsars that we found. In addition, we first show our work based on the already known pulsar J1717–5800 in order to demonstrate that it works as a test case.

4.3 J1717.5–5804, aka PSR J1717–5800

J1717.5-5804 has been detected in the first batch of the observation on 2020-06-20 at 18:41:55. This source has an optimised DM at 125.34 ± 2.32 pc/cm³, a period of 321.824 ms, and an acceleration of 1.86 ± 14.92 m/s² (Figure 4.7). This candidate produced by our pipeline is a known pulsar, PSR J1717–5800. The true spin period and DM of this pulsar are 321 ms and 125.22 pc cm⁻³ (Manchester et al., 2005), in agreement with the values found by our pipeline. It is an isolated pulsar, however, upon further investigation, we found that the acceleration measure reported by the pipeline is compatible with 0. We can check whether PSR J1717–5800 is likely associated with the Fermi source or not. This pulsar has an $\dot{E} = 2.32 \times 10^{32}$ erg/s (Edwards et al., 2001), which is considerably lower than the threshold power of $\dot{E} \sim 10^{33}$ erg/s required for typical pulsars to be gamma-ray bright (Smith et al., 2019). Therefore, we can rule out its associated with the gamma-ray source.

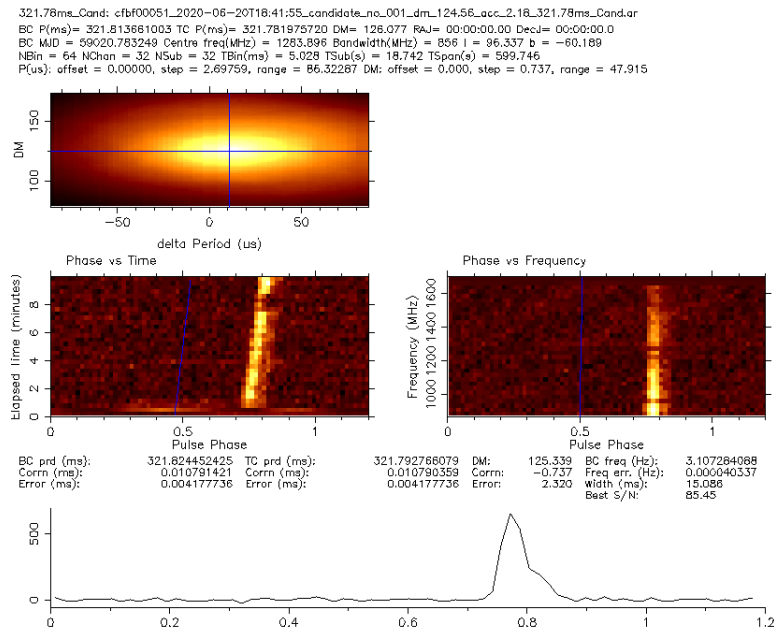


FIGURE 4.7: Original fold detection of J1717.5–5804. The pulsed signal is strong. The pulse can be identified through both time and frequency in the folds as a function of spin phase.

Beam	RA	DEC	S/N
cfbf00051*	17:17:35.83	-58:00:13.5	71.50
cfbf00023	17:17:40.17	-58:00:35.4	21.55
cfbf00025	17:17:40.94	-58:00:17.1	24.83
cfbf00049	17:17:35.05	-58:00:31.7	23.83
cfbf00053	17:17:36.61	-57:59:55.3	41.00
cfbf00104	17:17:29.94	-58:00:28.1	12.33
cfbf00106	17:17:30.72	-58:00:09.9	22.16
cfbf00108	17:17:31.50	-57:59:51.6	16.27

TABLE 4.3: The detection of J1717.5–5804 and neighbouring beams using for localisation. The detection is at the boundary of the beams. Thus, there are only 7 surrounded beams instead of 8.

Given that the true location of the pulsar is known, we decided to use it as a benchmark for our localisation work. We present the beam position and signal-to-noise information in Table 4.3. The probability map produced by our analysis is shown in Figure 4.8 and full information for beam tiling and position can be found in Appendix C. On the right-hand side, the colour bar depicts the probability from 0 to 100 percent in black to red. The green contour represents the location where the 68% probability region, while the cyan contour, on the other hand, exhibits the 90% probability region. The white contour is the beam shape at the half power point. The red cross indicates the true position of the pulsar as measured using pulsar timing.

We notice that the likely position from our analysis is different from that of the red cross. We note that RFI can noticeably influence the signal-to-noise measured in a beam, which will directly lead the weighting used for the probability of localisation to be wrong if the RFI excision is not the same for all beams. For this reason, we have reprocessed all of our candidate data in order to obtain RFI-free, consistent folds. Several steps are involved in this vital quality assurance process. The first step is to re-folding the data to check the folding parameters and folding format are consistent. After re-folding the data, we use the interactive program *paz* to zap the RFI from all archive files on pre-selected frequency channels. Then, the RFI cleaning program CLFD is run on the beam with the most significant detection. This enables us to generate an RFI mask which we can apply in the same way to all other neighbouring beams. Applying the same RFI masking on all beams ensures that we retain the same weighting and sensitivity. For the next step, *PDMP* is run on the RFI-masked brightest beam to optimise the period/DM. We then apply the same optimised period/DM to the RFI-masked adjacent beams. Finally, we use *psrstat* to consistently extract the signal-to-noise of the candidate from each beam. There are other several reasons that influence the localisation result. Firstly, the beam shape has a plateau and drops quickly after. Hence, localisation of the target in the secondary lobes has poor accuracy. Secondly, the bandwidth is large therefore the beam shape and size change dramatically from the high and the low frequencies. This motivates the idea of splitting the band into smaller chunks and evaluate the probability for each of them individually.

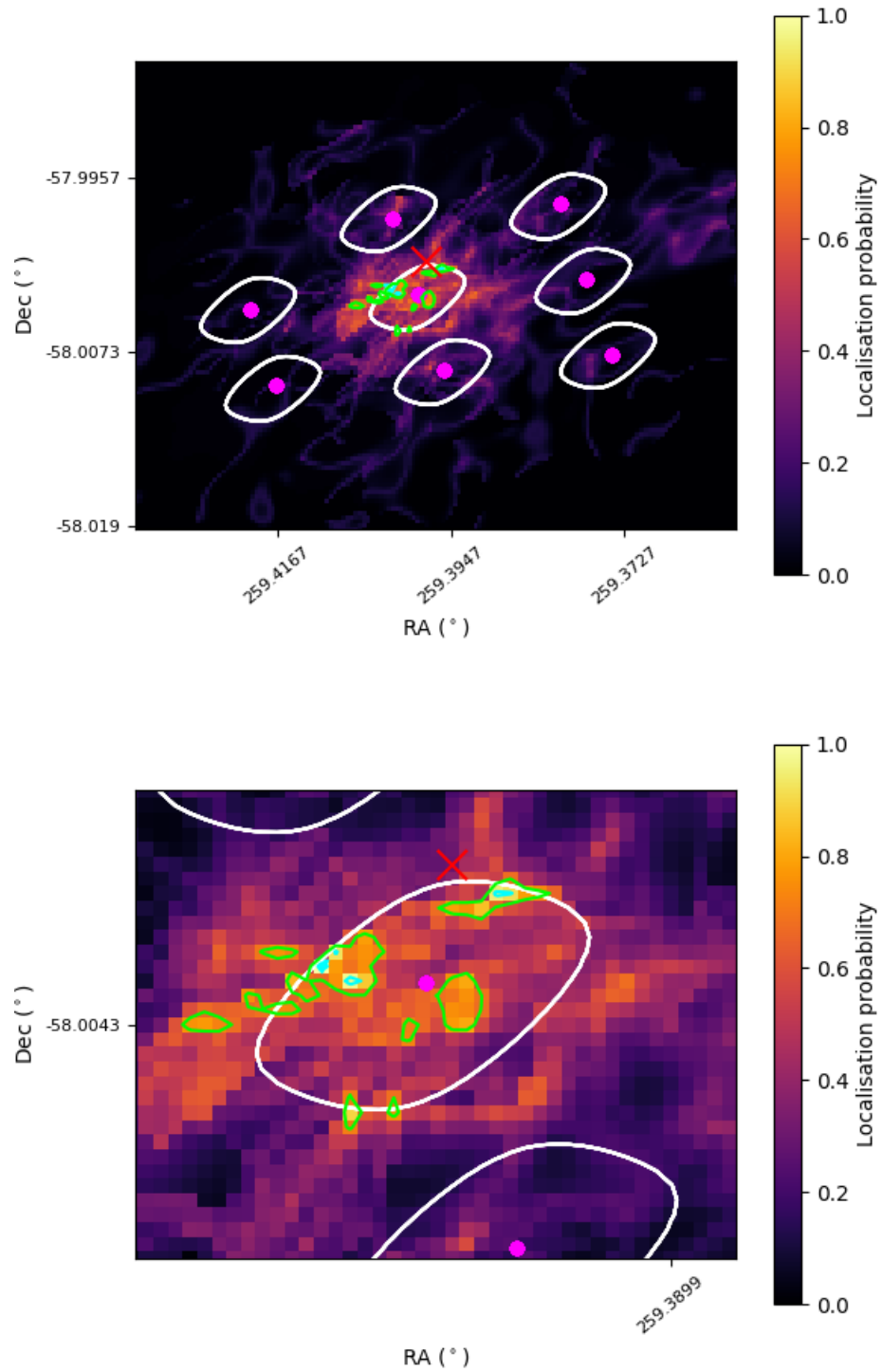


FIGURE 4.8: Localisation map for J1717.5–5804. The colour map depicts the localisation probability, with the pink dot marking the centre of each beam while the white contour is the beam shape at the half power point. Green and cyan contour represent 68 and 90 percent probability, respectively. The red cross is the location of J1717.5–5804 in the catalogue. We notice that the localisation is different from the known location. This probably due to the noise and RFI in some of the beams that weigh the localisation position.

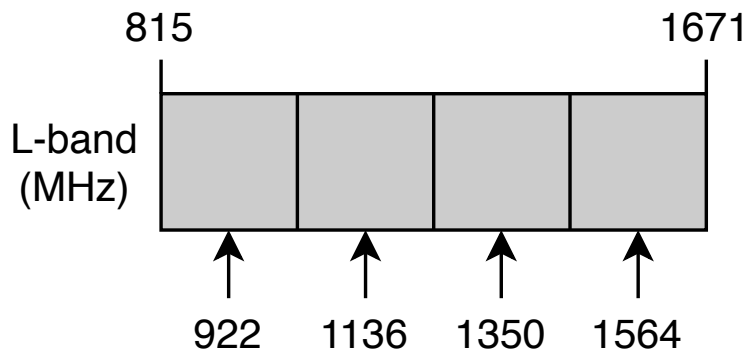


FIGURE 4.9: The image shows 4 new chunks after splitting with 4 new centres of frequency that we use for localisation. Those frequencies are 922, 1136, 1350, and 1564 MHz

Thus, we split the data into 4 frequency chunks for which we will perform the localisation individually. We use the PSRCHIVE command *psrsplit* to separate the data. A schematic diagram showing the centre of each new chunk can be found in Figure 4.9. By splitting the data into smaller frequency intervals, the results from localisation have changed and should be more reliable. This is since the pulsar spectrum affects its effective weight across the receiver bandwidth, and that the beam size is frequency-dependent. The detection, especially in side lobes, can be different in distinct frequencies. Hence, splitting pulsar data should give us more insights as to how reliable the localisation is if performed for the entire band. The results for the 4 subbands can be found in Figures 4.10 and 4.11. From these plots, we conclude that the localisation provides some approximate location for the true location of the source, but that the confidence contours are overestimating the true confidence. For the other candidates, we will stick to using the full band for the localisation, knowing that the position is likely in the vicinity but probably outside the 90% region. In the end, the localisation will be used for the confirmation observations to set a tighter packing for the beams and point the tile centre nearer to our best estimate for the position of the candidate. This will maximise our chances of confirming the pulsar and will further improve our localisation in the event that the candidate is a real pulsar, which in turn will speed up the process of obtaining a timing solution.

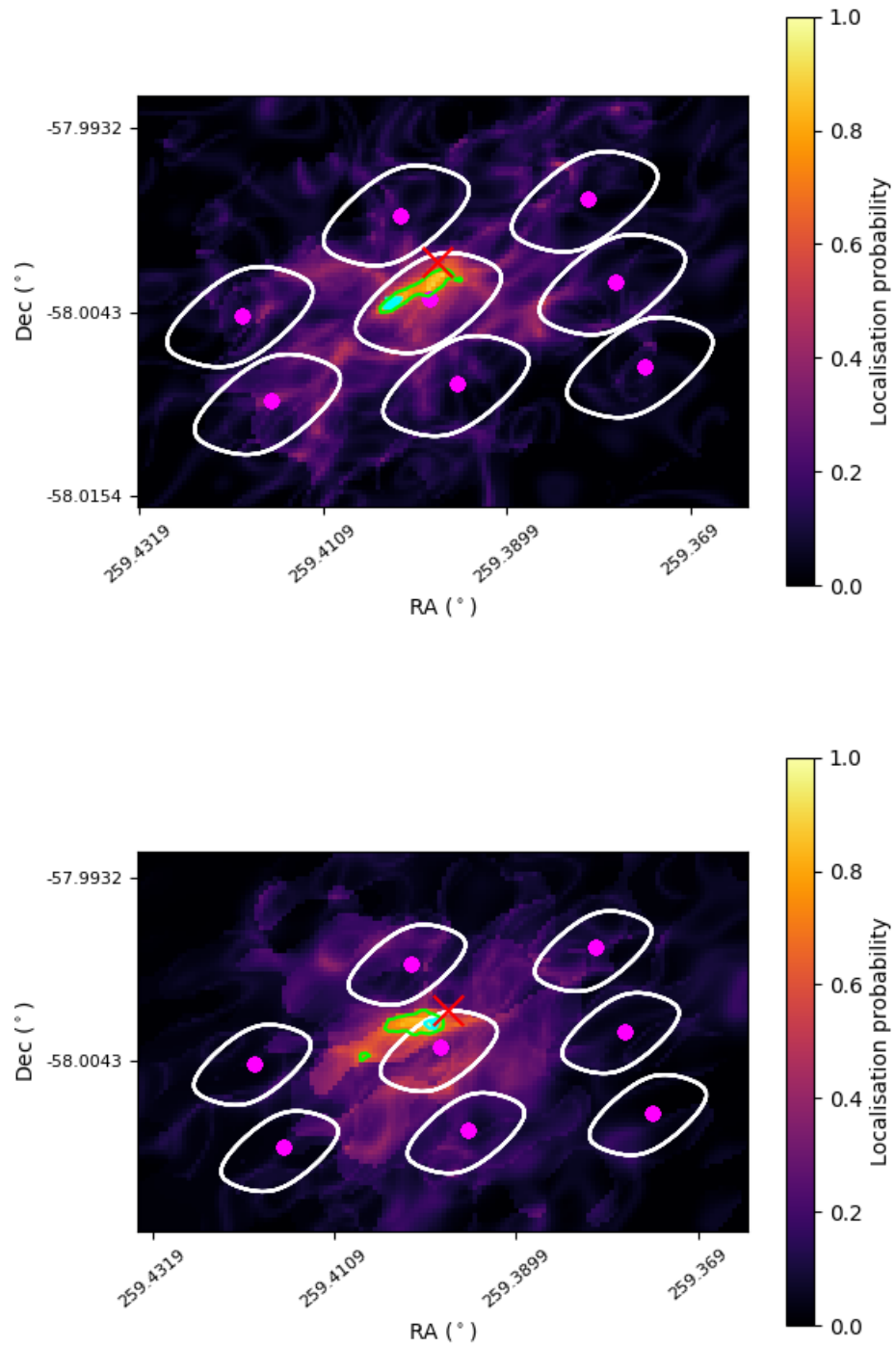


FIGURE 4.10: Localisation of split J1717.5–5804 data, The top image is a result of centre frequency at 922 MHz. The bottom image is a result of centre frequency at 1136 MHz.

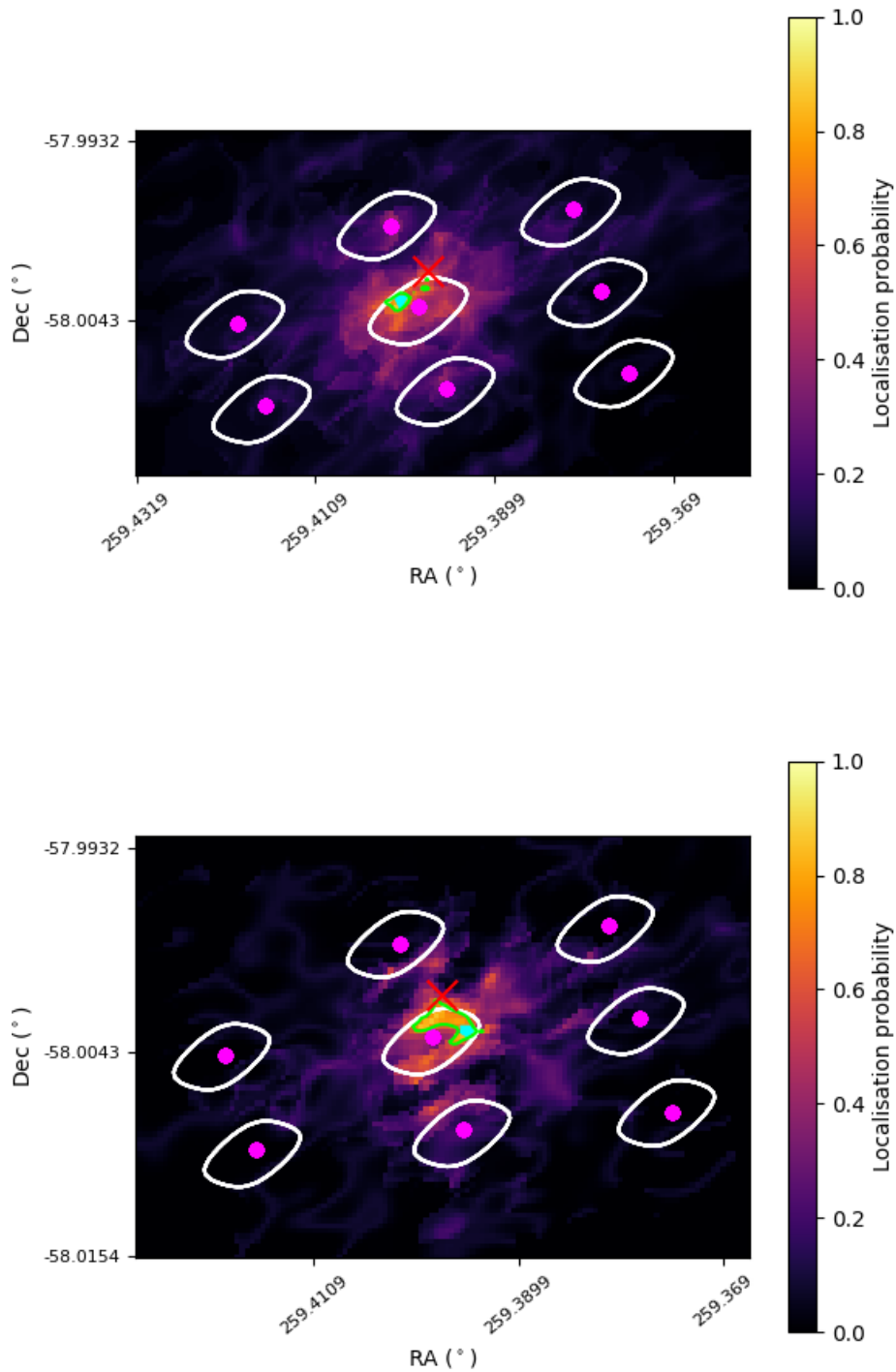


FIGURE 4.11: Localisation of split J1717.5–5804 data, The top image is a result of centre frequency at 1350 MHz. The bottom image is a result of centre frequency at 1564 MHz.

4.4 J1526.6–2743

J1526.6–2743 has been detected in the first batch of the observation on 2020-06-20 at 17:37:49. This source has an optimised DM at 31.00 ± 0.04 pc/cm³, a period of 2.489 ms, and an acceleration of -8.58 ± 0.75 m/s² (Figure 4.12). To do the localisation, The beam position and signal-to-noise information is provided in Table 4.4.

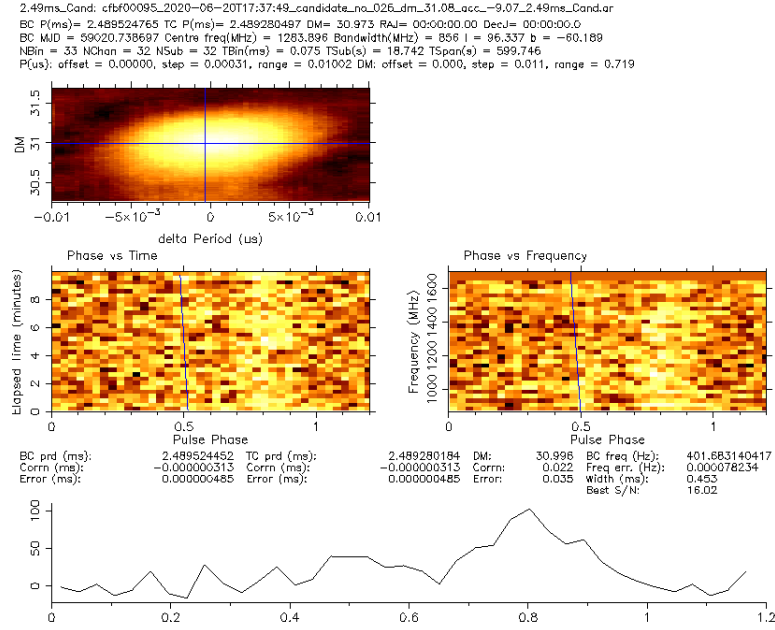


FIGURE 4.12: Original fold detection of J1526.6–2743. The pulsed signal is fairly weak, yet clearly identifiable through both time and frequency in the folds as a function of spin phase.

Beam	RA	DEC	S/N
cfbf00095*	15:26:45.89	-27:44:05.7	12.41
cfbf00047	15:26:43.45	-27:44:01.7	-
cfbf00049	15:26:44.16	-27:43:42.5	-
cfbf00051	15:26:44.87	-27:43:23.3	-
cfbf00094	15:26:45.17	-27:44:24.9	-
cfbf00097	15:26:46.60	-27:43:46.5	-
cfbf00139	15:26:47.61	-27:44:28.8	-
cfbf00140	15:26:46.90	-27:44:48.0	-
cfbf00141	15:26:48.32	-27:44:09.7	-

TABLE 4.4: The detection of J1526.6–2743 and neighbouring beams using for localisation. For this source, the localisation has not been done due to a low number of detections (the program can not be run because there is no other detection to compare).

4.5 J1803.1–6708

J1803.1–6708 has been detected in the first batch of the observation on 2020-06-20 at 19:35:10. This source has an optimised DM at 38.36 ± 0.04 pc/cm³, a period of 2.134 ms, and an acceleration of 3.20 ± 0.38 m/s² (Figure 4.13). To do the localisation, The beam position and signal-to-noise information is provided in Table 4.5.

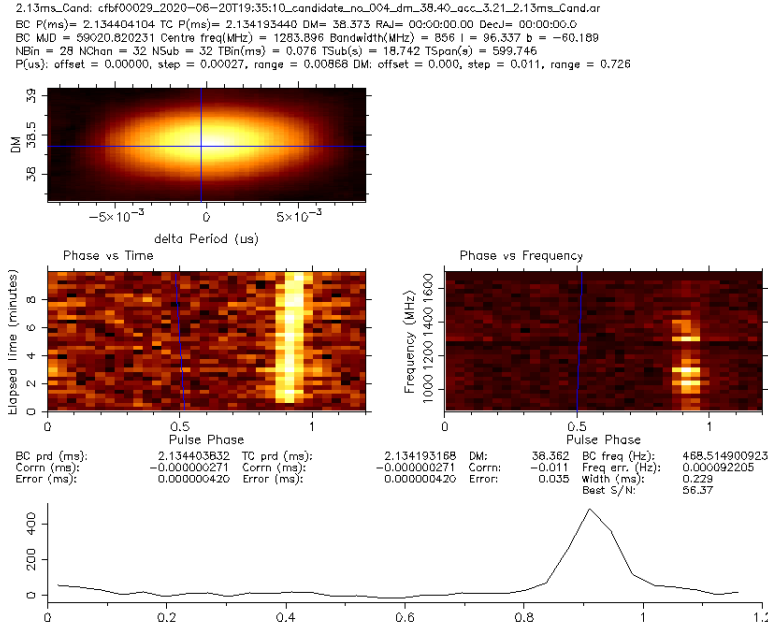


FIGURE 4.13: Original fold detection of J1803.1–6708. The pulsed signal is strong. The pulse can be identified through both time and frequency in the folds as a function of spin phase. Furthermore, pulsar signal drops significantly at 1400 MHz in the frequency plot.

Beam	RA	DEC	S/N
cfbf00029*	18:03:04.00	-67:07:40.9	56.37
cfbf00000	18:03:09.84	-67:08:04.9	16.01
cfbf00001	18:03:11.08	-67:07:46.7	15.04
cfbf00002	18:03:08.60	-67:08:23.1	-
cfbf00030	18:03:02.76	-67:07:59.0	10.11
cfbf00031	18:03:05.23	-67:07:22.7	17.33
cfbf00085	18:02:56.92	-67:07:35.0	-
cfbf00086	18:02:58.15	-67:07:16.8	14.09
cfbf00088	18:02:59.39	-67:06:58.7	9.11

TABLE 4.5: The detection of J1803.1–6708 and neighbouring beams using for localisation.

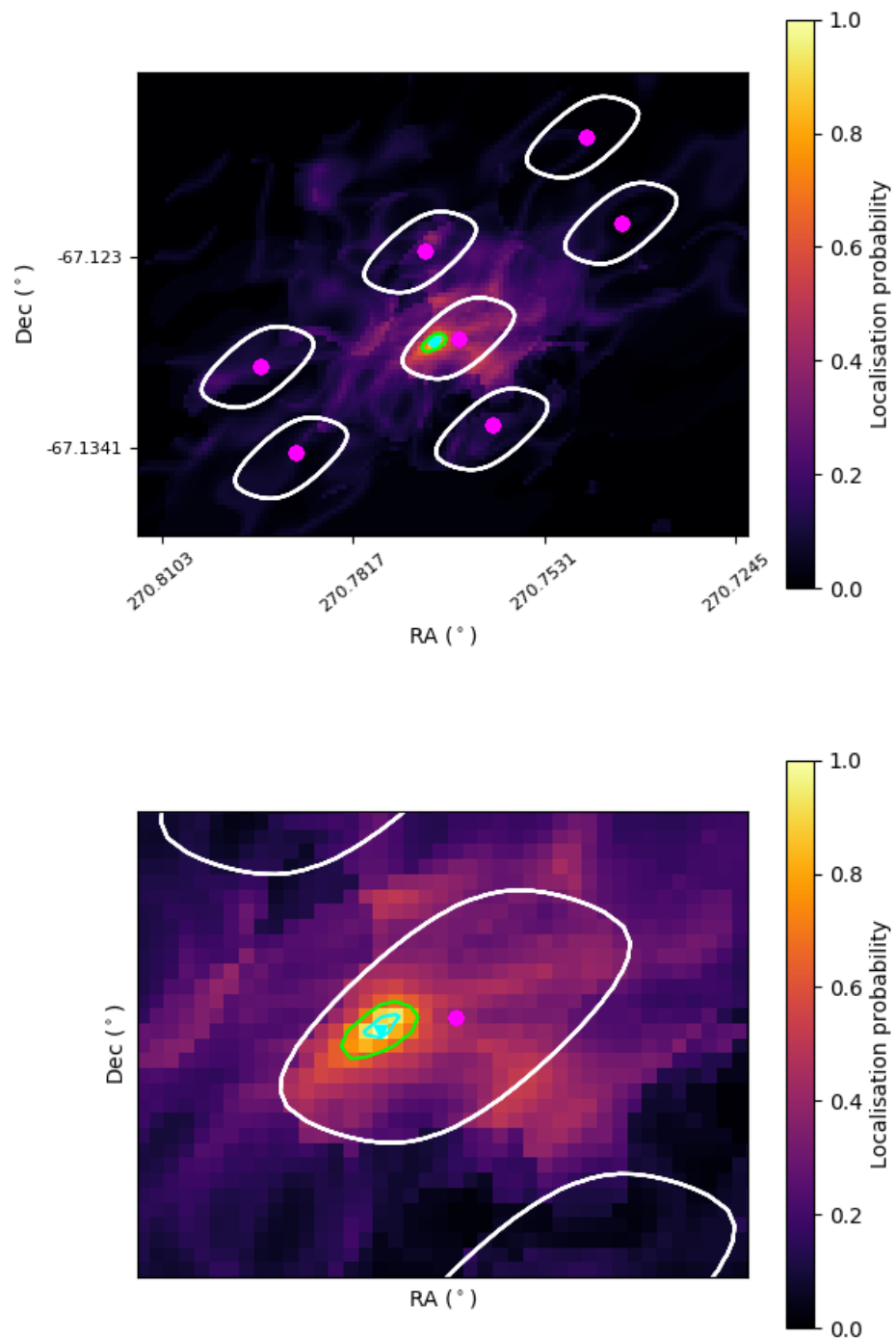


FIGURE 4.14: Localisation map for J1803.1–6708. The colour map depicts the localisation probability, with the pink dot marking the centre of each beam while the white contour is the beam shape at the half power point. Green and cyan contour represent 68 and 90 percent probability, respectively.

4.6 J1823.8–3544

J1823.8–3544 has been detected in the second batch of the observation on 2020-04-07 at 02:22:42. This source has an optimised DM at 1.65 ± 0.04 pc/cm³, a period of 2.373 ms, and an acceleration of 0.47 ± 0.56 m/s² (Figure 4.15). To do the localisation, The beam position and signal-to-noise information is provided in Table 4.6.

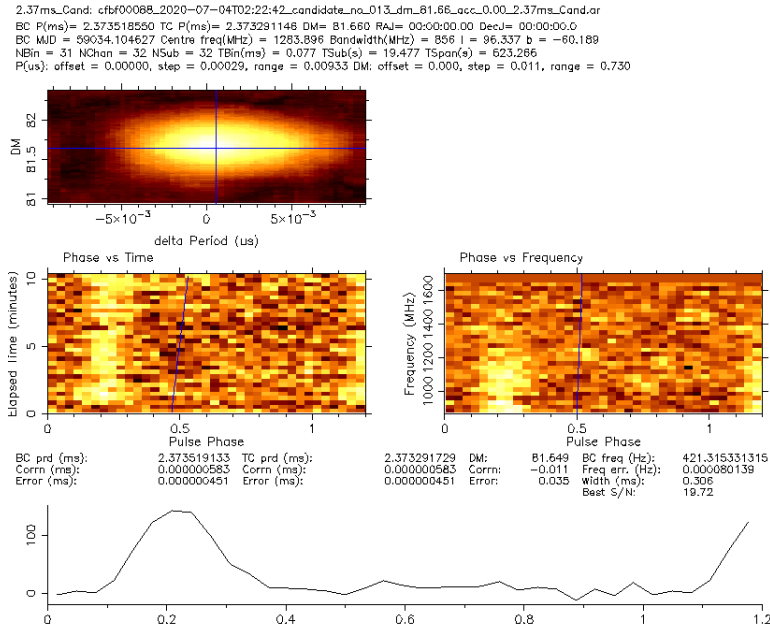


FIGURE 4.15: Original fold detection of J1823.8–3544. The pulsed signal is strong. The pulse can be identified through both time and frequency in the folds as a function of spin phase. Furthermore, pulsar signal drops significantly at 1400 MHz in the frequency plot.

Beam	RA	DEC	S/N
cfbf00088*	18:23:43.04	-35:43:26.5	16.8
cfbf00022	18:23:44.01	-35:44:19.3	-
cfbf00053	18:23:45.08	-35:43:48.7	13.26
cfbf00055	18:23:41.98	-35:43:57.1	13.63
cfbf00086	18:23:46.14	-35:43:18.1	-
cfbf00090	18:23:39.94	-35:43:34.9	8.89
cfbf00119	18:23:44.11	-35:42:55.9	-
cfbf00121	18:23:41.01	-35:43:04.3	-
cfbf00150	18:23:42.08	-35:42:33.7	-

TABLE 4.6: The detection of J1823.8–3544 and neighbouring beams using for localisation.

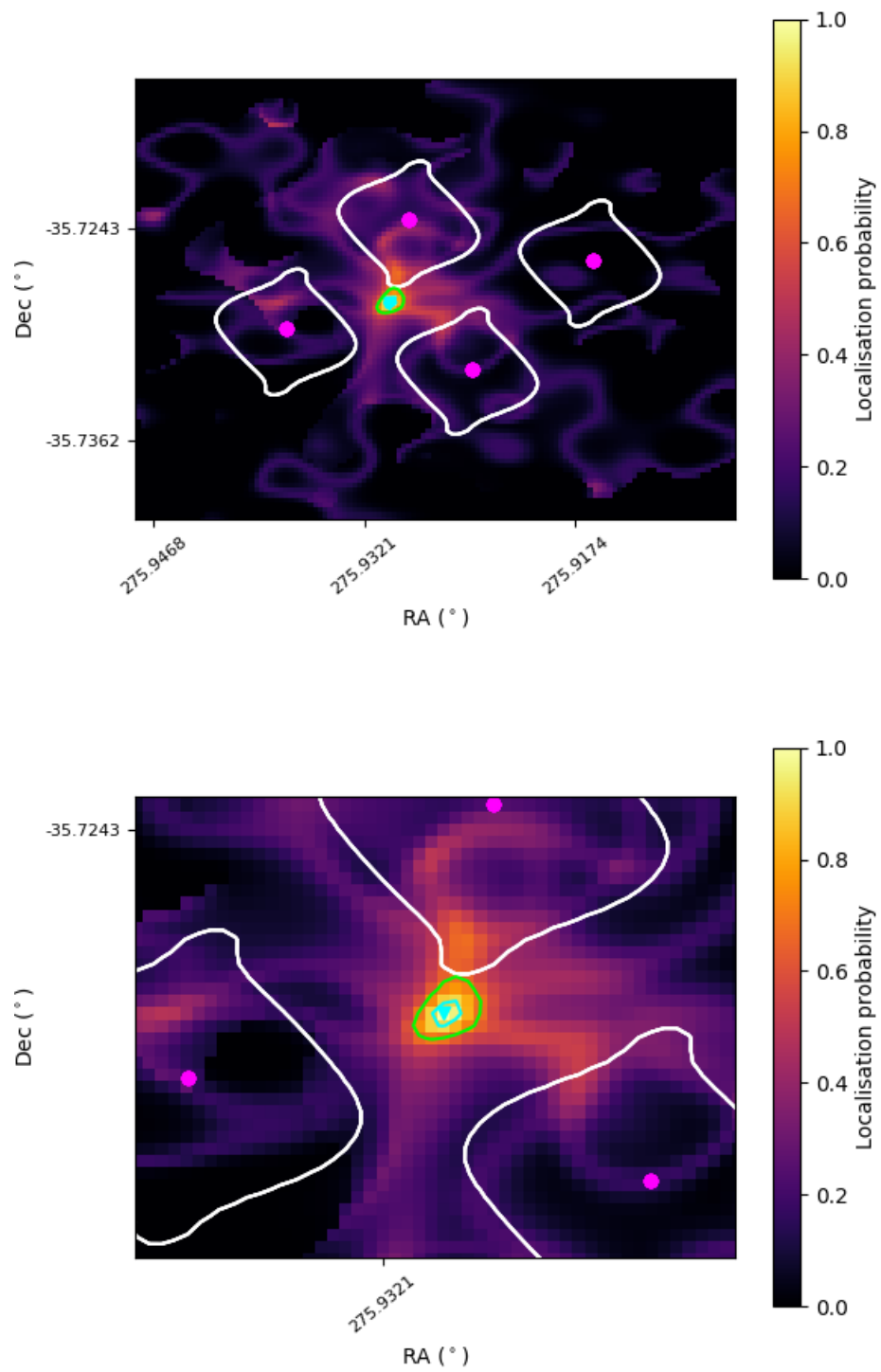


FIGURE 4.16: Localisation map for J1823.8–3544. The colour map depicts the localisation probability, with the pink dot marking the centre of each beam while the white contour is the beam shape at the half power point. Green and cyan contour represent 68 and 90 percent probability, respectively.

4.7 J1858.3–5424

J1858.3–5424 has been detected in the second batch of the observation on 2020-07-04 at 03:15:56. This source has an optimised DM at $30.80 \pm 0.04 \text{ pc/cm}^3$, a period of 2.355 ms, and an acceleration of $0.00 \pm 1.16 \text{ m/s}^2$ (Figure 4.17). To do the localisation, The beam position and signal-to-noise information is provided in Table 4.7.

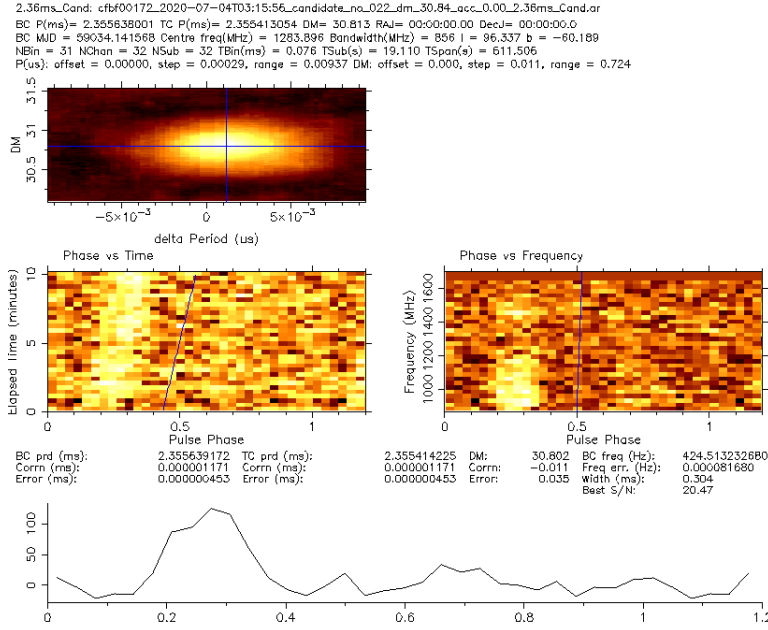


FIGURE 4.17: Original fold detection of J1858.3–5424. The pulsed signal is strong. The pulse can be identified through both time and frequency in the folds as a function of spin phase.

Beam	RA	DEC	S/N
cfbf00172*	18:58:09.67	-54:22:13.9	15.50
cfbf00122	18:58:11.39	-54:22:59.0	-
cfbf00145	18:58:13.09	-54:22:29.0	-
cfbf00147	18:58:07.96	-54:22:43.9	-
cfbf00171	18:58:14.80	-54:21:59.0	-
cfbf00174	18:58:04.54	-54:22:28.8	9.46
cfbf00195	18:58:11.38	-54:21:43.9	-
cfbf00197	18:58:06.25	-54:21:58.8	9.69
cfbf00218	18:58:07.96	-54:21:28.8	-

TABLE 4.7: The detection signal-to-noise of J1858.3–5424 and its neighbouring beams used for localisation.

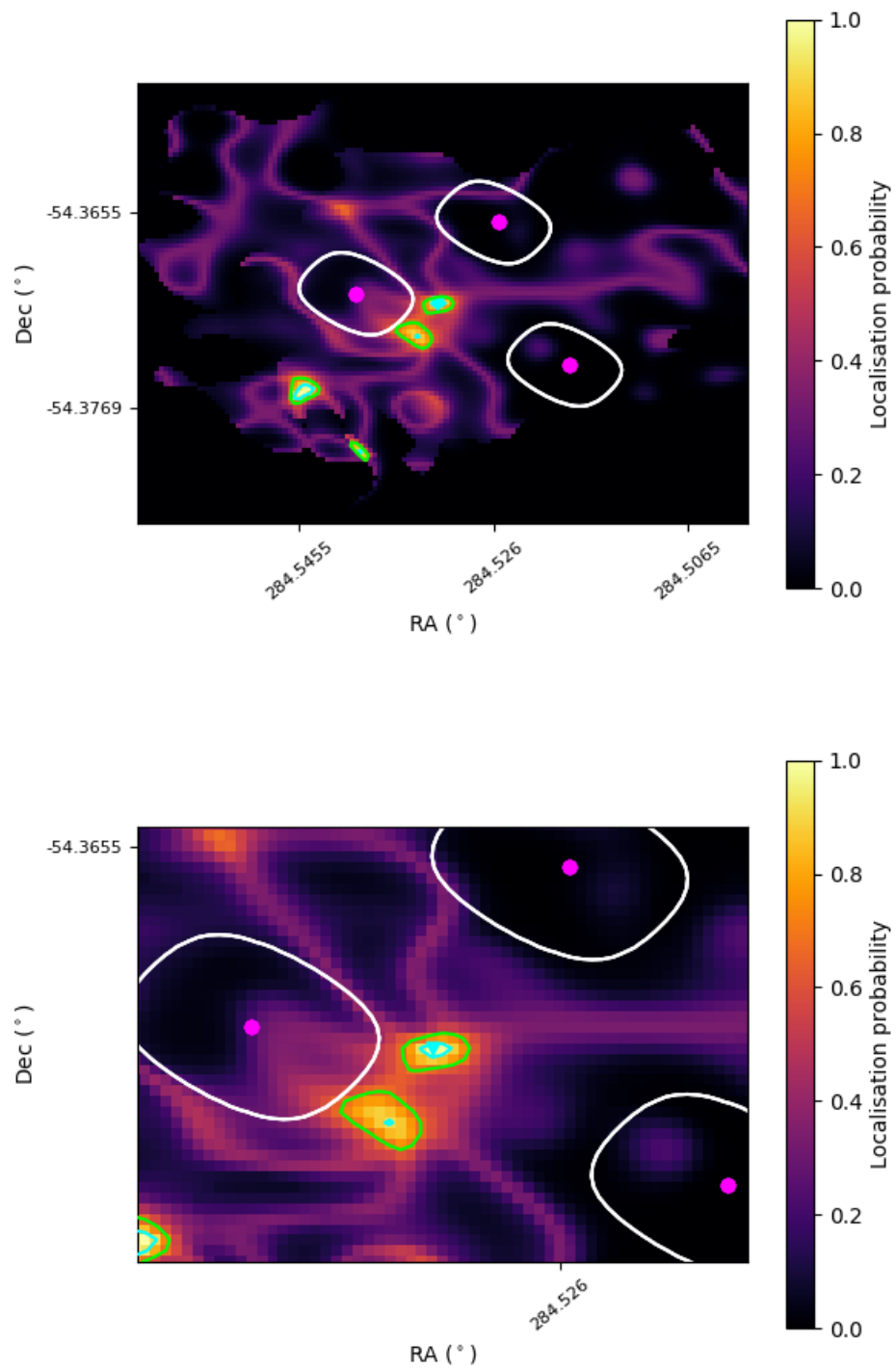


FIGURE 4.18: Localisation map for J1858.3–5424. The colour map depicts the localisation probability, with the pink dot marking the centre of each beam while the white contour is the beam shape at the half power point. Green and cyan contour represent 68 and 90 percent probability, respectively.

4.8 J1906.4–1757

J1906.4–1757 has been detected in the fourth batch of the observation on 2020-10-01 at 19:06:30. This source has an optimised DM at 98.06 ± 0.04 pc/cm³, a period of 2.877 ms, and an acceleration of 0.00 ± 0.89 m/s² (Figure 4.19). The beam position and signal-to-noise information used to do the localisation are provided in Table 4.8.

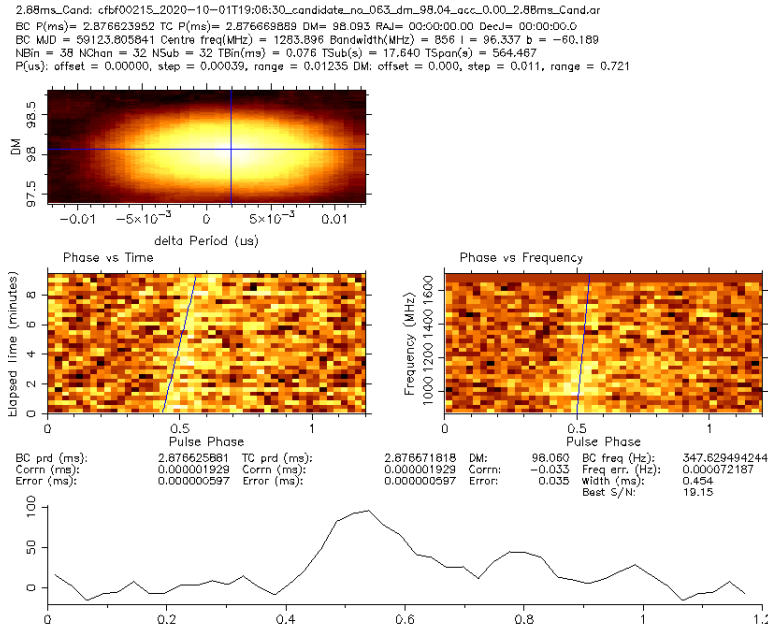


FIGURE 4.19: Original fold detection of J1906.4–1757. The pulsed signal is fairly weak, yet clearly identifiable through both time and frequency in the folds as a function of spin phase.

Beam	RA	DEC	S/N
cfbf00215*	19:06:15.51	-17:54:31.6	9.85
cfbf00182	19:06:17.35	-17:54:56.9	-
cfbf00184	19:06:15.38	-17:54:42.8	9.51
cfbf00213	19:06:17.48	-17:54:20.4	-
cfbf00217	19:06:13.54	-17:54:42.8	-
cfbf00244	19:06:15.63	-17:53:55.2	-
cfbf00246	19:06:13.67	-17:54:06.3	-

TABLE 4.8: The detection signal-to-noise of J1906.4–1757 and its neighbouring beams used for localisation. The detection is at the boundary of the tiling thus, there are only 7 surrounded beams instead of 8. For this source, the localisation has not been done due to a low number of detections (a low number of detections generates a poor result).

Chapter 5

Discussion and conclusion

In this last chapter, we discuss the results from the first pass of our shallow survey of Fermi unidentified sources and compare their expectations. We also consider the outlook from the second pass of the survey at L band and prospects of other strategies that could be adopted for further work. We also report on on-going follow-up work and summarises the work that has been carried out.

5.1 Discussion

In the first pass of our shallow survey of Fermi unidentified sources, we have found 5 new pulsar candidates and 1 known pulsar out of the 79 targets observed. These were selected out of the 13,115 candidates that were produced by our classification pipeline. These 5 candidates are likely to be a pulsar due to a very clear signal in both time series and frequency band. Furthermore, the noticeably short period of these sources suggests that they all are millisecond pulsars rather than young pulsars. However, follow-up observations are needed to confirm this assumption and confirm the existence of these pulsars.

We can estimate the expected number of pulsars using the probability value returned by the classifier presented in chapter 3.1, which provides the likelihood that a gamma-ray source gets classified as a pulsar. This will help us assess whether the result of five new pulsar candidates is in line with expectations. This will help us plan the upcoming observations. If the resulting number is close to the expected number of pulsars, the relevance of the second pass of the survey will be reduced.

For our estimation, we represent the probability that a 4FGL source is a pulsar using a binomial probability function where the probability of success (i.e. pulsar) is given by the probability ascribed by the classifier. We then simulate realisations of our 79 targets by drawing a sample from the corresponding binomial probability distribution for each target and calculate how many of them are pulsars. To properly sample the resulting probability distribution, we generate 10,000 Monte Carlo realisation of this process. Results from our simulation are plotted in Figure 5.1.

According to our calculations, the number of sources from our survey that are expected to be associated with a pulsar is 38 ± 4 out of 79. Note that by the central limit theorem, we can also analytically recover these numbers by considering the average probability and standard deviation of the 79 individual binomial distributions. This also explains why the shape of the histogram in Figure 5.1 resemble a Gaussian. Therefore, it is likely that there are many more pulsars to be discovered among the sources we pointed at in the first pass of our survey, which means that the second pass is important.

Several factors explain that only 5 new pulsars (candidates) have been discovered for the first pass of our survey. First, we assume that the random forest classifier provides the true probability that a source is a pulsar, which probability represents the likelihood that a source is classified as a pulsar not a true value. In reality, the two might not be the same. Second, the reported number assumes that all sources which are actual pulsars would be detectable as radio pulsars. However, it has already been established that pulsars show broader beams in the gamma-rays than in the radio regime (Ravi et al., 2010; Pierbattista et al., 2012). The true number that could be detected in our survey would be smaller by a factor similar to the ratio of the beaming fraction in the radio compared to that in the gamma-rays, which might be of order 0.5. Note that the exact beaming fraction is still not clearly established and depends on \dot{E} and the assumed model. Thus, there might very well be gamma-ray bright but radio-quiet pulsars in our sample of targets.

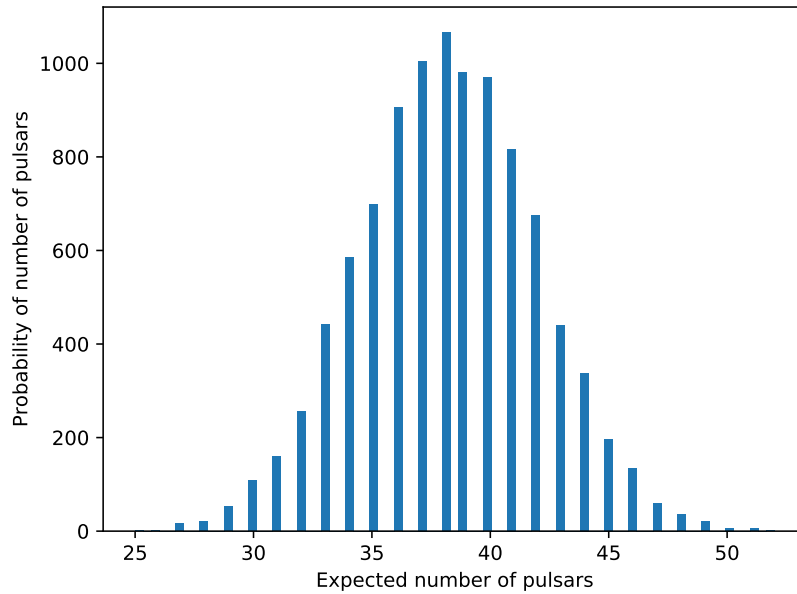


FIGURE 5.1: Histograms of expected new pulsars contained in our 79 targets from the 4FGL catalogue. The probability that a given target is a pulsar is given by a binomial distribution with a probability given by the probability returned from the random classifier presented in chapter 3.1. We generated 10,000 Monte Carlo realisation of the 79 targets and calculated how many of them are pulsars in each realisation. The mean and standard deviation of this histogram are 38 ± 4 , respectively.

Another factor is connected to the fact that many of the gamma-ray selected pulsars are energetic millisecond pulsars in so-called ‘spider’ binaries. These are known to display radio eclipses that can last a significant fraction of the orbit (Polzin et al., 2020). This phenomenon could be so extreme in some cases that the pulsar would be impossible to detect in the radio regime (or at frequencies below which the eclipse medium is opaque). In other systems, eclipses imply that repeated observations will be required to catch the pulsar out of eclipse. A subset of these spiders called ‘redback’ have also been observed to experience evolutionary state transitions where the system can flip back and forth between a ‘pulsar state’ and a ‘low-mass X-ray binary (LMXB) state’ (Stappers et al., 2014; Papitto et al., 2013). In the LMXB state, an accretion disc appears and radio pulsations disappear. A number of the unidentified Fermi sources could be in such an LMXB state.

In addition to intrinsic factors, radio searching inherently suffers from several factors that make the detection of pulsars sub-optimal. Millisecond pulsars suffer more heavily from the smearing induced by interstellar dispersion. Since our survey is guided by gamma-ray bright sources, which tends to favour energetic millisecond pulsars, the survey are more biased against finding pulsars having larger dispersion measures. Binary systems, which our survey is also biased toward, also require more processing resources (via the acceleration search) and can more easily miss sources. As a result, sources can be miss when searching in radio due to biased high DM sources from gamma-ray. RFI, noise fluctuations, and interstellar scintillation are also such that a pulsar might also not

be found in a single observation. These various elements motivate our approach to perform our survey in multiple passes. From our flux sensitivity calculations presented in section 3.2.2, the spectrum of each pulsar influences its likelihood of detection in a given band and so conducting another phase of the survey with observations with the UHF receiver is desirable to alleviate the bias.

The factors from above imply that the expectation value of 38 pulsars is probably an optimistic upper limit compared to the true detectable number. A more realistic estimate accounting for the gamma-ray to radio beaming would therefore be around half of it, ~ 19 pulsars, while a further reduction is to be expected from the other factors but somewhat difficult to ascertain. Similarly, for the entire 4FGL-DR2 list of unidentified Fermi sources, our analysis shows that up to 214 sources could be pulsars. We would also expect this number to be closer to 107 in reality. It is worth noting that our survey has so far focused on the higher probability sources since our nominal expected pulsar rate is 48% compared to 14% for the full 4FGL-DR2 list.

We can compare our detection rate so far with that of previous surveys of Fermi unidentified gamma-ray sources conducted with Parkes, GBT, Arecibo and, Effelsberg. For Parkes, 10 new pulsars were discovered from 49 Fermi unidentified sources, 1 pulsar was re-detected in a further field, and 6 known pulsars could not be detected in another 6 additional fields. Thus, this illustrates that even if a pulsar is associated with the Fermi source, it is not necessarily that it would be detected. As a result, the detection rate is around $\sim 20\%$ of their stated list (Camilo et al., 2015). The GBT survey, on the other hand, discovered 3 new pulsars out of 25 targets, hence $\sim 12\%$ (Ransom et al., 2010). From 34 targets, 6 new pulsars were discovered by Arecibo, which is $\sim 18\%$ (Cromartie et al., 2016). In the case of Effelsberg, they observed 289 unidentified sources and reported only 1 new pulsar (Barsdell et al., 2012). In our study, we use MeerKAT to observe 79 Fermi unidentified sources and we can assume that 5 have been detected as new pulsars (pending confirmation). Note that we exclude the known pulsar as it is likely not associated with the Fermi source (mentioned in chapter 4.3). As a result, our current detection rate is approximately $\sim 6\%$. Although our rate is lower than previous surveys, we have only conducted the first pass so far and the homogeneity of the other surveys compared to ours is debatable. For instance, some surveys have conducted repeated observations of some fields and occasionally benefited from prior information obtained at other wavelengths. Another effect that will likely start manifesting itself is the fact that surveys like ours are likely increasingly looking at candidates of “poorer” quality the brighter and more likely pulsars have possibly already been detected. It will therefore be interesting to consider a proper full comparison once our survey is completed. Another noticeable aspect is that all of the discovered sources from these previous surveys were indeed energetic millisecond pulsars similar to five new pulsar candidates from our survey.

5.2 Second pass observation

In preparation for the second pass of our survey, we have identified some areas where our observing configuration and overall strategy could be improved. In this context, progress made by the MeerKAT team now enables larger data through the backend system. This implies that more coherent beams can be formed on the sky and/or changes made to the channelisation and time resolution of the data recorded. More flexibility with the observing setup is also now possible. We discuss some of the possible adjustments that could be made below in this section.

After the survey's first pass, 5 new pulsars have been discovered. For the second pass, adjustments should be made to the previous setting to improve our sensitivity. The first step is to re-check the available information. By using *tilsim.py*, we set the configuration with a full array (64 antennae) with 288 beams and vary the elevation to get the beam size. In addition, different beam tiling compactness has been examined, ranging from 0.5 to 0.7 in beam overlap in units of intensity at full power (i.e. 0.5 meaning that adjacent beams intersect at the point where the power drops to 50% of the peak value). The results are shown in Figure 5.2. The MeerKAT operations now support the dynamic change in tiling between observations. It will be possible to optimise the overlap fraction from one source to another, given the time of the observation (and thus elevation angle) to maximise sensitivity while also ensuring that the full region of interest (i.e. r_{95}) is covered. Furthermore, the new possibility of using 480 rather than 288 beams will also increase sky coverage by nearly 30% at a similar overlap factor. This optimisation implies that, in some cases, the detection sensitivity at the coherent beam intersection could increase by a factor ~ 2 or so. Another important factor is that in the initial tiling design, the approximate coherent beam that was used overestimated the beam size at an assumed 0.5 overlap (see the black curve in Figure 5.2). This implies that the actual overlap that was used for the survey's first pass was effectively lower than 0.5, which was assumed. We believe the reason for this is the non-Gaussian shape of the coherent beam produced by the interferometer, which has a central 'plateau' but then decreases fairly sharply.

According to Figure 5.3, 40 sources have maximum DM higher than 100 pc/cm^3 while other 39 sources have maximum DM lower than 100 pc/cm^3 . This histogram provides information about existing targets, which can be useful when designing de-dispersion plan and observation. Our main goal is that we want a more suitable setup in the second pass of observation. More beams and compact beams provide more sensitivity. However, it comes with a downside of the data rate. Thus, there is a need to adjust the de-dispersion plan. The first attempt for the second pass is a sampling time of $76 \mu\text{s}$, 2048 channels for 480 beams, and 0.7 overlap.

We have compared the old and new de-dispersion plans for the observation. The old setting was $dt = 76 \mu\text{s}$, $N_{chan} = 4096$ for 288 beams. The new setting is $dt = 76 \mu\text{s}$, $N_{chan} = 2048$ for 480 beams and 70 percent overlap. Essentially the same coverage as in the first pass is achieved with 288 beams at 50 percent overlap. The de-dispersion plan depicts that the new setting is better at low DM (lower than 100) while the old setting is superior

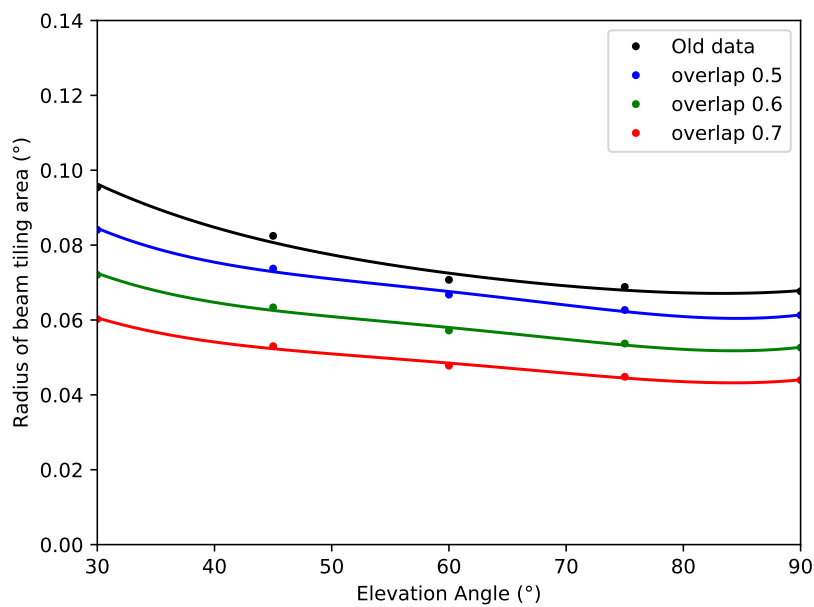


FIGURE 5.2: The plot shows the radius of the approximate circular area covered by 288 coherent beams as a function of elevation. The result has been generated by *tilsim.py*. The new configuration is a full array of 64 antennae, 288 beams, and 3 different values of overlap, 0.5, 0.6, and 0.7, which are represented in blue, green, and red, respectively. The black curve shows the estimated size for a 0.5 overlap, which was available to us using an approximation beam (Figure 3.7). This clearly overestimated the beam size, which means that for a given coverage area the beam overlap was in fact lower than the assumed 0.5 value.

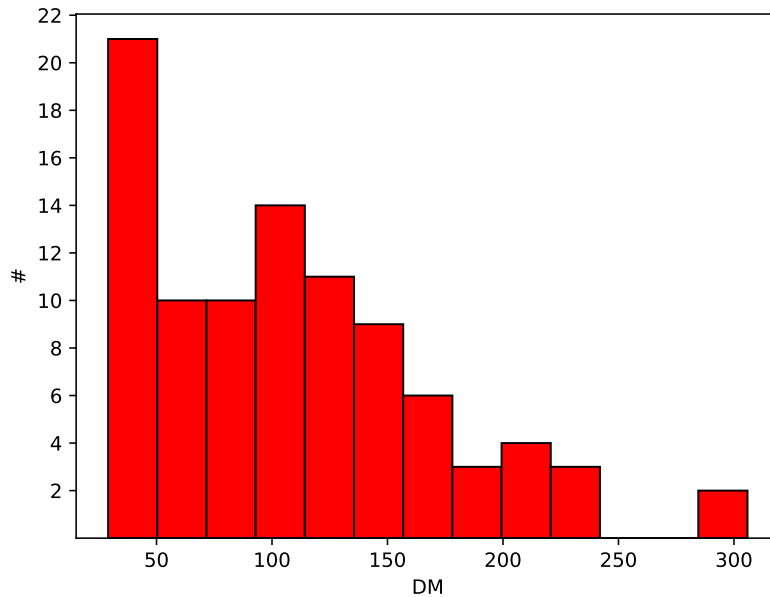


FIGURE 5.3: Histogram of maximum DM along the line of sight of 79 sources. 40 sources have maximum DM higher than 100 pc/cm^3 , other 39 sources have maximum DM lower than 100 pc/cm^3 (using NE2001 electron density model (Cordes & Lazio, 2002)).

at higher DM shown in Figure 5.4. However, we expect that all of our Fermi sources to be at lower DM, and even between DM 100 to 300 pc/cm^3 we can detect pulsars that have a period of 2 or 3 ms and above. Hence, dropping from 4k to 2K channels and higher time resolution is the better option. This suggests that approximately half of our sources benefit from the new de-dispersion plan setting while the other half prefers the old setting. The best solution is separating 79 sources into two groups.

5.3 Deeper survey and follow-up observations

Besides the second pass, we intended to extend our source list using the updates provided by the Fermi Large Area Telescope Fourth Source Catalogue Data Release 2 (4FGL-DR2). This catalogue is a gamma-ray catalogue from 50 MeV to 1 TeV, which uses the same analysis method as in the previous catalogue (4FGL), but incorporates the first ten years of data instead of the first eight years. Details about the 4FGL-DR2 can be found in Ballet et al. (2020). By using this catalogue with similar constraints as our original survey's source selection, our new list contains 100 rather than 79 sources. This will provide a $\sim 25\%$ increase in "high quality" targets for us to investigate. Once these targets have been observed, we will investigate as part of the TRAPUM collaboration whether we wish to extend the survey to targets that are considered to have a lower probability of being a pulsar. Alternatively, there are plans to revisit targets using longer observing times than the current 10 minutes to reach deeper flux density limits.

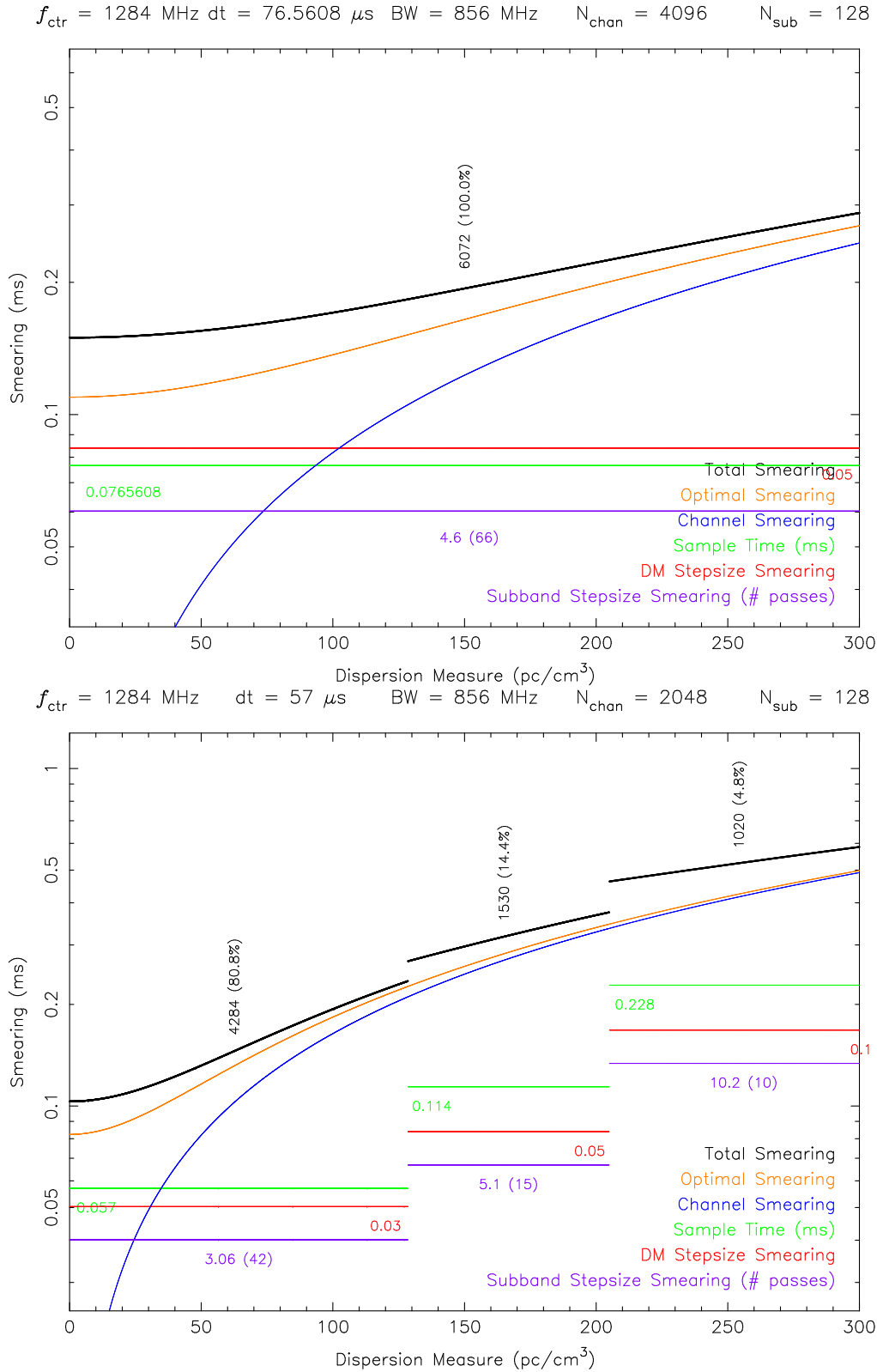


FIGURE 5.4: Comparing de-dispersion plans for both first and second passes, the top plot is the old setting for the first pass because we want a better time resolution, the second pass setting has been tested. As we can see the first setup is better at higher DM ($DM > 100 \text{ pc/cm}^3$). On the contrary, the second setup is recommended for lower DM ($DM < 100 \text{ pc/cm}^3$).

For the follow-up survey, the Fermi-TRAPUM Working Group has sent the potential candidates to the Follow-up Working Group that has a follow-up proposal for Parkes approved. One of the Follow-up Working Group members, Marta Burgay has used Prep-fold to re-fold J1803.1-6708, the brightest candidates, on a 1-hr long observation on the archive taken in 2015 with the Parkes DFB backend. DFB backend is a high-speed dual input sampler and a digital signal processing (DSP) card for pulsar processing. The examination of these data has confirmed that the candidate is a pulsar (Figure 5.5). In addition, there are some orbital details already available using archival observation and MeerKAT detection (period and acceleration). The MeerKAT observation covered a different part of the orbit. Therefore, the orbit parameter can be estimated. The results are the estimated orbital period (8.5 hr) and minimum companion mass ($0.26 M_{\odot}$, assuming a canonical $1.4 M_{\odot}$ pulsar). This particular pulsar is likely a redback system and was probably missed in the past due to the varying orbital acceleration. A new, updated proposal to follow-up the current five pulsar candidates using Parkes has now been submitted to continue the existing one, which is soon due to expire. The follow-up observation consists of 1-hr observation for J1803.1–6708 and 2-hr observation for other candidates. This proposal is requested to get an initial estimate of the spin and orbital parameters. The total time request for the second follow-up proposal is 62 hours and should enable us to obtain enough time-of-arrival measurements to establish early timing solutions for these objects.

5.4 Targeted survey

Another future area of work that we are already pursuing is to perform a targeted survey (observing specific sources). We will observe targets that are known to be binary systems and have a high likelihood of harbouring a pulsar. They were chosen because an optical counterpart in the vicinity of a Fermi unidentified source has been discovered and displays flux and colour variability similar to the light curve signature of redback pulsar binaries. In some cases, optical spectroscopy has confirmed the existence of an unseen second body with a mass compatible with that of a neutron star. We currently collated five such sources for the first phase of our targeted survey: 4FGL J0523.3–2527, 4FGL J0838.7–2827, 4FGL J0940.3–7610, 4FGL J0955.3–3949, and 4FGL J2333.1–5527 (see Halpern et al., 2017; Strader et al., 2019; Swihart et al., 2020, for full references). A summary of the properties of these sources presented in Table 5.1.

To plan the observation, we account for the criteria due to the sources that have been observed in optical wavelength. Optical observations are far more superior in terms of localisation than gamma-ray. Therefore, there is no need for the r_{95} constraint. However, a new criterion has been added, which is the orbital ephemeris. We want to observe the pulsar when it is in front of its companion around the superior conjunction (phase = 0.75). By doing this, we minimise the chances of observing the potential pulsar while it is eclipsed. Furthermore, we plotted Figure 5.6 to assist with the planning of the observations. For the observing duration, a continuous one hour has been decided to reach

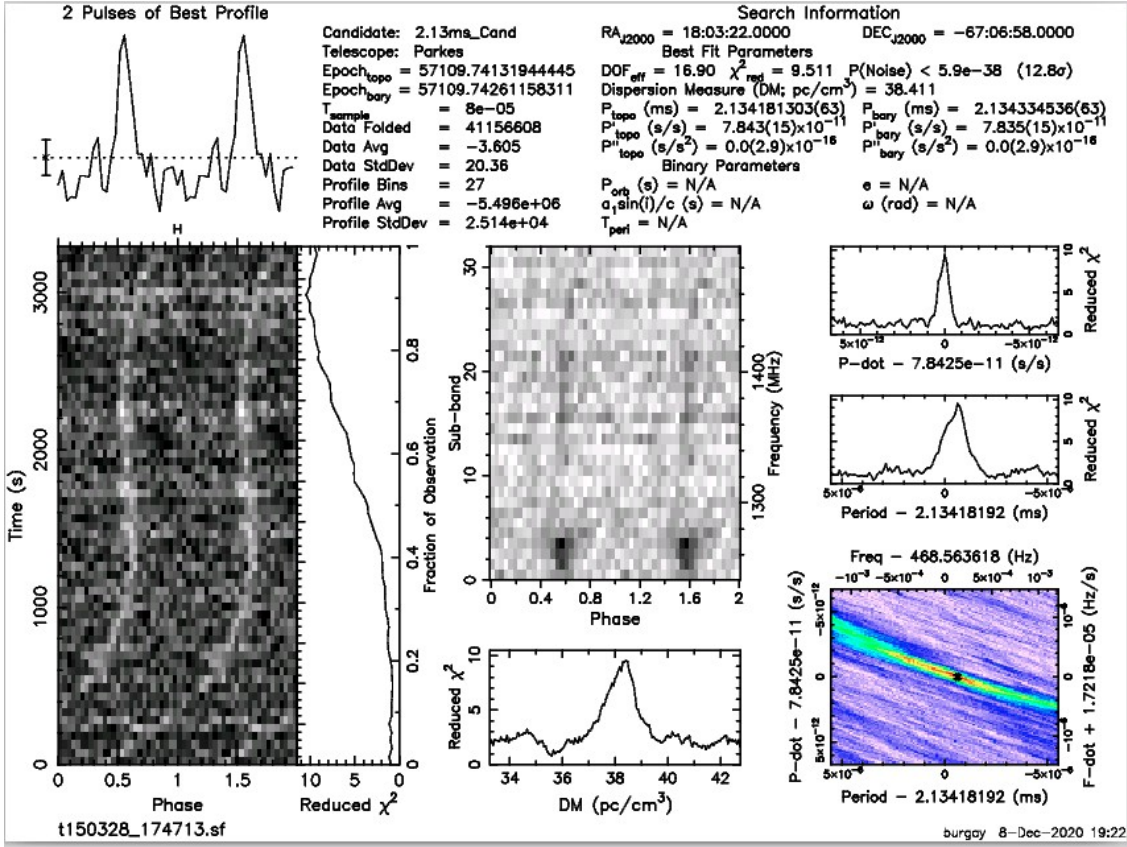


FIGURE 5.5: The Prepfold result of J1803.1-6708 from the archival data from Parkes in 2015. The result displays pulsar-like signal in both time series and frequency band (Figure provided by Marta Burgay).

a deep detection limit. The orbital periods of all sources lie between 5.1 and 16.5 hours, which implies that 1-hr observing time will represent between 5 and 20% of the orbit. We can therefore expect our strategy to be suitable for the (linear) acceleration search, which we will complement with a ‘jerk’ search in case no pulsar is detected with the simpler analysis.

5.5 Conclusion

Previous work has demonstrated the success of detecting several types of pulsars (very fast-spinning millisecond pulsars and young pulsars) at both radio and gamma-ray wavelengths using point sources detected by the Fermi Gamma-ray Telescope as a treasure map (Guillemot et al., 2012; O’Leary et al., 2015). Many radio surveys have been conducted using Fermi unidentified gamma-ray sources as primary targets (Ransom et al., 2010; Barr et al., 2012; Camilo et al., 2015; Cromartie et al., 2016). So far, 20 new sources have been confirmed as pulsars in these previous surveys. The newly-built MeerKAT telescope, which started its pulsar searching activities in 2020, provides a major step-change in terms of instantaneous sensitivity and localisation capabilities over its predecessors, especially in the Southern Hemisphere, due to its large collecting area and interferometric capabilities (Booth et al., 2009).

Name	RA	DEC	TASC	PB
J0523.3–2527	80.8205208	-25.4602555	56577.31839	0.688135 d
J0838.7–2827	129.7100752	-28.4658240	57781.2515	0.2145229 d
J0940.3–7610	145.0991125	-76.16670278	58525.37263	0.270639 d
J0955.3–3949	148.8658712	-39.7978600	58097.44433	0.3873396 d
J2333.1–5527	353.3165313	-55.4391955	58463.46881	0.2876450 d

TABLE 5.1: Properties of five candidate redbacks for our upcoming targeted survey. The name refers to the 4FGL name. RA is the Right Ascension and DEC is the Declination at epoch J2000. TASC is the time of ascending of the pulsar in Mean Julian Day (MJD). PB is an orbital period in days (information taken from Halpern et al. (2017); Strader et al. (2019); Swihart et al. (2020)).

In this thesis, we reported on our contribution to a pulsar survey run by the TRAPUM Fermi Working Group made using the MeerKAT telescope at L-band (1284 MHz). This survey targeted a selection from the 1336 unidentified sources from the Fermi-LAT 4FGL catalogue (Abdollahi et al., 2020). Those sources were selected by criteria, for example, the quality of the localisation ($r_{95} < 5$ arcmins, sky position (declination lower than 20°)), and the probability of being associated with a pulsar given the variability and spectral curvature of their gamma-ray emission. As a result, we observed 79 unidentified gamma-ray sources for 10 minutes each. The source list has been split into four observing blocks. The acceleration search pipeline (Peasoup) has been run on a MeerKAT computer cluster and optimised for the expected dispersion measures, spin periods, and binary accelerations that these pulsars might have. Machine learning classification from Zhu et al. (2014) has been used to sift the pulsar candidates produced by the pipeline. We have folded and cleaned the result using Prepfold and CLFD, respectively. Subsequently, the 13,115 candidates produced by this process required human inspection to decide on their final classification. We produced a viewing tool to coordinate and accomplish this task within the collaboration. This resulted in us finding one known pulsar and discovering five new pulsar candidates. A careful re-processing and localisation of the data from these candidates has been performed. To confirm these candidates, follow-up observations are now required.

In December 2020, the first block of the second pass of our survey has been conducted with improved instrumental setup parameters compared to the first pass. We hope to further increase the number of new pulsars with this second pass. Our analysis demonstrates that up ~ 38 pulsars could lie within the 79 targets of our survey. However, this number is most likely an optimistic upper limit as intrinsic and instrumental selection effects are such that a realistic number of pulsars to be discovered is probably around up to ~ 19 , by potentially somewhat lower. Lastly, we have already expanded our search to uncovered more pulsars associated with Fermi sources. The major next landmark will be a targeted survey to observe five sources that have optical counterparts. They are suspected to be redback pulsar binaries.

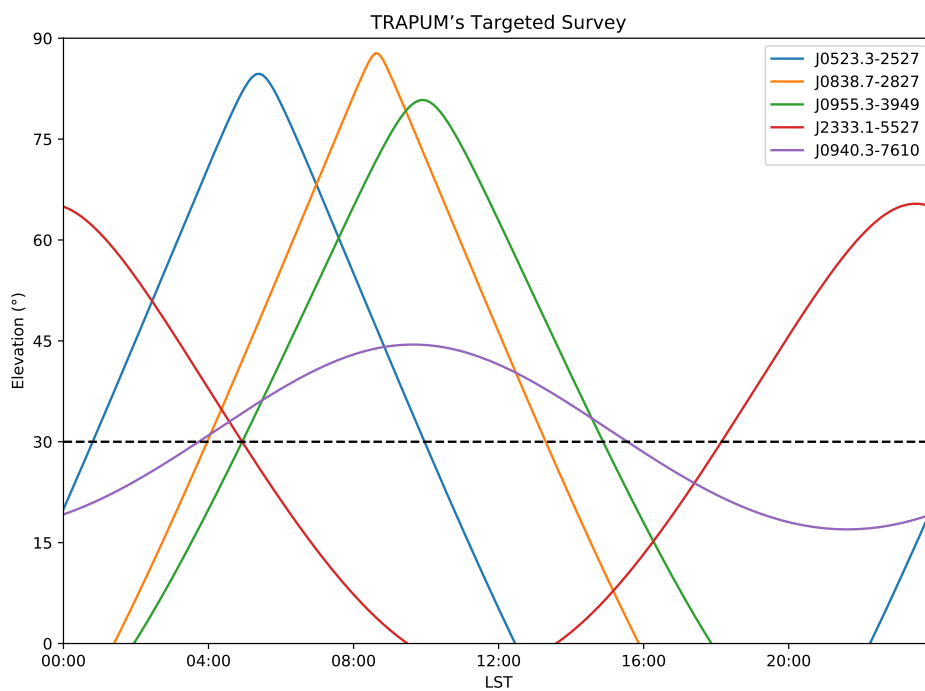


FIGURE 5.6: Elevation as a function of time for the 5 targeted redback candidates. This plot illustrates that all sources can be seen in a single 5-hour observing block at above $\sim 30^\circ$ elevation. However, in order to simplify the task of finding a suitable schedule where targets are observed at the right orbital phase range, we will split them into two groups.

Appendix A

The list of 79 sources

This appendix presents the list of selected 79 sources. Name of the target refers to the 4FGL name (Abdollahi et al., 2020). RA and DEC are in the epoch of J2000. The Galactic latitude is represented as b . r_{95} is the 95 %-confidence error region on the source localisation in arcminutes. P_{psr} is the probability of the source being a pulsar according to the machine learning classification detailed in Section 3.1. DM is the maximum dispersion measure from the NE2001 model (Cordes & Lazio, 2002). The PSC column refers to whether a source has been searched for in the radio according to the Pulsar Search Consortium (Ray, priv. comm).

TABLE A.1: A full list of 79 sources.

Name	RA	DEC	b	r95	p_{psr}	DM	PSC
J2112.5-3043	318.14001	-30.72930	-42.44355	1.068	0.96	46.8159	True
J1827.5+1141	276.87860	11.68630	10.55460	2.616	0.96	176.9606	True
J1231.6-5116	187.91020	-51.26720	11.48313	2.760	0.96	183.7301	True
J0940.3-7610	145.09891	-76.17940	-17.44946	2.664	0.94	110.2022	True
J0312.1-0921	48.02800	-9.35410	-52.37003	2.928	0.94	35.3578	True
J2212.4+0708	333.10831	7.14280	-38.47989	2.982	0.92	41.1455	True
J0802.1-5612	120.54560	-56.20120	-13.20960	3.120	0.91	286.4294	True
J1400.0-2415	210.02060	-24.26600	36.00356	3.078	0.91	50.6602	True
J1539.4-3323	234.85110	-33.39870	17.53206	1.374	0.90	123.2228	True
J0953.6-1509	148.40550	-15.15490	29.60278	2.094	0.89	55.3465	True
J2043.9-4802	310.98151	-48.03980	-38.28366	2.424	0.87	52.0685	True
J1730.4-0359	262.60861	-3.99230	15.99531	2.208	0.86	130.7822	True
J1845.8-2521	281.46481	-25.35850	-10.12024	3.336	0.85	223.757	True
J1612.1+1407	243.03130	14.11680	41.60764	3.264	0.84	35.919	True
J1757.7-6032	269.44891	-60.53740	-17.18688	2.226	0.84	129.6385	True
J1543.6-0244	235.90770	-2.74710	38.88678	3.372	0.83	41.6017	False
J1924.8-1035	291.20529	-10.59090	-12.16845	2.382	0.78	172.7905	True
J2133.1-6432	323.29510	-64.53830	-41.28885	2.640	0.77	47.4491	True
J1818.6+1316	274.65271	13.27310	13.19931	2.886	0.77	136.742	True
J1120.0-2204	170.00160	-22.07790	36.05591	1.380	0.75	50.1174	True
J1858.3-5424	284.57599	-54.41230	-22.72645	4.008	0.71	94.0932	True
J1207.4-4536	181.87340	-45.61250	16.57598	3.792	0.70	119.605	False
J1526.6-2743	231.67090	-27.73270	23.68056	3.720	0.68	83.8507	True
J1831.1-6503	277.77731	-65.06590	-22.34894	2.178	0.67	94.6409	True
J1717.5-5804	259.37839	-58.07060	-11.50470	2.748	0.66	205.4961	True
J1824.2-5427	276.07040	-54.45140	-18.04902	2.574	0.61	123.4598	True
J1659.0-0140	254.76550	-1.67750	23.92776	2.790	0.61	78.747	True
J1720.6+0708	260.16379	7.14690	23.41902	3.378	0.60	77.775	True
J1544.2-2554	236.05231	-25.91250	22.60352	2.478	0.59	88.7697	True
J1916.8-3025	289.22369	-30.42460	-18.42003	1.866	0.59	119.9363	False
J1106.7-1742	166.69901	-17.71480	38.47668	3.252	0.57	46.6422	True
J1630.1-1049	247.52890	-10.81830	24.83086	3.384	0.57	76.8948	True
J1416.7-5023	214.17810	-50.38950	10.21311	3.264	0.55	223.369	True
J0048.6-6347	12.16850	-63.79140	-53.33411	3.240	0.53	36.2674	True
J2219.7-6837	334.94690	-68.61730	-42.89050	2.430	0.52	45.2671	True
J1913.4-1526	288.35150	-15.44960	-11.74581	3.336	0.51	188.1756	True
J1204.5-5032	181.14830	-50.54560	11.63658	4.398	0.50	176.7995	True
J1816.4-6405	274.11499	-64.08500	-20.54843	3.354	0.47	104.6426	True

Continued on next page

Table A.1 – Continued from previous page

Name	RA	DEC	b	r95	P_{psr}	DM	PSC
J1747.6+0324	266.90509	3.40730	15.74170	2.766	0.46	124.7957	True
J1458.8-2120	224.70329	-21.33880	32.56670	2.742	0.46	55.5443	False
J1036.6-4349	159.15070	-43.82390	12.61511	3.150	0.45	142.0806	True
J0414.7-4300	63.69770	-43.01200	-46.22139	4.398	0.45	37.2805	False
J2201.0-6928	330.25699	-69.47390	-41.05111	3.126	0.41	47.1775	True
J1622.2-7202	245.55251	-72.03990	-15.51170	2.832	0.37	141.1156	False
J1711.9-1922	257.97760	-19.36760	11.65710	2.484	0.35	202.1237	True
J1345.9-2612	206.48151	-26.21160	35.07210	3.786	0.34	53.4701	True
J1906.0-1718	286.51859	-17.31530	-10.94926	4.626	0.33	207.4683	True
J2241.4-8327	340.35681	-83.46120	-32.58100	3.312	0.33	58.2557	False
J1735.3-0717	263.84009	-7.28530	13.28951	3.912	0.32	165.5668	True
J0529.9-0224	82.47700	-2.40480	-19.19776	4.572	0.30	74.3713	True
J1722.8-0418	260.71149	-4.30330	17.47949	2.472	0.29	118.6541	True
J0139.5-2228	24.89710	-22.47770	-78.13213	4.404	0.29	29.0429	True
J0657.4-4658	104.35980	-46.98020	-18.51060	3.960	0.26	81.4892	True
J1517.7-4446	229.42799	-44.77670	10.73275	4.854	0.24	219.062	True
J2355.5-6614	358.89081	-66.23450	-49.94003	3.738	0.24	38.8798	True
J1526.6-3810	231.65939	-38.16900	15.27866	4.716	0.23	143.4194	True
J2121.8-3412	320.47421	-34.20330	-44.87624	4.824	0.23	45.1072	True
J1213.9-4416	183.49440	-44.27950	18.07963	2.766	0.23	109.2276	True
J1803.1-6708	270.79099	-67.13470	-20.35580	2.070	0.23	105.0773	True
J1749.8-0303	267.46219	-3.05180	12.22140	3.072	0.22	176.3154	True
J1126.0-5007	171.51450	-50.11940	10.46262	4.008	0.21	189.8729	True
J1822.9-4718	275.73621	-47.30470	-15.08772	3.144	0.20	153.2065	True
J1816.7+1749	274.18771	17.82790	15.50645	3.162	0.20	109.2091	False
J2026.3+1431	306.59879	14.52250	-13.44417	3.318	0.19	112.9549	True
J0540.0-7552	85.00640	-75.87820	-30.58225	3.510	0.19	58.4571	True
J1513.7-1519	228.44450	-15.33310	35.27113	3.294	0.19	49.2503	True
J1656.4-0410	254.11940	-4.17020	23.18163	3.132	0.18	83.1652	False
J1947.6-1121	296.91611	-11.36520	-17.56450	3.348	0.18	111.0353	True
J1623.9-6936	245.98650	-69.60690	-13.96425	2.670	0.17	160.0867	False
J1646.7-2154	251.68510	-21.90750	14.90977	4.752	0.17	150.5449	True
J0712.0-6431	108.00800	-64.52560	-22.16661	4.638	0.17	76.7488	False
J1303.1-4714	195.78780	-47.23810	15.58671	4.740	0.15	134.7117	True
J1906.4-1757	286.61069	-17.95090	-11.29891	3.372	0.14	200.7841	False
J1450.8-1424	222.71080	-14.40590	39.35992	4.470	0.14	43.1815	True
J1709.4-0328	257.37469	-3.47100	20.77059	3.996	0.13	95.1976	True
J0251.1-1830	42.78350	-18.50930	-61.18706	2.058	0.13	31.9579	False
J1727.4+0326	261.86310	3.44980	20.22766	3.210	0.13	94.1391	False

Continued on next page

Table A.1 – *Continued from previous page*

Name	RA	DEC	b	r95	P_{psr}	DM	PSC
J1823.8-3544	275.96771	-35.74020	-10.35016	3.966	0.13	229.6853	True
J1813.7-6846	273.44809	-68.77850	-21.86269	4.050	0.12	96.2352	True

Appendix B

The details of four observing blocks

This appendix presents four observing blocks with the target's name, RA, DEC, and observing time when starting the observation. Moreover, the elevation of each source during the observation has been shown.

Name	RA	DEC	Time(UT)
J1543.6-0244	15:43:37.85	-2:44:49.6	16:55:17.190
J1623.9-6936	16:23:56.76	-69:36:24.8	17:06:13.216
J1646.7-2154	16:46:44.42	-21:54:27.0	17:16:54.925
J1513.7-1519	15:13:46.68	-15:19:59.2	17:27:26.792
J1526.6-2743	15:26:41.02	-27:43:57.7	17:37:53.273
J1539.4-3323	15:39:24.26	-33:23:55.3	17:48:10.309
J1544.2-2554	15:44:12.55	-25:54:45.0	17:58:28.382
J1400.0-2415	14:00:04.94	-24:15:57.6	18:09:01.330
J1416.7-5023	14:16:42.74	-50:23:22.2	18:20:18.241
J1612.1+1407	16:12:07.51	14:07:00.5	18:31:33.173
J1717.5-5804	17:17:30.81	-58:04:14.2	18:42:36.964
J1727.4+0326	17:27:27.14	3:26:59.3	18:53:33.340
J1720.6+0708	17:20:39.31	7:08:48.8	19:03:50.145
J1749.8-0303	17:49:50.93	-3:03:06.5	19:14:12.789
J1630.1-1049	16:30:06.94	-10:49:05.9	19:24:48.014
J1803.1-6708	18:03:09.84	-67:08:04.9	19:35:55.160
J1711.9-1922	17:11:54.62	-19:22:03.4	19:46:51.228
J1757.7-6032	17:57:47.74	-60:32:14.6	19:57:41.611
J1204.5-5032	12:04:35.59	-50:32:44.2	20:08:30.822

TABLE B.1: The first observing block has been observed on 2020-06-20. Time refers to the starting time.

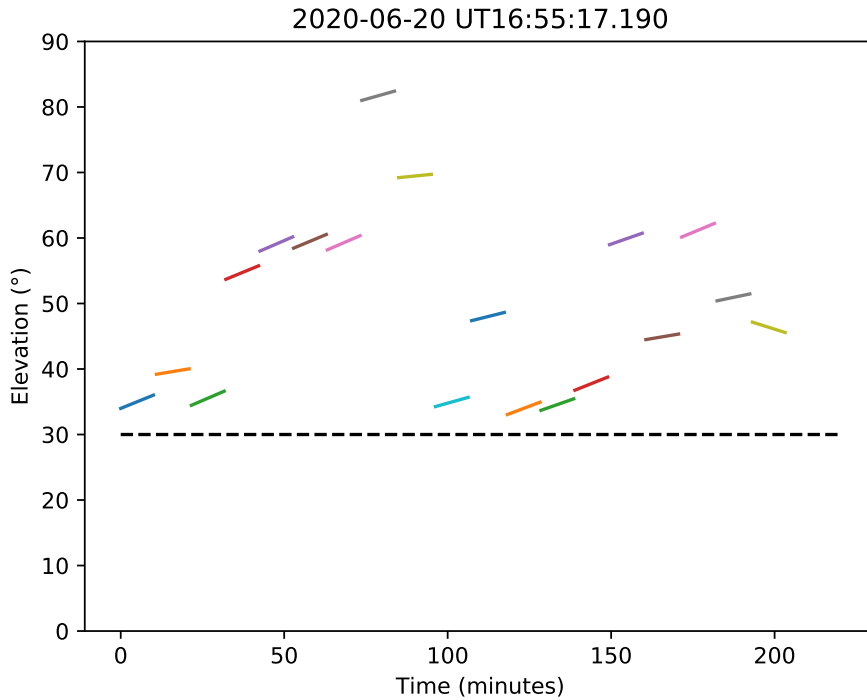


FIGURE B.1: The elevation of sources from the first observing block (0620). The dashed line is the minimum elevation at 30 degrees.

Name	RA	DEC	Time(UT)
J1924.8-1035	19:24:49.27	-10:35:27.2	02:01:54.452
J2026.3+1431	20:26:23.71	14:31:21.0	02:12:24.738
J1823.8-3544	18:23:52.25	-35:44:24.7	02:23:12.967
J1906.0-1718	19:06:04.46	-17:18:55.1	02:33:37.002
J2219.7-6837	22:19:47.26	-68:37:02.3	02:44:30.599
J2201.0-6928	22:01:01.68	-69:28:26.0	02:54:43.493
J1947.6-1121	19:47:39.87	-11:21:54.7	03:05:39.162
J1858.3-5424	18:58:18.24	-54:24:44.3	03:16:17.993
J0414.7-4300	4:14:47.45	-43:00:43.2	03:28:39.780
J2241.4-8327	22:41:25.63	-83:27:40.3	03:39:20.989
J2212.4+0708	22:12:25.99	7:08:34.1	03:51:24.228
J2355.5-6614	23:55:33.79	-66:14:04.2	04:02:41.978
J2043.9-4802	20:43:55.56	-48:02:23.3	04:13:15.981
J2112.5-3043	21:12:33.60	-30:43:45.5	04:23:40.413
J2133.1-6432	21:33:10.82	-64:32:17.9	04:34:15.725
J0312.1-0921	3:12:06.72	-9:21:14.8	04:46:13.942
J0251.1-1830	2:51:08.04	-18:30:33.5	04:56:34.902
J0048.6-6347	0:48:40.44	-63:47:29.0	05:07:48.021
J0540.0-7552	5:40:01.54	-75:52:41.5	05:18:18.830
J2121.8-3412	21:21:53.81	-34:12:11.9	05:29:11.209

TABLE B.2: The second observing block has been observed on 2020-07-04. Time refers to the starting time.

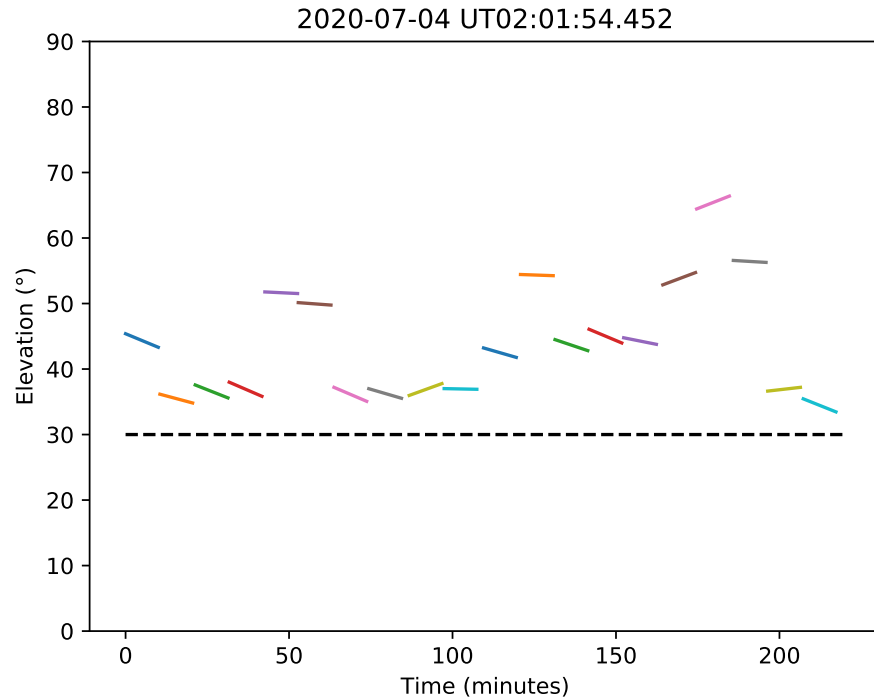


FIGURE B.2: The elevation of sources from the second observing block (0704). The dashed line is the minimum elevation at 30 degrees.

Name	RA	DEC	Time(UT)
J1303.1-4714	13:03:09.07	-47:14:17.2	10:05:18.460
J0529.9-0224	5:29:54.48	-2:24:17.3	10:17:08.018
J1126.0-5007	11:26:03.48	-50:07:09.8	10:29:00.628
J0802.1-5612	8:02:10.94	-56:12:04.3	10:39:41.587
J0953.6-1509	9:53:37.32	-15:09:17.6	10:51:14.264
J0657.4-4658	6:57:26.35	-46:58:48.7	11:02:44.699
J0940.3-7610	9:40:23.74	-76:10:45.8	11:13:20.715
J1345.9-2612	13:45:55.56	-26:12:41.8	11:25:51.777
J1207.4-4536	12:07:29.62	-45:36:45.0	11:36:24.085
J1036.6-4349	10:36:36.17	-43:49:26.0	11:46:48.949
J1106.7-1742	11:06:47.76	-17:42:53.3	11:57:59.380
J1120.0-2204	11:20:00.38	-22:04:40.4	12:08:21.032
J1213.9-4416	12:13:58.66	-44:16:46.2	12:19:12.626
J1517.7-4446	15:17:42.72	-44:46:36.1	12:29:55.822
J1231.6-5116	12:31:38.45	-51:16:01.9	12:40:31.999
J1526.6-3810	15:26:38.25	-38:10:08.4	12:51:10.385
J1450.8-1424	14:50:50.59	-14:24:21.2	13:01:37.459
J0712.0-6431	7:12:01.92	-64:31:32.2	13:12:51.773
J1458.8-2120	14:58:48.79	-21:20:19.7	13:24:02.224
J1622.2-7202	16:22:12.60	-72:02:23.6	13:34:48.092

TABLE B.3: The third observing block has been observed on 2020-08-04. Time refers to the starting time.

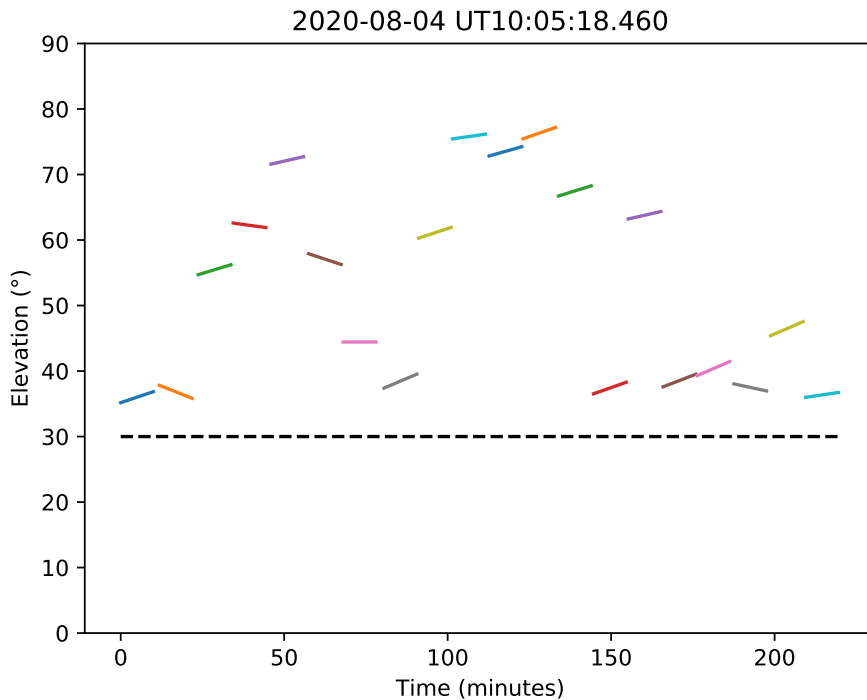


FIGURE B.3: The elevation of sources from the third observing block (0804). The dashed line is the minimum elevation at 30 degrees.

Name	RA	DEC	Time(UT)
J1656.4-0410	16:56:28.66	-4:10:12.7	16:05:21.255
J1824.2-5427	18:24:16.90	-54:27:05.0	16:16:40.742
J1813.7-6846	18:13:47.54	-68:46:42.6	16:27:06.858
J1816.4-6405	18:16:27.60	-64:05:06.0	16:37:22.256
J1816.7+1749	18:16:45.05	17:49:40.4	16:48:55.075
J1709.4-0328	17:09:29.93	-3:28:15.6	216:59:23.465
J1822.9-4718	18:22:56.69	-47:18:16.9	17:10:23.019
J1831.1-6503	18:31:06.55	-65:03:57.2	17:20:49.149
J1659.0-0140	16:59:03.72	-1:40:39.0	17:31:53.824
J1730.4-0359	17:30:26.07	-3:59:32.3	17:42:12.493
J1722.8-0418	17:22:50.76	-4:18:11.9	17:52:24.577
J1916.8-3025	19:16:53.69	-30:25:28.6	18:03:11.923
J1818.6+1316	18:18:36.65	13:16:23.2	18:14:02.676
J1747.6+0324	17:47:37.22	3:24:26.3	18:24:21.286
J1827.5+1141	18:27:30.86	11:41:10.7	18:34:39.994
J1735.3-0717	17:35:21.62	-7:17:07.1	18:45:05.139
J1913.4-1526	19:13:24.36	-15:26:58.6	18:55:41.304
J1906.4-1757	19:06:26.57	-17:57:03.2	19:05:55.135
J0139.5-2228	1:39:35.30	-22:28:39.7	19:17:33.080
J1845.8-2521	18:45:51.55	-25:21:30.6	19:29:09.148

TABLE B.4: The fourth observing block has been observed on 2020-10-01. Time refers to the starting time.

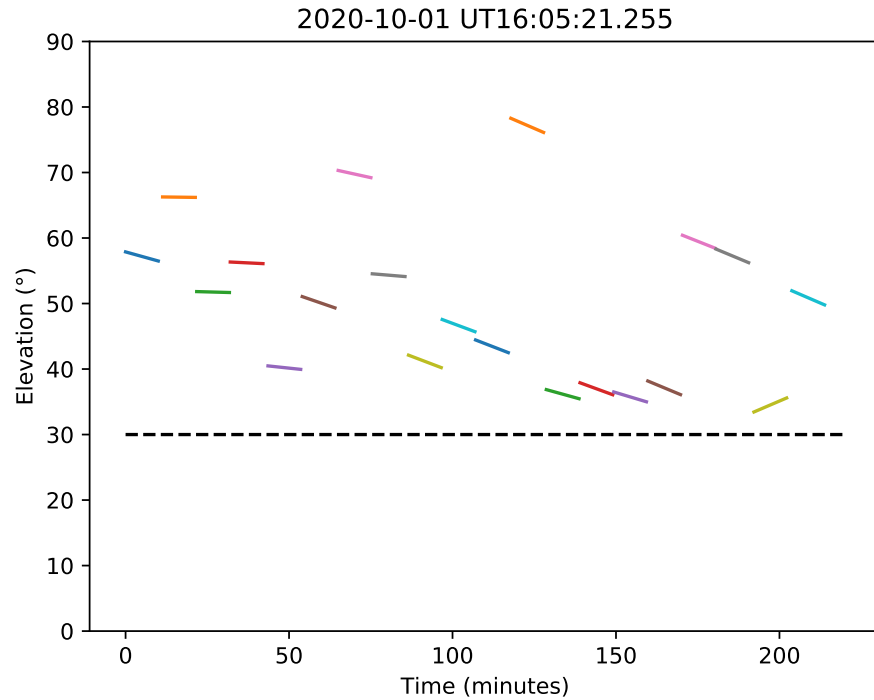


FIGURE B.4: The elevation of sources from the fourth observing block (1001). The dashed line is the minimum elevation at 30 degrees.

Appendix C

Beam tiling and position

This appendix depicts the beam tiling from each pulsar candidates. The plots are taken from the TRAPUM website.

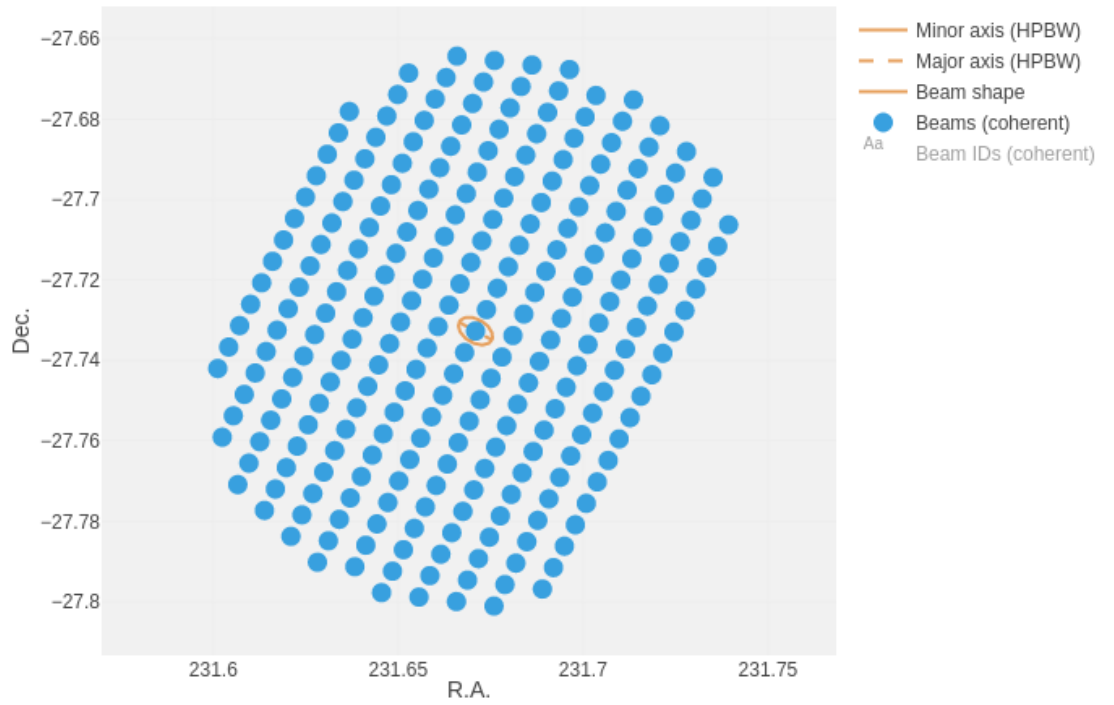


FIGURE C.1: 252 beams when observing J1526.6–2743, this plot is taken from TRAPUM website by Ewan Barr.

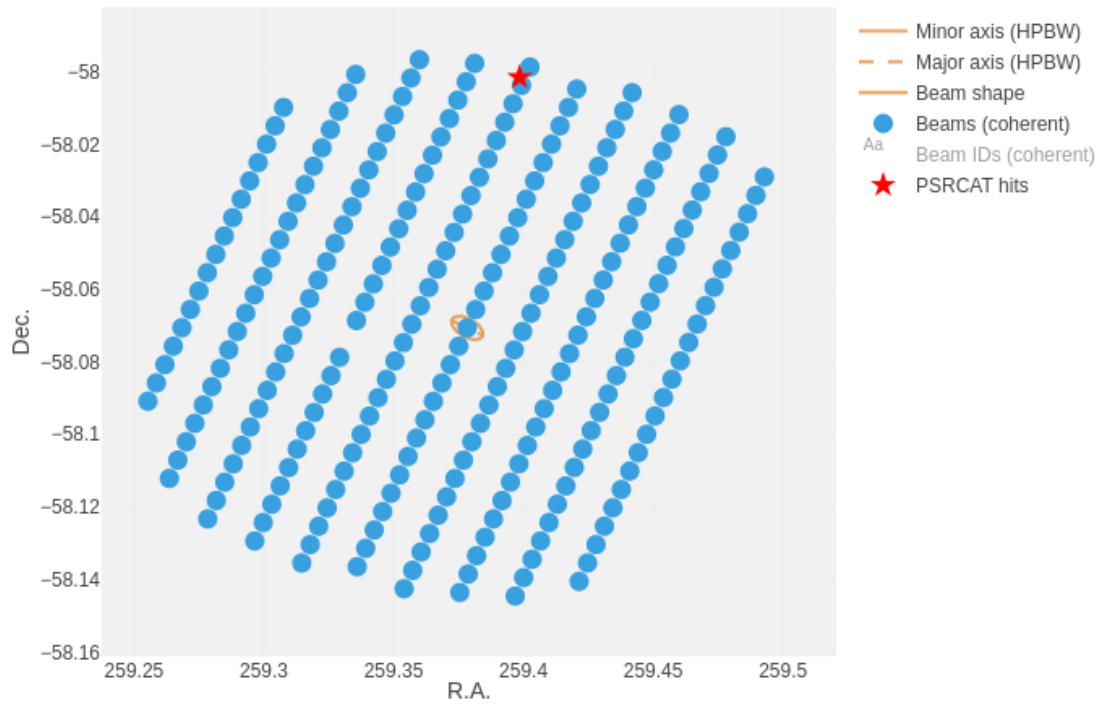


FIGURE C.2: 251 beams of J1717.5–5804, this plot is taken from TRAPUM website written by Ewan Barr.

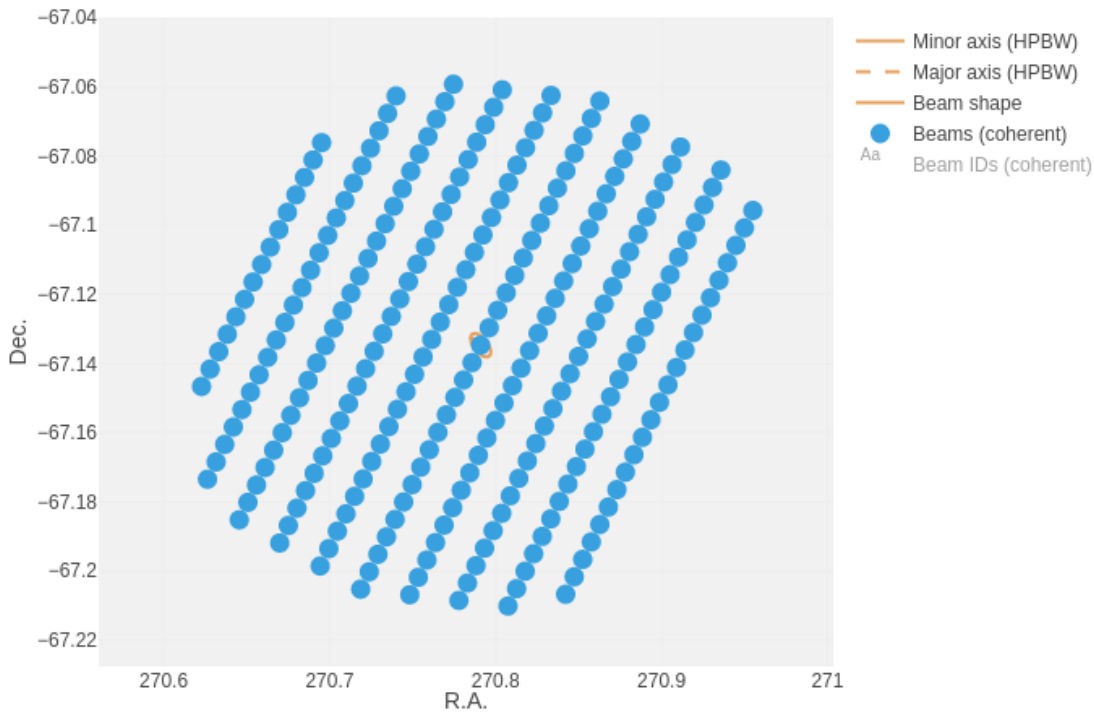


FIGURE C.3: 252 beams of J1803.1–6708, this plot is taken from TRAPUM website written by Ewan Barr.

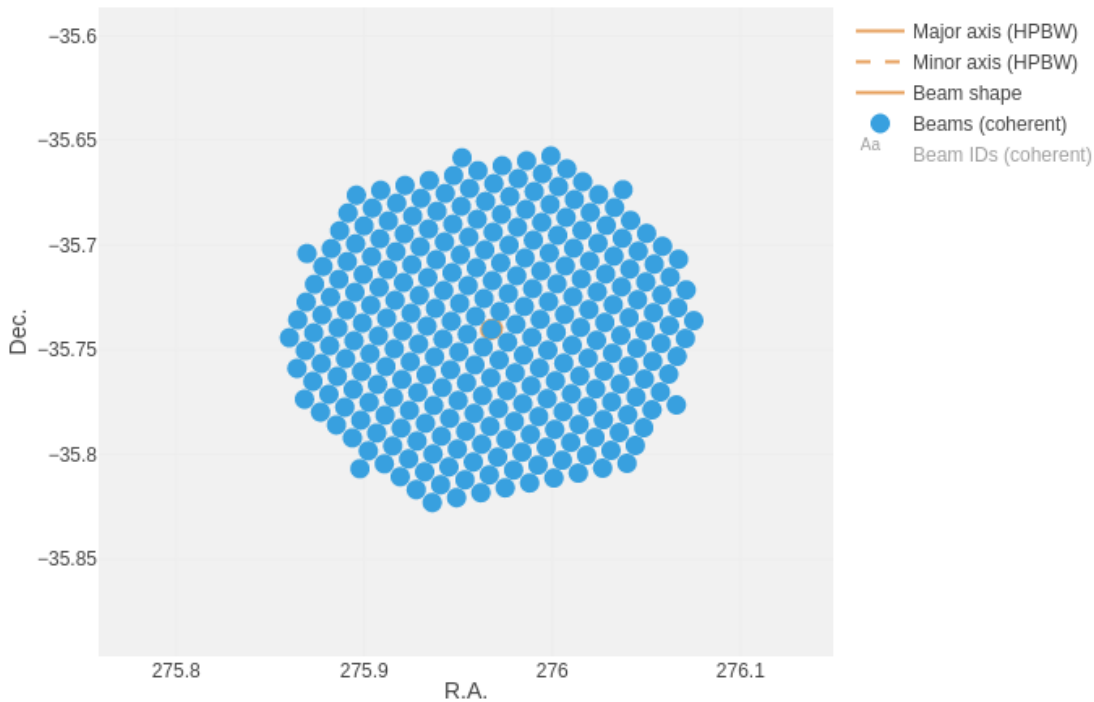


FIGURE C.4: 288 beams of J1823.8–3544, this plot is taken from TRAPUM website written by Ewan Barr.

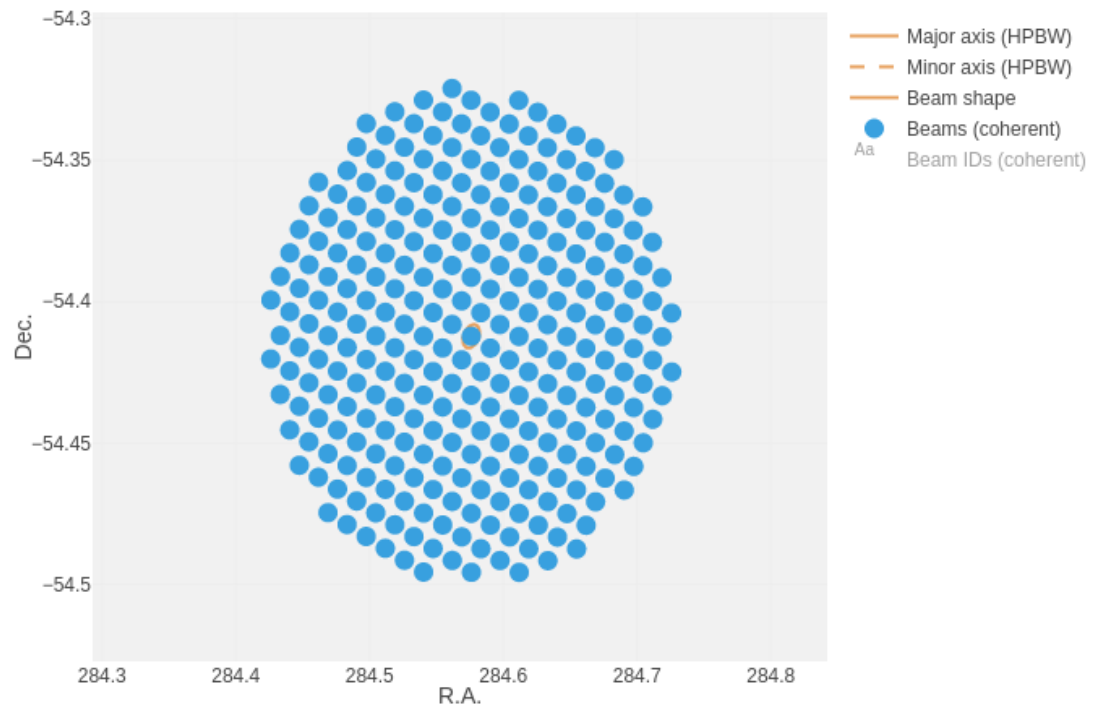


FIGURE C.5: 288 beams of J1858.3–5424, this plot is taken from TRAPUM website written by Ewan Barr.

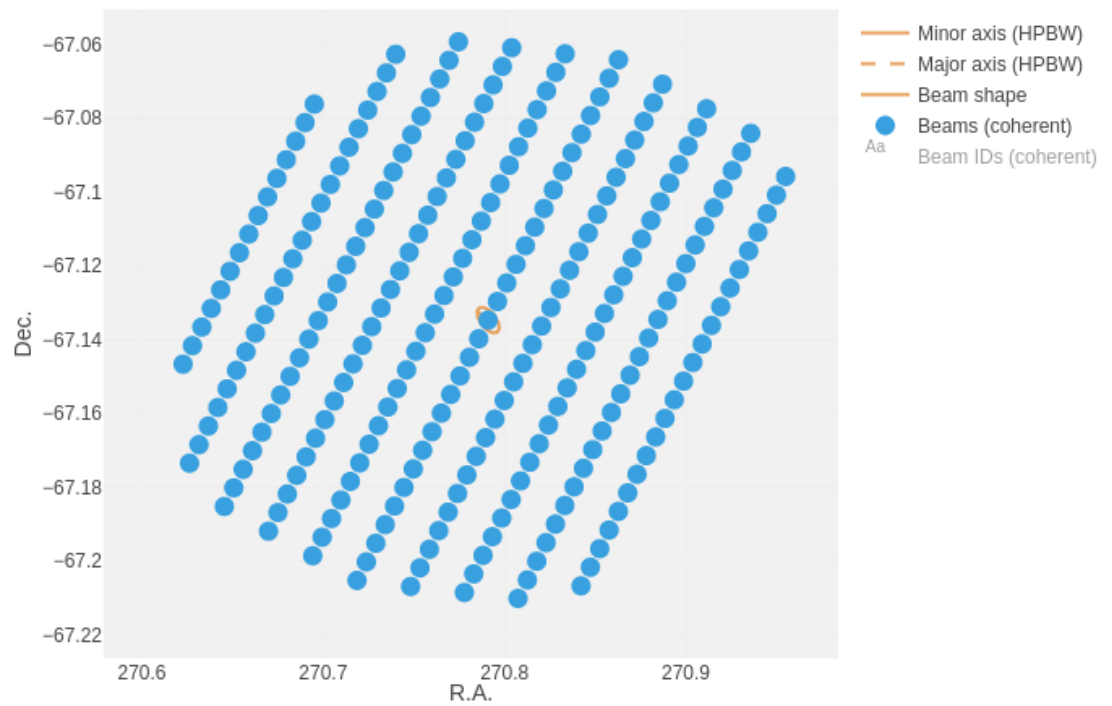


FIGURE C.6: 288 beams of J1906.4–1757, this plot is taken from TRAPUM website written by Ewan Barr.

Bibliography

- Abdo A. A., et al., 2010, [The Astrophysical Journal Supplement Series](#), 188, 405
- Abdollahi S., et al., 2020, [The Astrophysical Journal Supplement Series](#), 247, 33
- Acero F., et al., 2015, [The Astrophysical Journal Supplement Series](#), 218, 23
- Aliu E., et al., 2016, [The Astrophysical Journal](#), 831, 193
- Andersen B. C., Ransom S. M., 2018, [The Astrophysical Journal](#), 863, L13
- Antoniadis J., Tauris T., Ozel F., Barr E., Champion D., Freire P., 2016, arXiv: High Energy Astrophysical Phenomena
- Backer D. C., Kulkarni S. R., Heiles C., Davis M. M., Goss W. M., 1982, [Nature](#), 300, 615
- Ballet J., Burnett T. H., Digel S. W., Lott B., 2020, arXiv e-prints, p. [arXiv:2005.11208](#)
- Barr E. D., et al., 2012, [Monthly Notices of the Royal Astronomical Society](#), 429, 1633
- Barsdell B. R., Bailes M., Barnes D. G., Fluke C. J., 2012, [Monthly Notices of the Royal Astronomical Society](#), 422, 379
- Bates S. D., Lorimer D. R., Verbiest J. P. W., 2013, [Monthly Notices of the Royal Astronomical Society](#), 431, 1352
- Bilous A. V., et al., 2016, [Astronomy and Astrophysics](#), 591, A134
- Bogdanov S., Archibald A. M., Hessels J. W. T., Kaspi V. M., Lorimer D., McLaughlin M. A., Ransom S. M., Stairs I. H., 2011, [The Astrophysical Journal](#), 742, 97
- Booth R. S., de Blok W. J. G., Jonas J. L., Fanaroff B., 2009, arXiv e-prints, p. [arXiv:0910.2935](#)
- Breiman L., 2001, [Machine Learning](#), 45, 5
- Breton R. P., et al., 2013, [The Astrophysical Journal](#), 769, 108
- Brinkmann W., Aschenbach B., Langmeier A., 1985, [Nature](#), 313, 662
- Camilo F., et al., 2015, [The Astrophysical Journal](#), 810, 85
- Carroll B. W., Ostlie D. A., 2007, *An Introduction to Modern Astrophysics*, 2nd (international) edn

- Chandrasekhar S., 1935, *Monthly Notices of the Royal Astronomical Society*, 95, 207
- Chen H.-L., Chen X., Tauris T. M., Han Z., 2013, *The Astrophysical Journal*, 775, 27
- Condon J., Ransom S., 2016, Essential Radio Astronomy, Pulsars, Astr 534, <https://www.cv.nrao.edu/course/astr534/Pulsars.html>
- Cooley J. W., Tukey J. W., 1965, *Math. Comput.*, 19, 297
- Cordes J. M., Lazio T. J. W., 2002, arXiv e-prints, pp astro-ph/0207156
- Cromartie H. T., et al., 2016, *The Astrophysical Journal*, 819, 34
- De K., Gupta Y., 2016, *Experimental Astronomy*, 41, 67
- Detweiler S., 1979, *Astrophysical Journal*, 234, 1100
- Duncan R. C., Thompson C., 1992, *Astrophysical Journal, Letters*, 392, L9
- Edwards R., Bailes M., van Straten W., Britton M., 2001, *Monthly Notices of the Royal Astronomical Society*, 326, 358
- Guillemot L., et al., 2012, *Astrophysical Journal*, 744, 33
- Guo P., et al., 2019, *Monthly Notices of the RAS*, 490, 5424
- Halpern J. P., Strader J., Li M., 2017, *The Astrophysical Journal*, 844, 150
- Hankins T. H., Rickett B. J., 1975, in ALDER B., FERNBACH S., ROTENBERG M., eds, *Methods in Computational Physics: Advances in Research and Applications*, Vol. 14, Radio Astronomy. Elsevier, pp 55 – 129, doi:<https://doi.org/10.1016/B978-0-12-460814-6.50007-3>, <http://www.sciencedirect.com/science/article/pii/B9780124608146500073>
- Hewish A., Bell S. J., Pilkington J. D. H., Scott P. F., Collins R. A., 1968, *Nature*
- Johnston S., Karastergiou A., 2017, *Monthly Notices of the Royal Astronomical Society*, 467, 3493
- Johnston H. M., Kulkarni S. R., 1991, *Astrophysical Journal*, 368, 504
- Jonas J., MeerKAT Team 2016, in *MeerKAT Science: On the Pathway to the SKA*. p. 1
- Kaspi V. M., Beloborodov A. M., 2017, *Annual Review of Astronomy and Astrophysics*, 55, 261
- Keith M. J., et al., 2011, *Monthly Notices of the RAS*, 414, 1292
- Lorimer D. R., 2008, *Living Reviews in Relativity*, 11, 8
- Lorimer D. R., Kramer M., 2005, *Handbook of Pulsar Astronomy*. Cambridge University Press.

- Lorimer D. R., Bailes M., McLaughlin M. A., Narkevic D. J., Crawford F., 2007, [Science](#), 318, 777
- Lyne A. G., Graham-Smith F., 2006, *Pulsar Astronomy*. Cambridge University Press.
- Lyon R. J., Stappers B. W., Cooper S., Brooke J. M., Knowles J. D., 2016, [Monthly Notices of the RAS](#), 459, 1104
- Malofeev V., Gil J., Jessner A., Malov I., Seiradakis J., Sieber W., Wielebinski R., 1994, *Astronomy and Astrophysics*, 285, 201
- Manchester R. N., 2017, [Journal of Astrophysics and Astronomy](#), 38:42
- Manchester R., Hobbs G., Teoh A., Hobbs M., 2005, *VizieR Online Data Catalog*, 7245
- McLaughlin M. A., et al., 2006, [Nature](#), 439, 817
- Nice D., et al., 2015, *Tempo: Pulsar timing data analysis* (ascl:1509.002)
- Nolan P. L., et al., 2012, [The Astrophysical Journal Supplement Series](#), 199, 31
- O’Leary R. M., Kistler M. D., Kerr M., Dexter J., 2015
- Pacini F., 1968, [Nature](#), 219, 145
- Papitto A., et al., 2013, [Nature](#), 501, 517
- Pierbattista M., Grenier I. A., Harding A. K., Gonthier P. L., 2012, [Astronomy and Astrophysics](#), 545, A42
- Polzin E. J., Breton R. P., Bhattacharyya B., Scholte D., Sobey C., Stappers B. W., 2020, [Monthly Notices of the Royal Astronomical Society](#), 494, 2948
- Rajwade K., Lorimer D. R., Anderson L. D., 2015, [Monthly Notices of the Royal Astronomical Society](#), 455, 493
- Ransom S., 2011, *PRESTO: PulsAR Exploration and Search TOolkit* (ascl:1107.017)
- Ransom S. M., et al., 2010, [The Astrophysical Journal](#), 727, L16
- Ravi V., Manchester R. N., Hobbs G., 2010, [Astrophysical Journal, Letters](#), 716, L85
- Ray P. S., et al., 2012, arXiv e-prints, p. [arXiv:1205.3089](#)
- Remazeilles M., Dickinson C., Banday A. J., Bigot-Sazy M. A., Ghosh T., 2015, [Monthly Notices of the RAS](#), 451, 4311
- Ridley J. P., Lorimer D. R., 2010, [Monthly Notices of the Royal Astronomical Society](#), 404, 1081
- Roberts M. S. E., et al., 2018, in Weltevrede P., Perera B. B. P., Preston L. L., Sanidas S., eds, Vol. 337, *Pulsar Astrophysics the Next Fifty Years*. pp 43–46 ([arXiv:1801.09903](#)), [doi:10.1017/S1743921318000480](#)

- Saz Parkinson P. M., Xu H., Yu P. L. H., Salvetti D., Marelli M., Falcone A. D., 2016, [Astrophysical Journal](#), 820, 8
- Sieber W., 1973, *Astronomy and Astrophysics*, 28, 237
- Smith. S. W., 1998, *The Scientist and Engineer's Guide to Digital Signal Processing*. California Technical Publishing., <http://www.dspguide.com/>
- Smith D. A., et al., 2019, [The Astrophysical Journal](#), 871, 78
- Stappers B. W., et al., 2014, [Astrophysical Journal](#), 790, 39
- Strader J., et al., 2019, [The Astrophysical Journal](#), 872, 42
- Straten W. V., 2003, Ph.D. thesis, Swinburne University of Technology
- Swihart S. J., et al., 2020, [The Astrophysical Journal](#), 892, 21
- Tan C. M., Lyon R. J., Stappers B. W., Cooper S., Hessels J. W. T., Kondratiev V. I., Michilli D., Sanidas S., 2018, [Monthly Notices of the RAS](#), 474, 4571
- Taylor J. H., Weisberg J. M., 1982, [Astrophysical Journal](#), 253, 908
- Thompson D. J., et al., 1993, [Astrophysical Journal, Supplement](#), 86, 629
- Thornton D., et al., 2013, [Science](#), 341, 53
- Verbiest J. P. W., et al., 2016, [Monthly Notices of the RAS](#), 458, 1267
- W. Hotan A., van Straten W., N. Manchester R., 2004, [Publications of the Astronomical Society of Australia](#) 21, 302-309
- Zhu W. W., et al., 2014, [Astrophysical Journal](#), 781, 117